STUDIES ON HOT GAS H_2S REMOVAL SORBENTS IN FIXED-BED REACTORS AT HIGH TEMPERATURES

Thesis by

Miguel Jorge Bagajewicz

In Partial Fulfillment of the Requirements

for the Degree of

Doctor of Philosophy

California Institute of Technology

Pasadena, California

1988

(Submitted June 23, 1987)

To Mita

$\lim_{x \to 0} (1 + x)^{(1/x)^2}$! times

.... Experiments are many times falacious and always difficult and even when they reach perfection, they do not show us more than the extrinsic accidents, never the nature of things. The judgement falls on the results of the experiment and consequently it does not pass the limits of the exterior, and even this is perceived in an incomplete manner, not going beyond conjectures over the causes.

RENE DESCARTES

(1596-1650)

ACKNOWLEDGMENTS

My wife Patricia deserves much more recognition than I can express in writing. Not only has she been crazy enough to marry me, but she has remained at my side for more than 12 years altogether. Even when there was bad weather. Moreover, she put aside her own career to allow my studies at Caltech. Now it is her turn.

Next in line of those who made this thesis possible is my advisor, Dr George R. Gavalas. His presence and support when I had difficulties is deeply appreciated. He also let me fly alone, whenever it was possible. And I like flying very much.

Caltech has provided a lot more than I had expected. My deep appreciation to Carol Mastin for her understanding and help. When my son Marek was born in 1986, Caltech was present through her, helping us in those difficult financial times. Now that I am leaving this country, she remains in my memory as one example of the kind of good people that can be found in these lands.

The National Research Council of Argentina (CONICET) and the Universidad Nacional del Litoral in Santa Fe, Argentina, sent me here to pursue these studies. I cannot feel less than infinitely grateful for their support. Especially, I want to mention Dr. Alberto Cassano, who made the fellowship possible, and believed in me when bureaucrats were after me.

Amongst the many new friends we made, Julio and Graciela Josefina de Haro deserve our best appreciation. It is perhaps one of the rare cases in which personal estime can coexist with sometimes strong dissent. Our love also goes, of course, to all the people who made our social life meaningful.

Our children, Marek, Alejandro, Alina and Andrés enjoyed these years with us, and they deserve to be mentioned for providing all those wonderful moments.

ABSTRACT

Experimental and theoretical studies in the field of fuel gas desulfurization at high temperatures are presented. The performance of different oxides as sorbents for high temperature H_2S removal is evaluated. A fixed-bed microreactor was used for this purpose. Basically, streams containing different H_2S concentrations were passed through the reactor and the outlet H_2S concentration was measured as a function of time. Comparisons between observed and theoretical maximum conversion values are used as a measure of sorbent H_2S removal efficiencies.

Most of the work was devoted to study zinc oxide and vanadium oxide, but other sorbents were also investigated. ZnO was studied because of its high equilibrium constant for sulfidation. High surface alumina-supported ZnO and high surface bulk ZnO were tested. Alumina-supported ZnO proved to have a smaller desulfurization capacity than bulk ZnO. In the case of V_2O_5, chemisorption of H_2S on reduced vanadium oxide, rather than bulk sulfide formation, was found to be the mechanism of sulfur removal. Adsorption-desorption measurements were carried out in this case to investigate the behavior of the sorbent.

The regeneration step, which restores the oxide by means of oxidation of the spent sulfide, was also studied in detail. The rate of ZnS oxidation was measured using a thermogravimetric analyzer. For the range of temperatures 650-700°C, the rate of reaction was consistent with Langmuir kinetics. The activation energy and the free energy of oxygen chemisorption were determined. An undesirable side reaction during oxidative regeneration is sulfate formation. The kinetics of this reaction was also investigated by thermogravimetric measurements.

Theoretical studies dealing with reaction and diffusion processes in pellets and fixed-bed reactors were conducted, to a large extent motivated by the need

to describe desulfurization processes. One chapter is devoted to a survey of exact and approximate solutions for an isothermal fixed-bed gas-solid reactor. Approximate analytical solutions to a class of models of reaction and diffusion inside sorbent pellets are presented next. The last chapter is devoted to a traveling wave solution describing reaction fronts inside non-isothermal fixed-bed reactors. This provides a good analytical approach for the prediction of conditions for the formation of zinc sulfate during the regeneration of ZnS.

CONTENTS

LIST OF FIGURES

CHAPTER II

CHAPTER III

CHAPTER IV

CHAPTER V

CHAPTER VI

CHAPTER VIII

CHAPTER IX

LIST OF TABLES

CHAPTER I

No hay tiempo que no se acabe

ni tiento que no se corte

del Martín Fierro

INTRODUCTION

Coal gasification to low Btu Gas is pursued as a route to synthetic natural gas, synthetic liquid fuels and, more significantly, fuel for turbine or fuel cell combined cycles for highly efficient electric power generation.

Sulfur, nitrogen, alkali, and halogen compounds, all found in coal constitute contaminants that are released during gasification or combustion. These compounds not only pose environmental, corrosion and catalyst poisoning problems, but also limit the technical feasibility of some applications of coal gas such as fuel cells, which can tolerate only a very low level of contaminants.

Coal gasification consists primarily of the reactions with O_2 and steam to produce a gas containing CO, H_2 and, to a lesser extent, methane. The major non-fuel components are CO_2, unreacted H_2O and N_2, if air is used as the oxidant.

The concentration of these major components in the gasification atmosphere determine the equilibrium levels of various other compounds. Coal sulfur, which is present in both organic and mineral form, reacts to form H_2S and COS. The mole fraction of H_2S is in the range of $10^{-3} - 10^{-2}$ (*) throughout the range of practical gasification temperatures, whereas the mole fraction of COS varies from approximately 10^{-5} at low temperatures to 10^{-4} above 1000°K. These two gases appear to equilibrate rapidly through reaction with CO and H_2. Therefore, hot gas removal of H_2S will also remove COS. Mercaptans and CS_2 are present in smaller amounts (30-50ppm) and must also be removed in some applications.

Coal nitrogen reacts forming NH_3 in mole fractions around 10^{-4}. Above 1000°K, it also forms HCN in mole fractions about 10^{-5}. Fortunately, in many cases the concentration of NH_3 and HCN are below environmentally accepted levels and do not need to be removed. When removal is needed, NH_3 decomposition to N_2 and H_2 can be enhanced by a heterogeneous catalyst.

Removal of H_2S from cooled gasification products by wet, low temperature, chemical processes, such as absortion in alkaline solutions, is the standard commercial technology. However, since combustion and some other applications use the coal gas at high temperatures, the cooling of the gas to carry out desulfurization and the subsequent reheating in the combustion environment involves substantial degradation of thermal efficiency. To improve process economics, new high temperature desulfurization technologies are currently under research and development. These technologies make use of metal oxides as desulfurization agents. The following generic chemical reaction describes the metal oxide role

$$MO + H_2S \longrightarrow MS + H_2O$$

(*) All concentrations are taken from [1].

Aside from this bulk chemical reaction, H_2S adsorption on different types of surface sites may also take place.

Economics dictates that regeneration, rather than disposal of the sulfided sorbent, is essential in almost all cases. Different procedures can be used to regenerate the MeS. Regeneration can be carried out by reaction with either oxygen or H_2O according to:

$$MeS + O_2 \longrightarrow MeO + SO_2$$

$$MeS + H_2O \longrightarrow MeO + H_2S$$

although the second reaction is limited by equilibrium and is never used by itself.

In addition to the above two reactions, sulfate and elemental sulfur formation take place to a smaller extent depending on reactor conditions. In the case of alumina-supported sorbents, metal aluminate formation is also possible, and has been mentioned as responsible for the elemental sulfur formation during the regeneration.

By means of a purge of the sorbent with some inert gas, the chemisorbed H_2S can be removed before regeneration. If this step is ommitted, part of the adsorbed H_2S will react on the regeneration reaction front, and part will evolve and decompose ahead of the front as in pure desorption.

Final sulfur recovery or disposal is an important part of the desulfurization process. If regeneration leads directly to elemental sulfur, then no other step is necessary. If, on the other hand, it produces SO_2 or H_2S, these gases must be further disposed. When SO_2 is produced at sufficiently high concentrations it can be converted to sulfuric acid or reduced by carbon to elemental sulfur.

Various properties of the sorbents are important. From the standpoint of the sulfidation step, thermodynamic equilibrium , as well as reaction kinetics,

is crucial. Thermodynamic equilibrium determines the outlet concentration of H_2S in the desulfurization reactor ahead of the reaction front, and therefore also the H_2S content of the cleaned gas. Rate processes including specific reaction rates and diffusional rates determine the shape of the reaction front. The outlet concentration uptake at breakthrough is directly related to the shape of this front that travels along the reactor. Sharply decaying concentration profiles such as those typical of traveling shocks are preferred. The following schematic illustrates desirable and undesirable profiles.

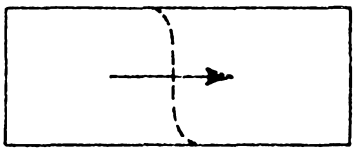

desired profile

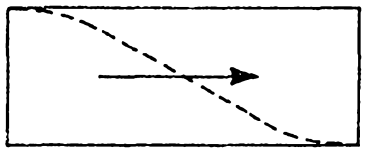

undesired profile

In the case of slowly decaying concentration profiles, the maximum acceptable level of contaminant is rapidly reached at the outlet, resulting in poor utilization of the sorbent. Therefore, the width of the concentration wave on which significant changes in concentration occur is, aside from the desulfurization capacity, a very important parameter, which can discourage the use of a thermodynamically promising material.

High specific surface area provides good gas accessibility to the solid and therefore enhances the reaction rate. It is therefore of importance to reduce sintering processes to a minimum. Also, the regeneration process should restore the original sorbent surface area. High O_2 concentrations used in regeneration increase reaction kinetics, but produce high temperature spots at the oxidation front. High temperature can produce a considerable amount of sintering and is undesirable. The reduction of the metal oxide to produce gaseous metal vapors

that leave the reactor with the exit stream can produce significant sorbent losses and must be avoided. Finally, mechanical stability to facilitate sorbent handling is necessary.

High levels of O_2 in the regeneration step also imply high levels of SO_2. Both compounds can react with freshly formed ZnO at the oxidation front to form metal sulfate. Generally, sulfate decomposes at a very low rate, and if it is present during the sulfidation step it will be reduced, producing undesirable SO_2 in the exit stream. For this reason regeneration should be conducted selecting operating conditions that avoid or minimize the formation of sulfate.

In view of all these various requirements, there is not a single sorbent that will meet all of them. For this reason a lot of research is being done to select appropiate sorbents.

Westmoreland and Harrison [2] performed a thermodynamic screening of 28 metal oxides. Among the different oxides they showed that oxides of the metals Fe, Zn, Mo, Mn, V, Ca, Sr, Ba, Co, Cu, and W were the most promising from the thermodynamic point of view. Zinc and vanadium oxides have shown the highest desulfurization potential over a wide range of temperatures [2]. Kinetic investigations have been made on the reaction of H_2S with ZnO [3], and the reaction rate was found to be high enough to encourage more theoretical and experimental studies on this oxide.

One chapter of this thesis presents studies on the desulfurization properties of selected mixed and pure oxides. The rest of this thesis is devoted to detailed studies on ZnO and V_2O_5 with the aim of obtaining deeper understanding of the mechanisms involved in selected steps of the desulfurization processes performed using these oxides.

As will be seen from the analysis included in this thesis, there is scope for

further fundamental research in high-temperature MeO (metal oxide) sulfidation as well as in MeS (metal sulfide) regeneration. Fixed-bed reactor modeling is needed to anticipate the form of the concentration wave, especially in the sulfidation step, and to predict hot spots as well as sulfur and sulfate formation during the regeneration step.

One chapter of this thesis is devoted to the analysis of reaction and diffusion processes inside sorbent pellets. Another chapter is devoted to the modeling of some aspects of the regeneration process. These theoretical studies, although motivated by the field of H_2S removal at high temperatures, are also more generally applicable to other gas-solid reactions.

BRIEF OUTLINE OF THE THESIS CONTENTS

In Chapter II a preliminary analysis based on a literature review is presented. In Chapter III a fixed bed microreactor setup used to conduct the desulfurization experiments is described. Some experiments carried out with alumina-supported ZnO are also described. Chapter IV is devoted to experimental results of the desulfurization performance of different pure and mixed oxides using a fixed bed microreactor. This work was done at JPL in collaboration with other investigators. In Chapter V the H_2S desorption from vanadium oxide sorbents is discussed and a mathematical model is used to interpret the results. Chapter VI is devoted to the study of the kinetics and mechanism of the ZnS regeneration reaction. Intrinsic reaction rates are presented and sulfate formation results are reported and discussed. In Chapter VII some problems relating to the mathematical description of sulfidation are outlined. Chapter VIII is devoted to a method for obtaining monotone bounds for certain gas-solid

reaction problems. Finally, in Chapter IX an approximate traveling wave solution is proposed to obtain temperature, concentration and conversion profiles for the ZnS regeneration process. This model is then used to study the conditions under which $ZnSO_4$ is formed during the process.

REFERENCES

1.-: Giner Inc., Final report to Argonne National Laboratory. Contract 31-109-39-5804, Waltham MA, 1981.

2.-: Westmoreland P.R. and Harrison D.P. *Env. Sci. & Tech.*, 1976, **10**, 659.

3.-: Westmoreland P.R., Gibson J.B. and Harrison D.P. *Env. Sci. & Tech.*, 1977, **11**, 489.

CHAPTER II

Que son campanas de palo
Las razones de los pobres

del Martín Fierro

BACKGROUND MATERIAL

In this chapter the thermodynamics, mechanism and kinetics of the different steps of a desulfurization process are briefly reviewed. Some particular phenomena related to a fixed bed reactor are included. Reference is made to experimental work with a microreactor performed at JPL, which is described in a later chapter. Since the main emphasis of this thesis is placed on ZnO and V_2O_5, the basic issues and outstanding problems of the desulfurization process are discussed describing their performance. First, the main reaction and certain side reactions of the sulfidation step are discussed. Then, the intermediate desorption step is briefly analyzed, and finally regeneration is described and discussed.

Sulfidation in Reducing Atmosphere

Taking advantage of the high equilibrium constant for reaction with H_2S at high temperatures, ZnO has been selected [1-4] as one of the most suitable

sorbents for gas desulfurization. The process is conducted normally in a fixed-bed reactor at temperatures in the range $550 - 700°C$. As described earlier, the main constituents of the fuel gas are CO and H_2. These determine a reducing atmosphere from which H_2S is to be removed, lowering its concentration from $10^{-3} - 10^{-2}$ mole fractions to a few parts per million in some cases. Another component present in the fuel gas is H_2O, whose concentration is important in establishing the level of equilibrium outlet conditions. To increase the reaction rate and make more ZnO accesible to the H_2S, the sorbent is supported on alumina, or it is prepared in a bulk form using a special technique, which produces a high surface area material.

Aside from possible interactions with the support, which are going to be mentioned later, the relevant reactions of the sulfidation step are

- Adsorption:

$$H_2S_{(g)} + (*) \longrightarrow H_2S_{(ad)} \qquad (1)$$

where (*) denotes the chemisorption site.

- Sulfidation:

$$ZnO_{(s)} + H_2S_{(ad)} \longrightarrow H_2O_{(g)} + ZnS_{(s)} \qquad (2)$$

The sulfidation reaction (2) has been studied over low specific surface area ZnO [1] , by measuring the initial reaction rate. The reaction was found to be first order in gaseous H_2S concentration, and the preexponential factor and activation energy were determined. In these experiments, like in other ZnO pellet sulfidations [2,3], the adsorption reaction (1) was not reported. In one case where it was observed [4], it did not have a significant impact on the overall conversion. The total surface area used was 4.9 (m^2/g) for kinetic determinations

[1], and 17-34 (m^2/g) for pellet studies [2,3]. Contrasting with these low values, the surface area of alumina-supported ZnO is of the order of 80-100 m^2/g, increasing drastically the importance of the adsorption step.

Adsorption has been mentioned as an intermediate, but not a controlling step, of other sulfidation reactions as FeS sulfidation [5,6]. Adsorption can occur on ZnO as an intermediate but not as a controlling step, but can also take place on ZnS and the alumina support. The interactions due to adsorption on these different sites are not fully understood.

In some other sorbents, like V_2O_5, adsorption is responsible for almost all the desulfurization capacity, as is described in detail in Chapter V of this thesis.

The Interaction with the Support

Before the desulfurization properties of any supported sorbent are studied, it is important to determine the role played by the support.

No sulfur compound is known to form by the alumina under desulfurization conditions. At the same time, adsorption on alumina is limited. For example, at 700°C and H_2S concentration of 5000 ppm the coverage is only 8.0×10^{-8} moles/m^2, which is 100 times smaller than the adsorption capacity of supported V_2O_5 under the same conditions. Another type of alumina, used as a support for ZnO, showed a capacity in some cases equivalent to as much as 20 % of the overall capacity of supported ZnO, as is reported in Chapter III.

When bulk sulfide formation is the main reaction, as in the case of ZnO, the contribution of chemisorption on the support to the overall sorbent capacity cannot be determined unless the area of support exposed to the gaseous phase after impregnation is determined.

Other types of interactions can take place. For example, for the case of alumina-supported ZnO, a study conducted at IGT [7] showed that zinc aluminate ($ZnAl_2O_4$) reacts with H_2S as follows:

$$ZnAl_2O_4 + H_2S \longrightarrow ZnS + Al_2O_3 + H_2O \qquad (3)$$

These experiments were performed using pure $ZnAl_2O_4$ mixed with alumina. In the case of alumina impregnated with ZnO, a solid-solid reaction must take place to give the aluminate first . If a substantial amount of this spinel compound is indeed forming during successive sulfidation-regeneration cycles, its degree of exposure to the gas phase is very important.

Nagata *et al.* [8] measured the rate of $ZnAl_2O_4$ formation. The solid state reaction follows the parabolic rate typical of this kind of solid-solid reactions. Extrapolating their rate expression to 1000 °K for a specific area of 100 m^2/g and a loading of ZnO of 4.2 wt %, the time needed to convert all the ZnO to aluminate is around 5 sec. An x-ray diffraction test was performed on freshly impregnated sorbent as well as on sorbent calcined at 700°C over 12 hours. The results showed that the $ZnAl_2O_4$ was present in appreciable amounts.

The Effect of the Reducing Atmosphere

In the presence of H_2 the side reaction

$$H_{2(g)} + ZnO_{(s)} \longrightarrow Zn_{(g)} + H_2O_{(g)} \qquad (4)$$

could be significant, and normally can be avoided by increasing the H_2O concentration. Low Btu gas contains as much as 10 % H_2O. Considering both reactions (1) and (4) being at equilibrium at the reactor outlet, the influence of the feed

water concentration on $Zn_{(g)}$ and H_2S partial pressures can be calculated. Using the thermodynamic data from [9] to calculate equilibrium constants, it is found that the addition of 10% H_2O to a dry fuel gas produces a reduction of the $Zn_{(g)}$ partial pressure by a factor of 13. At the same time, the equilibrium H_2S concentration is increased 10 times, which may or may not exceed the limit of the H_2S specification for the cleaning process. However, a further increase in water content to 20 % lowers the $Zn_{(g)}$ partial pressure by only a factor of 2, and doubles H_2S concentration. Contrasting with the above theoretical predictions, runs at JPL showed an increase in deposition downstream of the reactor, whenever water was present. This phenomenon as well as the reduction by CO needs to be further clarified.

The Desorption Step

A desorption step can be used between sulfidation and regeneration to increase the amount of H_2S recovered in the regeneration step. In addition, elemental sulfur is produced during the desorption due to H_2S decomposition, which is slow in the gas phase, even at high temperatures, but is known to be catalyzed by certain sulfides [10]. Chapter V of this thesis is devoted to study both experimentally and theoretically this process for the case of alumina-supported V_2O_5.

The Regeneration Step

Before discussing reactions and mechanisms involved in the regeneration process, a few comments about the thermodynamic stability of the different phases are needed. The triangular diagram of Figure 1 shows the different compounds in equilibrium when all condensed phases are solids. The gas phase

may have any composition betwen pure S_2 and pure O_2. More familiar are diagrams like the one of Figure 2, where the phase equilibria are shown as a function of the partial pressure of two components in the gas phase. In this type of diagram each phase is stable within a predominance region, bordered by lines that represent the coexistence with other phases. The slope of each curve is given by the stoichiometry of the corresponding reaction.

The effect of temperature is usually displayed by plotting ln P_{O_2} against 1/T at constant P_{SO_2} as shown in Figure 3 . Curves for different SO_2 pressure can be obtained by shifting the curves as illustrated by the dotted lines. We notice that the oxygen potential for equilibria between Me and MeO and between MeS and $MeSO_4$, are not affected by the SO_2 pressure. In addition to SO_2 and S_2, the gas will contain some SO_3 produced by SO_2 oxidation. Finally, some intermediate stable compounds such as $2ZnSO_4.ZnO$ can be expected as can be seen in Figure 4. A complete diagram for the case of the system Zn-O-S was constructed and is shown in Figure 1 of Chapter VI.

Regeneration with Oxygen

The reactions that can take place are the following(*):

$$ZnS + 2\,O_2 \longrightarrow ZnSO_4 \qquad \Delta G = -106.4 \text{ Kcal/mol} \qquad (5)$$

$$ZnS + \frac{3}{2}\,O_2 \longrightarrow ZnO + SO_2 \qquad \Delta G = -87.7 \text{ Kcal/mol} \qquad (6)$$

$$ZnO + SO_2 + \frac{1}{2}\,O_2 \longrightarrow ZnSO_4 \qquad \Delta G = -18.7 \text{ Kcal/mol} \qquad (7)$$

Different kinetic studies have been performed on reaction (6) [12-14]. Fukunata *et al.* [12] reviewed these studies and pointed out discrepancies among the

(*) All free energies of formation given in this chapter are at 1000°K.

reported results. Consequently, there is a need for detailed rate determinations for this reaction. Some relevant results regarding the rate of reaction (6) are described in Chapter VI of this thesis.

Reaction (6) was assumed by almost all investigators to be the main mechanism by which ZnS oxidation takes place. If this mechanism is assumed, the small amounts of sulfate formed are due to reaction (5) or (7). However, other mechanisms are possible. For example, if $ZnSO_4$ forms according to reaction (5) and later decomposes according to reaction (7), two reaction fronts can form as shown in the diagram below.

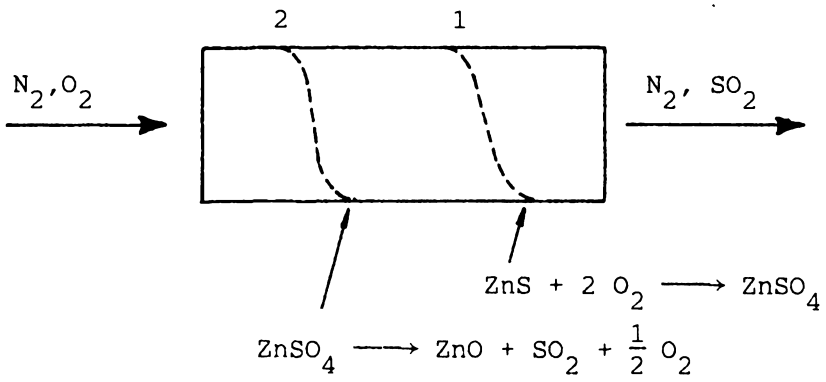

According to this suggestion ZnS would give first $ZnSO_4$ at interface 1 reacting directly with O_2. Decomposition would follow at interface 2, since no SO_2 is present in the feed . If reaction at front 1 is faster, the two fronts will be clearly at different positions. Note that in this last case, reaction (5) would proceed in the presence of relatively high concentrations of SO_2. According to figure 2, as SO_2 concentration increases, oxysulfate and sulfate become the most stable species giving thermodynamic support to the above mechanism.

Twidwell and Larson [15] and Skachkov [16], studied the kinetics of $ZnSO_4$ decomposition, alone and in the presence of ZnS. The crystalline form of $ZnSO_4$

is rhombic and requires crystallographic transformations to give the hexagonal ZnO. The reaction of hexagonal ZnS to form $ZnSO_4$ requires crystallographic transformation as well. The absence of crystallographic changes from ZnS to ZnO suggests that reaction (6) is more facile than the other two reactions.

The above arguments do not allow an *a priori* determination in favor of one or the other route of ZnS oxidation. Additional experiments are needed for this purpose. The experiments reported in Chapter VI of this thesis give conclusive proof that oxidation takes place by reaction (6) followed by reaction (7). In Chapter IX a theoretical study is used to investigate the conditions that favor the occurrence of reaction (7) inside a fixed-bed reactor. From this study theoretical guidelines are given to avoid sulfate formation.

Once sulfate is formed, its decomposition is slow . If a nitrogen purge is carried out after regeneration, a maximum in SO_2 concentration is observed after a few minutes. This gives some support to earlier reports [16] indicating that $ZnSO_4$ decomposition is autocatalytic. The undecomposed $ZnSO_4$ remaining in the sorbent would be reduced by the fuel gas during the sulfidation step, producing undesirable SO_2 at the reactor outlet. If the solid product of the sulfate reduction is only ZnO, an exposure of the regenerated bed to a reducing gas would complete the preparation of the bed for a new sulfidation cycle. To explore such possibility, preliminary experiments were performed at JPL where a N_2-H_2 mixture was passed through a regenerated bed to reduce $ZnSO_4$, aiming to convert the residual $ZnSO_4$ to ZnO. Evidence of ZnS presence as a result of this reduction was obtained by treating the bed again with a N_2-air mixture and observing that SO_2 is formed. Therefore, reduction of $ZnSO_4$ produces ZnS in addition to ZnO.

In regeneration experiments performed at JPL using alumina-supported

ZnO, substantial amounts of sulfur were seen during the first few minutes. This could be explained by the presence of H_2S chemisorbed on ZnS at the end of the sulfidation step. The chemisorbed H_2S would desorb ahead of the oxidation front, and decompose due to the absence of H_2. This decomposition is catalyzed by the sulfide, as mentioned earlier. However, when desorption by an inert purge preceded the introduction of oxygen, sulfur was still seen to evolve in appreciable amounts. This indicates that some mechanism, in addition to H_2S decomposition, is providing sulfur. The regeneration of ZnS with simultaneous $ZnAl_2O_4$ formation [7] as shown below could be this additional source of sulfur.

$$ZnS + Al_2O_3 + \frac{1}{2} SO_2 \longrightarrow \frac{3}{4} S_2 + ZnAl_2O_4 \quad \Delta G = -6.6 \text{ Kcal/mol} \qquad (8)$$

The formation of ZnO in a similar reaction, but without the intervention of the support has a relatively high positive ΔG :

$$ZnS + \frac{1}{2} SO_2 \longrightarrow \frac{3}{4} S_2 + ZnO \qquad \Delta G = 15.8 \text{ Kcal/mol} \qquad (9)$$

indicating that in the former case the formation of aluminate is essential in the production of sulfur.

Regeneration with Water and Water-Oxygen Mixture

The reaction with H_2O is exactly the opposite of the sulfidation reaction

$$ZnS + H_2O \longrightarrow ZnO + H_2S \qquad (10)$$

Downstream of the reaction front, adsorption of H_2S can take place and sulfur formation can occur *via* the already described surface decomposition. Since the equilibrium constant for reaction (1) is high, it can be anticipated that H_2O is not effective as a regenerating agent. This was confirmed by Giner [4]. As

expected, they observed significant increase in the rate of regeneration when air was added.

$ZnSO_4$ formation in the presence of O_2 is somewhat retarded by the presence of H_2O, as was observed by Giner [4] and confirmed in JPL experiments. The inhibition of $ZnSO_4$ formation constitutes an attractive property of the combined air-H_2O regeneration, but is not well understood. It is highly probable that H_2O competes for sites with oxygen, reducing the rate of sulfide oxidation and lowering the concentration of SO_2 in the reactor. Under these conditions, sulfate formation according to reaction (7) would be less favorable.

REFERENCES

1.-: Westmoreland P.R., Gibson J.B. and Harrison D.P. *Env. Sci. & Tech.*, 1976, **11**, 489.

2.-: Gibson III J.B. and Harrison D.P. *I&EC Proc. Des. & Dev.*, 1980, **19**, 231.

3.-: Ranade P.V. and Harrison D.P. *Chem. Engng. Sci.*, 1981, **36**, 1079.

4.-: Giner Inc., Final report to Argonne National Laboratory. Contract 31-109-39-5804, Waltham MA, 1981.

5.-: Turkdogan E.T. *Trans. of the Metall. Soc. of AIME*, 1968, **242**, 1665.

6.-: Worrell W.L. and Turkdogan E.T. *Trans. of the Metall. Soc. of AIME*, 1968, **242**, 1673.

7.-: Anderson G.L., Garrigan P.C. and Berry F.E. *AIChE 89th National Meeting*, 1980.

8.-: Nagata K., Sato K. and Goto K. . *Metall. Transactions of AIME*, 1980, **11B**, 455.

9.-: Barin I. and Knacke O. Thermodynamic Properties of Inorganic Substances. *Springer Verlag*, New York, 1973.

10.-: Fukuda K., Dokiya M., Kameyama T. and Kotera Y. *I&EC Fund.*, 1978, **17**, 4, 243.

11.-: Turkdogan E.T. Physical Chemistry of High Temperature Technology. *Academic Press*, New York, 1980.

12.-: Fukunata Y, Monta T., Asaki Z. and Kondo Y. *Metall. Transactions*, 1976, **7B**, 307.

13.-: Denbigh L.G. and Beveridge K.G. *Trans. Inst. Chem. Eng.*, 1962, **40**, 23.

14.-: Cannon K.J. and Denbigh K.G. *Chem. Engng Sci.*, 1957, **6**, 145.

15.-: Twidwell L.G. and Larson A.H. *Trans. of the Metallurgic Soc. of AIME*, 1966, **236**, 1379.

16.-: Skachkov B.I. *Chem. Abst.*, **53**, 6860.

17.-: Rosenqvist T. *Metall. Trans. of AIME*, 1978, **9B**, 337.

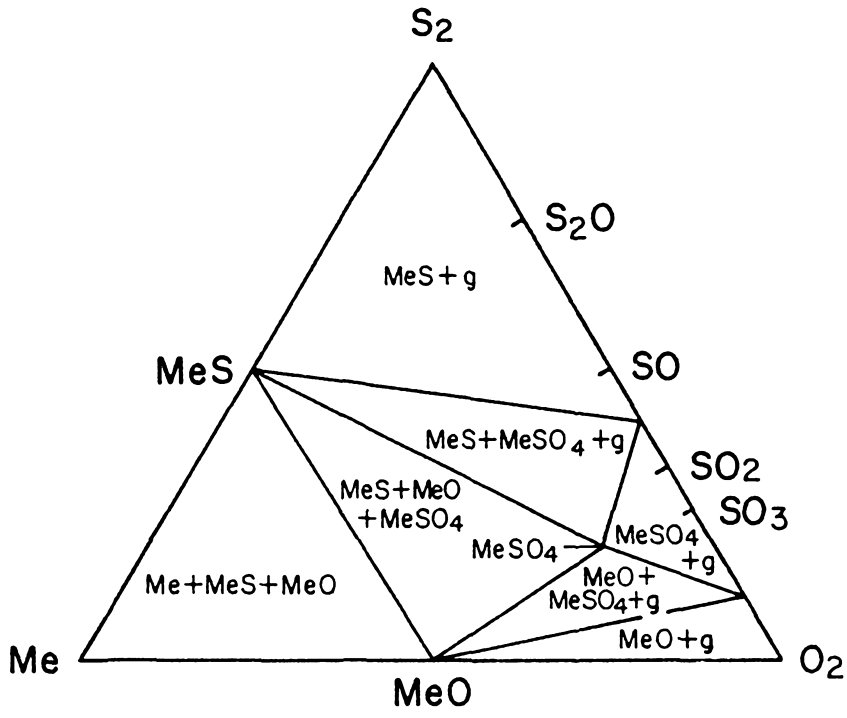

Figure 1: Phase Equilibria in a System Me-S-O. Schematic. (from [17]).

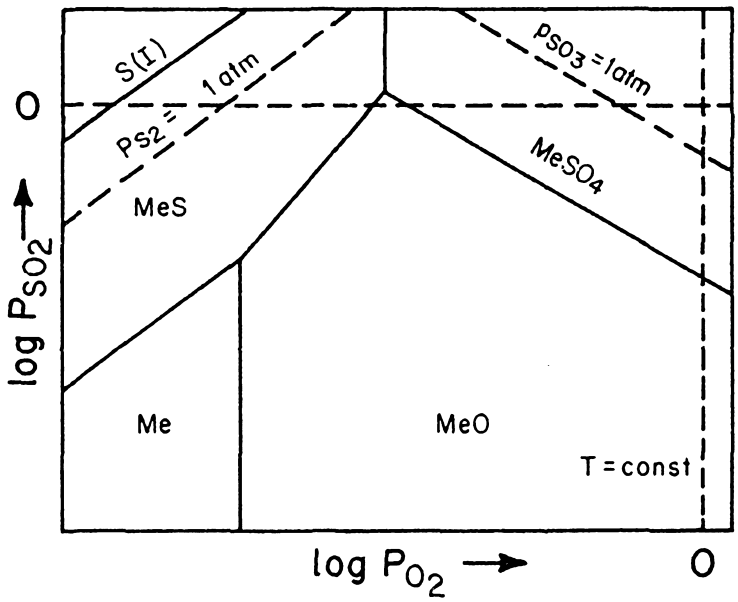

Figure 2: Predominance Areas for Phases in the System Me-S-O at constant Temperature. Schematic (from [17]).

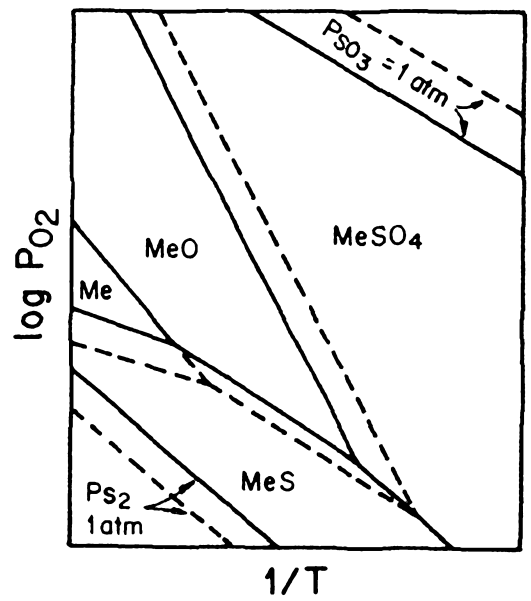

Figure 3: Effect of Temperature on Phase Equilibria in the System Me-S-O at constant SO_2 Pressure. Schematic (from [17]).

—— p_{SO_2} = 1.0 atm, --- p_{SO_2} = 0.1 atm. p_{tot} = 1 atm.

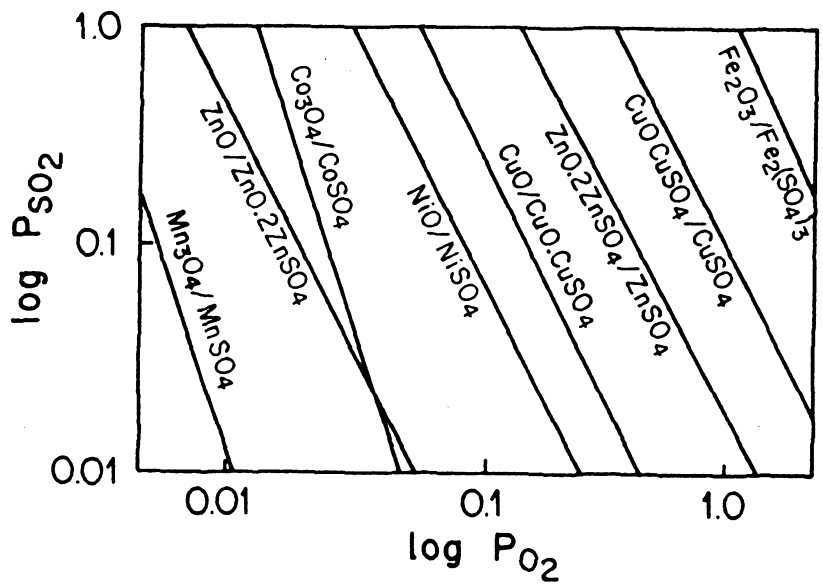

Figure 4: Equilibrium Partial Pressures of O_2 and SO_2 for Coexisting Metal Oxides and Sulfates at 800°C (from [1]).

CHAPTER III

Hay sabios de todas menas
Mas digo, sin ser muy ducho
Es mejor que aprender mucho
El aprender cosas buenas

del Martín Fierro

INTRODUCTION

In this chapter a description is given of the experimental microreactor system used to perform all the sulfidation and regeneration experiments. Subsequently, experimental results obtained studying the performance of alumina-supported ZnO as a desulfurization sorbent are described.

EXPERIMENTAL REACTOR SYSTEM

Experiments were carried out using a reactor system, which is schematically shown in Figure 1. The laboratory-scale reactor is a 1 cm-ID quartz tube, 41 cm in length mounted vertically inside an electric furnace. A porous quartz disk fitted 1 inch away from the tube center supports the bed and a K-type (chromel-alumel) thermocouple is inserted through a 0.3 cm -ID quartz tube concentric to the reactor. An arrangement is made so that the desired mixture can flow

through the reactor either in the downward or upward direction. In either case an ice-cooled trap at the reactor outlet collects elemental sulfur and/or water. Temperature is monitored at various points of the system.

Steam can be added to a nitrogen stream by means of a 3-neck flask, maintained at constant temperature. An absorber loop containing iodine solution is placed at the exit line for the purpose of analyzing total sulfur gases (H_2S, SO_2) during regeneration.

Downward direction of flow is used in desorption and regeneration runs, whereas upward direction is used in sulfidation. The concentrations of SO_2 and H_2S in the product gas are monitored as a function of time using a gas chromatograph (GC). In the GC, a 6 ft $\times$ 1/8" Teflon column packed with Chromosil 310 separates the sulfur gases, which are then conducted through a flame photometric detector (FPD). A microprocessor records the chromatograms, integrates and obtains peak areas.

EXPERIMENTAL RESULTS FOR ALUMINA-SUPPORTED ZnO

As explained before, the outlet H_2S concentration at breakthrough is related to the concentration wave that travels along the reactor. We will call the breakthrough curve, the plot of the outlet H_2S concentration as a function of time. Breakthrough time can be defined in different ways. Some authors define it as the time at which the outlet concentration reaches some predetermined value, called breakthrough concentration. This definition is very useful from the practical point of view, but has to be used together with a criterion for selecting the value of the breakthrough concentration. Another definition, which we will use, defines breakthrough time as the interception of the tangent at the inflex-

ion point of the curve with the time axis, as shown in the following schematic diagram.

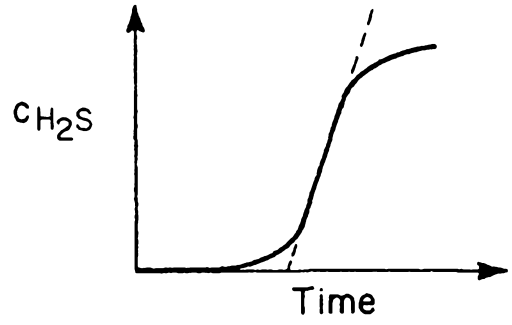

The slope of the tangent at the inflexion point, which we call the breakthrough curve slope, is another useful quantity. High values of the slope are a desirable sorbent characteristic. This definition provides means for analyzing the experimental breakthrough curve in terms of a kinetic model.

The first supported ZnO that was tested, denoted CAT-15Z, had a loading of 3.9 wt % of Zn on alumina. The alumina used to prepare this sorbent was -20+40 mesh MCB alumina. This alumina is commercially known as ALCOA F-1 and was thermally stabilized at 800°C, washed with a solution of NH_4OH and finally dried. The surface area dropped from 240 to 100 m^2/g after stabilization. The manufacturer reported a pore volume of 0.25-0.3 cm^3/g and an average pore size of 600 Å.(*) Figure 2 shows the breakthrough curves where t^* is the time corresponding to 100 % Zn conversion. The feed gas contained 0.2 % (vol) of H_2S and 20 % (vol) of H_2 to simulate the reducing atmosphere of a gasifier gas. H_2O was not added in these experiments. The succesive breakthrough curves had a similar shape but the breakthrough time declined from 0.44 to

(*) The pore size distribution was actually bimodal, accounting for 50 % of the pores having an average pore size of 40-45 Å.

0.23, indicating a loss of sorbent capacity. The slope of the breakthrough curves remained roughly the same, indicating that reaction rate was not affected by repeated sulfidations and regenerations. The supported ZnO was treated with nitric acid to dissolve the Zn and the liquid sample was analyzed for Zn concentration, using atomic absorption. The measurements revealed a drop of Zn concentration in the particles to 1.2 wt%. Sorbent analysis by XRD showed the presence of $ZnAl_2O_4$ as well as ZnO. Since $ZnAl_2O_4$ is not soluble in nitric acid, only part of the Zn losses detected by the atomic absorption technique can be attributed to vaporization of elemental zinc formed by reduction of the oxide.

Experiments using blank MCB alumina were also performed. The H_2S exit concentration profiles obtained for the sulfidation of this blank alumina are included in Figure 2. To make the comparison more useful, the same value of t^* as for CAT-15Z was used. A relatively large amount of H_2S was retained by this alumina (2.9×10^{-7} moles/m^2) which, upon exposure to nitrogen, desorbed completely either as H_2S or as elemental sulfur, indicating that only H_2S chemisorption takes place on the support. Almost 57 % of the adsorbed H_2S desorbed as elemental sulfur, produced by decomposition of the adsorbed H_2S.

Sulfidation tests were also performed with another sorbent called CAT-NZ, which is UCI alumina containing 1.69 wt% of Zn. The properties of this UCI alumina are given in Table 1 of Chapter V. Figure 3 shows breakthrough curves for this sorbent. Under dry conditions (cycles 1,4), considerable loss of zinc by evaporation was observed in a form of deposits on the cooler parts of the reactor. AA analysis was used to confirm that these deposits contained zinc. Consequently, the H_2S absortion capacity of this supported ZnO dropped rapidly in consecutive cycles.

The H_2S breakthrough curve corresponding to cycle 3 in Figure 3 was ob-

tained with 6.5 mol% H_2O in the sulfidation gas, which contained 2530 ppm H_2S. The drastic drop in breakthrough conversion is mainly due to the large H_2O/H_2S ratio. Similar results were obtained with the sorbent CAT-NZ2, which had a higher loading of ZnO (3.2 Zn wt %)on the same UCI alumina [1]. Water has been found to have a strong effect on sorbent adsorbing behaviour. Interrupting the flow of H_2O in the feed after breakthrough time caused a drop of H_2S concentration at the outlet to low values comparable to those obtained in the absence of H_2O.

Desorption using a nitrogen purge was carried out for CAT-15Z and MCB alumina. The outlet H_2S concentrations are shown in the semi-logarithmic plot of Figure 4. In the case of the alumina, the outlet concentration increases for a few minutes and reaches a maximum. After that, the plot corresponds to the sum of two negative exponential terms. The straight line changes slope abruptly at about 45 minutes. This behavior of the support needs further study.

Regeneration of CAT-15Z was performed with 1-2 % of air in nitrogen. An initial rapid increase in both H_2S and SO_2 concentrations was observed, reaching values beyond the range of GC calibration curves. After a few minutes, the concentrations of both components decayed rapidly. After regeneration, if the system was left under N_2 purge, the SO_2 outlet concentration increased, reaching a maximum and then decaying slowly. This behavior is related to $ZnSO_4$ decomposition, which could follow an autocatalytic mechanism of decomposition, as was mentioned earlier. Instead, if the system is treated with H_2, $ZnSO_4$ is reduced rapidly to ZnO and smaller amounts of ZnS. The secondary production was shown by passing a mixture of air-N_2 through the reduced bed. During this treatment SO_2 was detected at the bed outlet, which can come only from ZnS oxidation.

Regeneration steps were carried out for CAT-NZ using diluted air, observing a behavior similar to that of CAT-15Z. For this sorbent, exploratory regenerations using a diluted air-H_2O mixture were performed. No evidence of $ZnSO_4$ formation was found, confirming that water somehow inhibits sulfate formation.

REFERENCES

1.-: Stephanopoulos M.F., Gavalas G.R., Tamhankar S.S., Sharma P.K., *Final Report to DOE. DOE/MC/20417-1898.* **1985.**

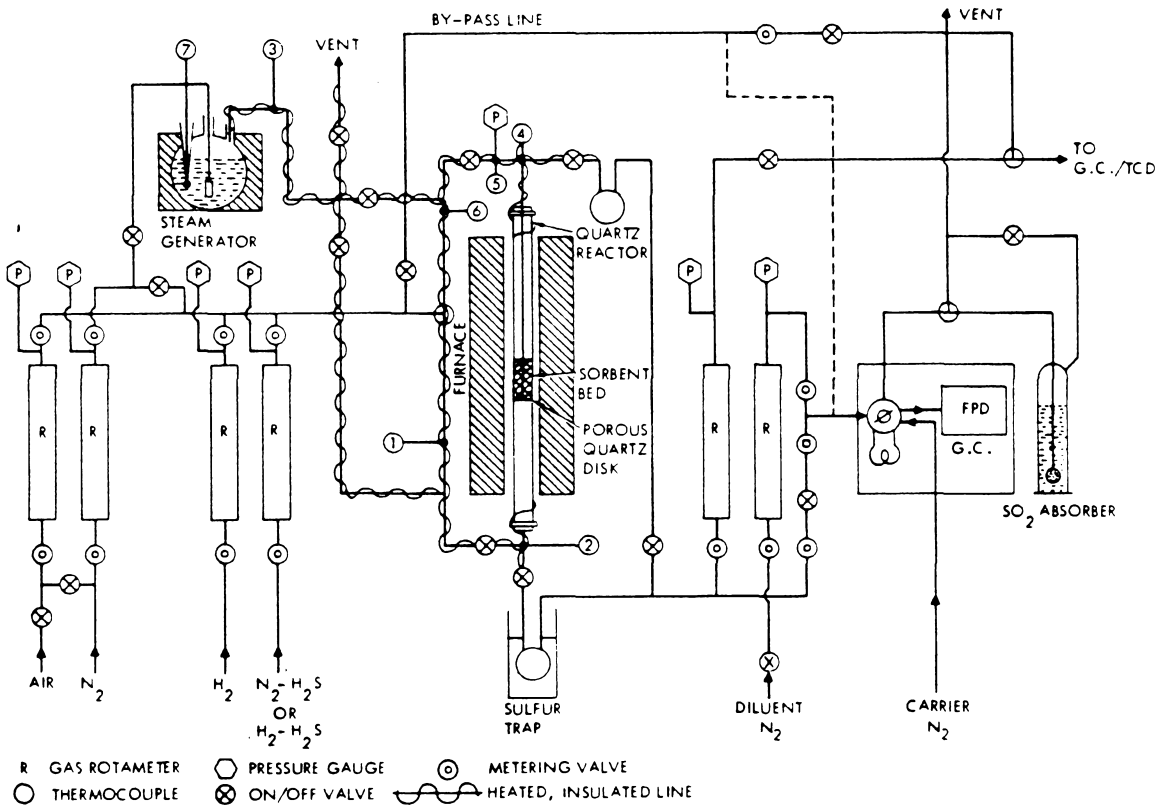

Figure 1.- Reactor System for Sulfidation-Regeneration Studies.

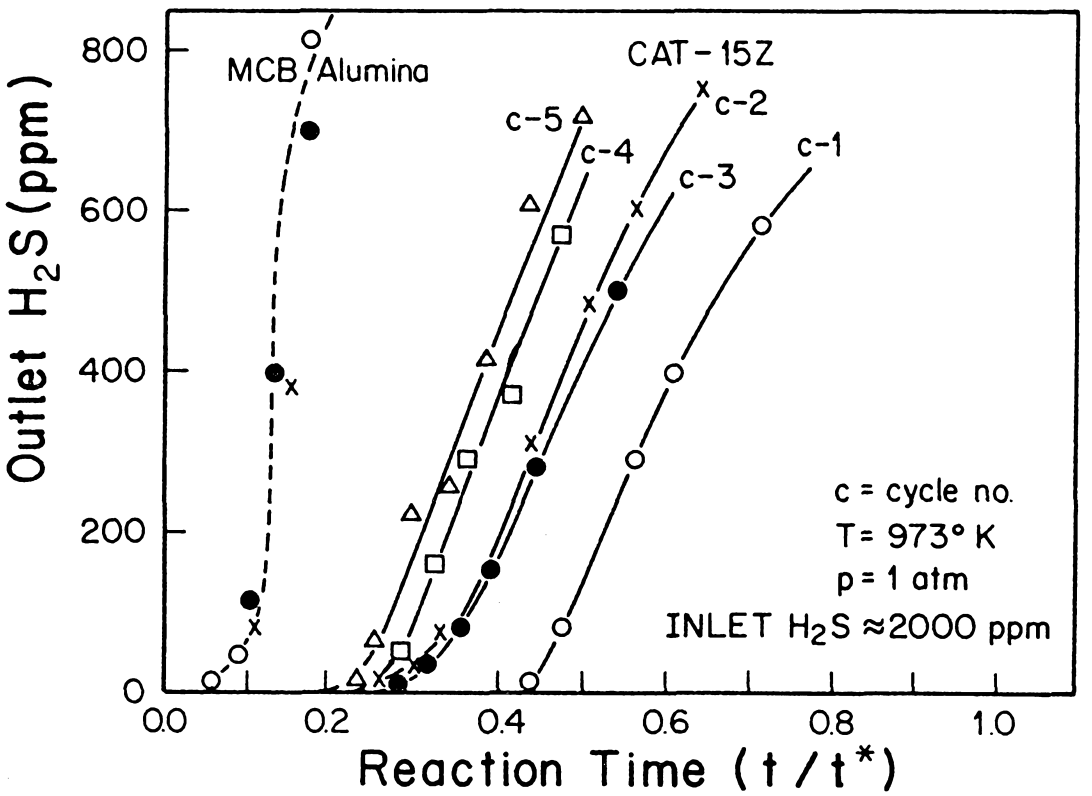

Figure 2: Breakthrough Curves for CAT-15Z and MCB Alumina.

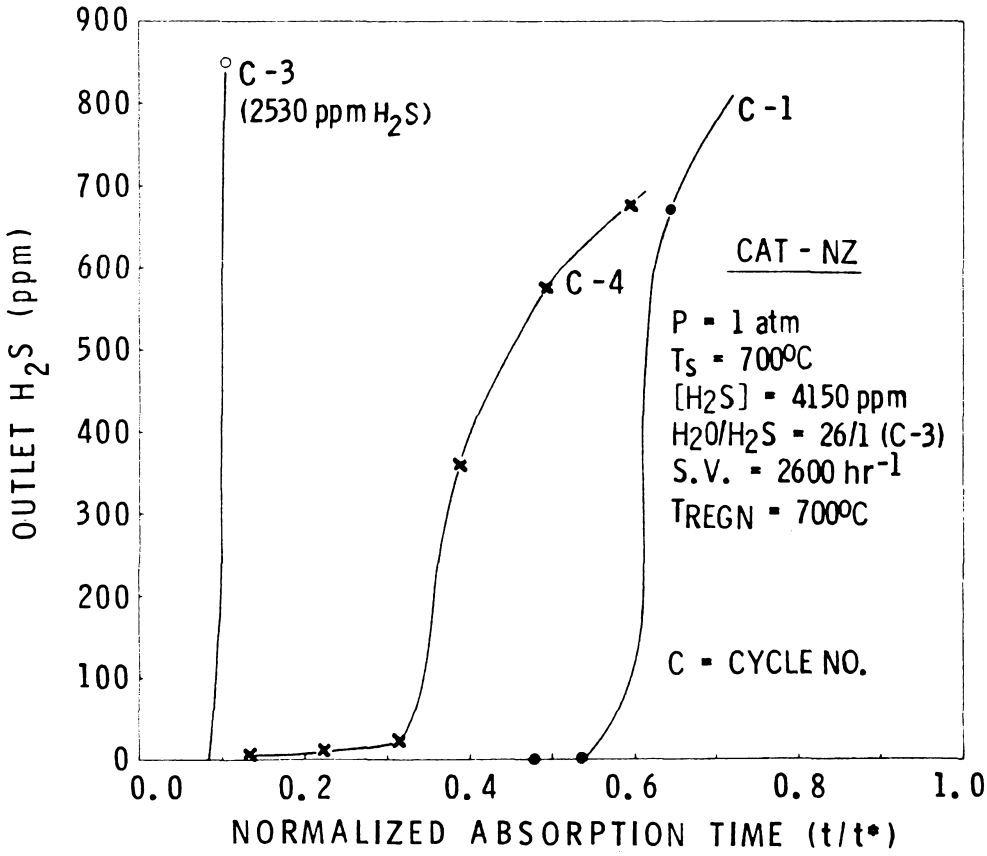

Figure 3.- Breakthrough Curves for CAT-NZ.

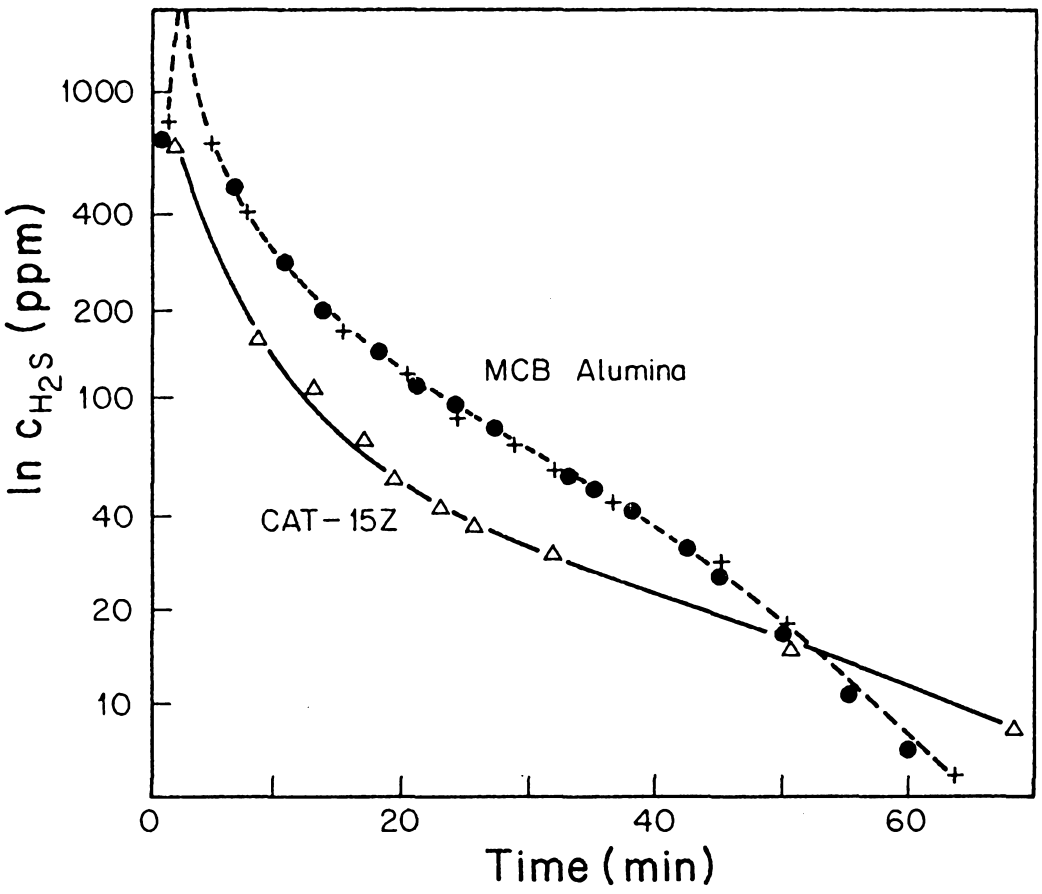

Figure 4: Semilogarithmic Plot for Desorption of CAT-15Z and MCB Alumina.

CHAPTER IV

There are those who believe that destiny rests on the knees of the gods ; but the truth is that it confronts the conscience of men with a burning challenge.

Eduardo Galeano

The content of this chapter was published as a paper in the Journal *Ind. & Eng. Chem., Proc. Des. and Dev.* It deals with the desulfurization performance of pure and mixed oxides at high temperatures. Results for high surface bulk ZnO show that this form of ZnO has a larger desulfurization capacity than the alumina-supported ZnO. For this reason the regeneration studies reported in chapter VI, were done on bulk ZnO.

Reprinted from I&EC PROCESS DESIGN & DEVELOPMENT, 1986, 25, 429.

Mixed-Oxide Sorbents for High-Temperature Removal of Hydrogen Sulfide

S. S. Tamhankar,† M. Bagajewicz, and G. R. Gavalas

Department of Chemical Engineering, California Institute of Technology, Pasadena, California 91125

P. K. Sharma and M. Flytzani-Stephanopoulos*

Jet Propulsion Laboratory, California Institute of Technology, Pasadena, California 91109

Several pure and mixed oxides (ZnO, CuO, $ZnO-Fe_2O_3$, $CuO-Fe_2O_3$, $CuO-Al_2O_3$, and $CuO-Fe_2O_3-Al_2O_3$) were investigated as regenerable sorbents for the removal of H_2S at high temperatures. A special technique was used to prepare the sorbents in highly porous form. The sorbents were subjected to successive sulfidation–regeneration cycles in a packed-bed microreactor. Sulfidation was carried out at 538–650 °C with $H_2S-H_2O-H_2-N_2$ mixtures, regeneration with $O_2-N_2-H_2O$ mixtures. Fresh, sulfided, and regenerated sorbents were characterized by XRD, SEM-EDS, and BET surface area analysis. Solid conversion and the prebreakthrough exit concentration of H_2S are discussed in terms of physical structure and thermodynamic properties of the sorbents. The performance of the sorbents $CuO-Fe_2O_3$, $CuO-Al_2O_3$, and $CuO-Fe_2O_3-Al_2O_3$ is discussed in terms of changes in the oxidation state of copper during sulfidation.

Coal-derived gas used in power generation must be substantially free of H_2S and other sulfur compounds deriving from the gasification of coal. The sulfur content must be reduced from several thousand parts per million (ppm) to a few hundred parts per million for combined-cycle and to only 1 ppm for molten carbonate fuel cell power generation. In the former case, the H_2S level is dictated by environmental regulations, while in the latter by the need to avoid fouling of the electrodes. Well-established desulfurization processes operate at ambient temperatures and entail considerable efficiency loss in the cooling and reheating of the fuel gas. The thermal efficiency of the power cycle can be substantially improved by carrying out the sulfur removal at high temperatures.

A number of studies have been reported over the last decade on high-temperature H_2S removal, primarily using

* To whom all correspondence should be addressed. Presently with the Department of Chemical Engineering, Massachusetts Institute of Technology, Cambridge, MA 02139.

† Presently with the BOC Group, Inc., Technical Center, Murray Hill, NJ 07974.

0196-4305/86/1125-0429$01.50/0

430 Ind. Eng. Chem. Process Des. Dev., Vol. 25, No. 2, 1986

various transition-metal oxides as sorbents. Comparative evaluations of various oxide sorbents have been published in Department of Energy reports (e.g., MERC, 1978) and in journals (e.g.: Westmoreland and Harrison, 1976; Westmoreland et al., 1977).

The sorbent most intensively studied is iron oxide, which yields equilibrium H_2S concentrations in the humdred parts per million range for a composition representative of low British thermal unit coal-derived gas and temperatures 500–800 °C. Recent experimental work has examined the performance of various iron oxide-based sorbents (Oldaker et al., 1975; Oldaker and Gillmore, 1976; Schrodt, 1980; Grindley and Steinfeld, 1981). The last reference examines the properties of iron oxide alone or in combination with zinc oxide, in the form of the compound zinc ferrite.

Zinc oxide has been used as a nonregenerable sorbent in "guard beds" protecting catalyst beds from trace sulfur impurities. More recently, zinc oxide has also been investigated as a regenerable sorbent (MERC, 1978; Giner, 1981; Grindley and Steinfeld, 1981). The thermodynamic equilibrium for sulfidation of ZnO is quite favorable, yielding purification down to a few parts per million H_2S. The sulfidation kinetics of ZnO, however, are much slower compared to those of iron oxide, and the regenerability of ZnO is restricted by loss of surface area at high regeneration temperatures and formation of zinc sulfate at low regeneration temperatures. Quite recently, zinc ferrite ($ZnFe_2O_4$) has been found to possess sulfidation equilibria comparable to ZnO but somewhat better capacity and regenerability (Grindley and Steinfeld, 1981). A difficulty with all sorbents containing zinc oxide is the reduction to volatile elemental zinc at temperatures above 600 °C.

Sorbent properties important in the applications are (i) the degree of H_2S purification of the treated gas and the sulfur loading of the sorbent, (ii) regenerability of the sorbent, (iii) the composition of the regeneration off-gas, and (iv) the mechanical strength of the sorbent. In this paper, we are concerned primarily with properties (i) and (ii). The chemistry of regeneration is important in its own right but will not be considered here in any detail. The experiments have employed conditions adequate for complete regeneration but have not attempted to delineate mechanisms or optimize the composition of the regeneration off-gas.

The chemistry of a complete sulfidation–regeneration cycle may be represented by the overall reactions

reduction

$$MO_x \xrightarrow{H_2, CO} MO_y \qquad (y \leq x) \tag{1}$$

sulfidation

$$MO_y + yH_2S = MS_y + yH_2O \tag{2}$$

regeneration

$$MS_y \xrightarrow{O_2} M(SO_4)_x \rightarrow MO_x + xSO_2 \tag{3}$$

where M is a metal Fe, Zn, Cu, etc.

Reduction and sulfidation take place simultaneously when the sorbent is contacted with the hot fuel gas. Regeneration can be conducted by air or air–steam mixtures where the chemistry is more complicated than shown by reaction 3, with elemental sulfur and H_2S produced in addition to SO_2.

When reaction and diffusion rates are sufficiently rapid, the sorbent sulfur capacity and the extent of purification are determined by thermodynamics alone. With many sorbents, however, the rate of reaction, or pore diffusion, or diffusion in the product layer limits sorbent capacity and the degree of purification under practical conditions. Such is the case with some commercial ZnO sorbents where reported conversions at breakthrough have been less than 20%.

Recent research has shifted from pure oxides to mixed oxides with the goal of improving sorbent performance. As mentioned above, zinc ferrite has been found to possess better capacity and regenerability than pure zinc oxide (Grindley and Steinfeld, 1981). Mixed ZnO–CuO has been studied for its better resistance to surface area loss (Jalan, 1983), and various other mixtures including $ZnO–Cr_2O_3$ and $ZnO–Al_2O_3$ have been studied with the objective of increasing the yield of elemental sulfur during regeneration (Anderson and Garrigan, 1982). Mixed oxides form various distinct crystalline phases or solid compounds and should generally possess different thermodynamic properties and reactivity with respect to reactions 1–3 above. This rather intriguing aspect of the problem has received limited attention so far.

In this paper, we report results on pure and mixed-oxide sorbents prepared by a special technique as highly porous materials. The sorbents studied include ZnO, CuO, $ZnO–Fe_2O_3$, $CuO–Fe_2O_3$, $CuO–Al_2O_3$, and $CuO–Fe_2O_3–Al_2O_3$. These sorbents have exhibited high H_2S removal efficiency and large sulfur capacity. The copper-based mixed oxides, in particular, have yielded H_2S concentrations well below those corresponding to their pure oxide constituents. Experiments and discussion are largely concerned with explaining sorbent performance in terms of changes in phase composition and surface area during successive sulfidation–regeneration cycles.

Experimental Section

Sorbent Preparation and Characterization. Sorbent preparation was carried out by a general method for synthesizing highly porous mixed oxides (Marcilly et al., 1970). According to this method, an aqueous solution containing the metal salts in desired proportion, and an organic polyfunctional acid with at least one hydroxy and one carboxylic function, is rapidly dehydrated under vacuum at about 70 °C. The resulting amorphous solid foam is calcined at high temperature (usually 500–600 °C) to form the mixed-oxide phase. The crystallized mixed oxides thus formed are homogenous and highly porous.

This method was used to prepare bulk pure oxides (ZnO and CuO) as well as the mixed oxides $ZnO–Fe_2O_3$ (ZF), $CuO–Fe_2O_3$ (CF), $CuO–Al_2O_3$ (CA), and $CuO–Fe_2O_3–Al_2O_3$ (CFA). All these materials were prepared as dispersed microcrystalline solids with high porosity. X-ray diffraction (XRD) analysis of the crystalline phases of these mixed-oxide sorbents was performed by using a Cu $K\alpha$ source on a Siemens Allis D500 instrument. Scanning electron microscopy (SEM) was used to observe the porous surface of the sorbents. The surface areas were measured in a Quantasorb flow BET apparatus. Mercury porosimetry was used to measure pore volumes and obtain the pore size distribution of selected sorbents. Table I lists the physical characteristics and crystalline phases of the fresh sorbents prepared in this work. The mixed oxides $ZnO–Fe_2O_3$ and $CuO–Fe_2O_3$ had the ferrite-spinel structure, $ZnFe_2O_4$ and $CuFe_2O_4$, respectively, while $CuO–Al_2O_3$ consisted of the aluminate-spinel $CuAl_2O_4$, CuO, and an amorphous phase. The CFA sorbent consisted of crystalline CuO, $FeAl_2O_4$, $CuFe_2O_4$, and an amorphous phase. Table II gives the results of XRD analyses of selected fresh, sulfided, and regenerated sorbent materials.

The phase composition given in Table II is only qualitative due to the nature of the technique and the presence

Ind. Eng. Chem. Process Des. Dev., Vol. 25, No. 2, 1986 431

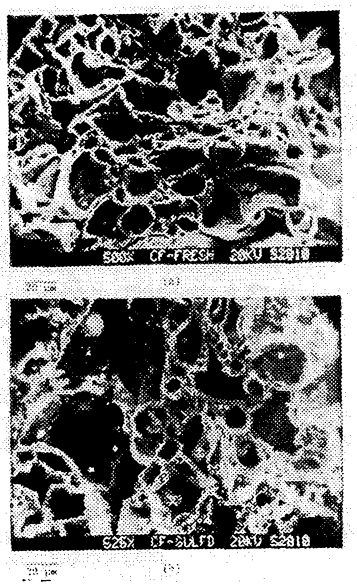

Figure 1. Scanning electron micrographs of porous copper ferrite: (a) fresh; (b) sulfided at 650 °C, two cycles.

of certain amorphous phases. In the Al_2O_3-containing sorbents, a large amount of an amorphous (to XRD) phase was typically present, even before reaction. Based on material balances, this phase was comprised of aluminum compounds. The calcination conditions (temperature, exposure time) are critical for the type and amount of

Table I. Properties of Fresh Sorbents Used in Sulfidation Experiments

sorbent designation	composition, molar ratio	pore surface area, m^2/g	pore vol, cm^3/g	crystalline phases
ZF	ZnO/Fe_2O_3 (1:1)	17	1.9	$ZnFe_2O_4$
ZnO	ZnO	7	NA	ZnO
CF	CuO/Fe_2O_3 (1:1)	7–10	NA	$CuFe_2O_4$
CA	CuO/Al_2O_3 (1:1)	12	NA	$CuAl_2O_4$, CuO
CuO	CuO	NA	NA	CuO
CFA	$CuO/Fe_2O_3/Al_2O_3$ (2:1:1)	26	1.0	CuO, $CuFe_2O_4$, $FeAl_2O_4$

stable crystalline phases formed in these sorbents. In Table II, "sulfided" indicates sorbent treatment with a H_2S–H_2O–H_2–N_2 gas mixture, while "reduced" indicates treatment with a H_2–H_2O–N_2 mixture. The SEM analyses provided information about the porous structure of the sorbents. As an example, Figure 1 shows SEM micrographs of fresh and sulfided CuO–Fe_2O_3 sorbents. The micrographs show very large (>10 μm) as well as submicrometer size pores with similar structure before and after sulfidation. Typically, all porous sorbents used here had surface areas in the range of 10–40 m^2/g, small crystallite size, and large pore volume. For example, the porous $ZnFe_2O_4$ with 17 m^2/g surface area had an average crystallite size of 890 Å (as measured by low-angle XRD). The pore volume of this material was 1.9 cm^3/g with pore sizes greater than 10 μm accounting for 63% (1.2 cm^3/g) of its total pore volume.

Apparatus and Procedure. The experiments were performed in the reactor system shown in Figure 2. The reactor consisted of a quartz tube, 1 cm i.d. × 41 cm length,

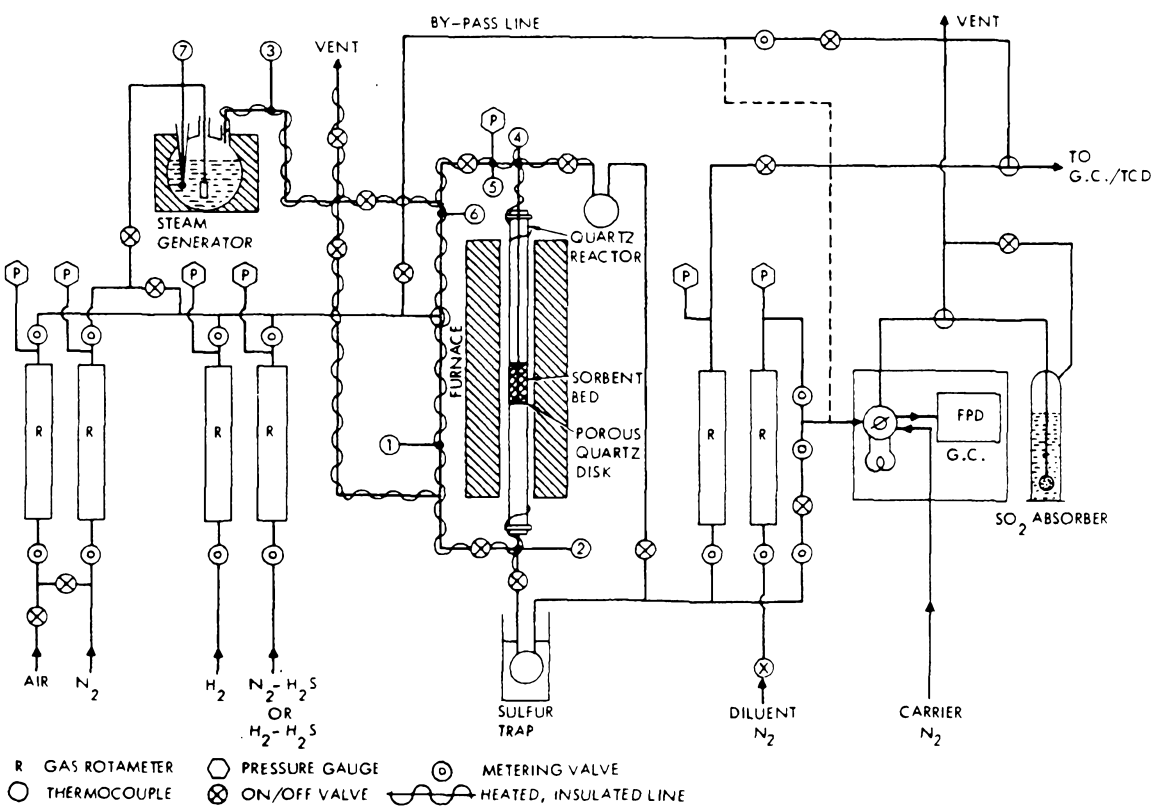

Figure 2. Experimental reactor system.

Table II. Crystalline Phases and Surface Areas of Various Sorbents

sorbent	crystalline phases.[a] (wt %)	surface area, m^2/g
ZF, fresh	$ZnFe_2O_4$ (100)	17.0
ZF, sulfided (538 °C, 6 cycles)	β-ZnS (83), $Fe_{1-x}S$ (17)	3.0
ZF, regenerated (700 °C, 6 cycles)	$ZnFe_2O_4$ (81), Fe_2O_3 (19)	6.0
CF, fresh	$CuFe_2O_4$ (100)	7.0
CF, reduced (538 °C, 30 min)	$CuFe_2O_4$ (14), Fe_3O_4 (43), Cu (43)	4.3
CF, sulfided (538 °C, 8 cycles)	$CuFe_2O_4$ (36), Fe_3O_4 (13), $CuFeS_2$ (32), $Fe_{1-x}S$ (19)	1.2
CF, sulfided (650 °C, 2 cycles)	Fe_3O_4 (36), $CuFe_2O_4$ (14), Cu (11), $Fe_{1-x}S$ (39)	1.0
CF, regenerated (700 °C, 2 cycles)	Fe_2O_3 (60), CuO (29), $CuFe_2O_4$ (11)	2.0
CA, fresh	$CuAl_2O_4$ (64), CuO (36)	12.0
CA, sulfided (538 °C, 5 cycles)	$CuAl_2O_4$ (69), Cu_7S_4 (31)	4.2
CA, regenerated (700 °C, 4 cycles)	CuO (66), $CuAl_2O_4$ (33)	7.0
CFA, fresh	CuO (37), $CuFe_2O_4$ (39), $FeAl_2O_4$ (24)	26.0
CFA, sulfided (650 °C, 4 cycles)	CuS (20), $Fe_{1-x}S$ (32), $CuFe_2S_3$ (48)	NA
CFA, sulfided (650 °C, 14 cycles)	$CuAl_2O_4$ (22), $CuFe_2O_4$ (34), $Cu_6Fe_9S_{16}$ (25), Cu (14), α-Al_2O_3 (5)	7.4
CFA, regenerated (650 °C, 14 cycles)	$CuAl_2O_4$ (21), $CuFe_2O_4$ (42), $CuAlO_2$ (9), α-Al_2O_3 (6), $Cu_6Fe_3O_7$ (15), $FeAl_2O_4$ (7)	4.2[b]

[a] The weight percentages are qualitative and refer only to total crystalline phases present. [b] Sample accidentally overheated to 800 °C during regeneration.

mounted vertically inside an electric furnace and instrumented with a K-type thermocouple moving inside a quartz thermowell (0.3 cm i.d) concentric to the reactor. The sorbents were loaded in the reactor as −20+40-mesh particles mixed, with low surface area zirconia or alumina particles serving as an inert filler. The use of the inert particles allows us to compress the experimental run time by decreasing the bed capacity, while maintaining the same space velocity. Different gases from cylinders passed through purifiers and then through calibrated flow meters into a common gas line. The gas mixture then passed through the reactor in the upward (sulfidation) or downward (regeneration) direction. The lines leading to the reactor were heated and insulated. Nitrogen bubbling through water maintained at constant temperature in a three-neck flask assembly was used to introduce known amounts of water vapor into the feed gas stream. Temperatures at various locations in the reactor system were monitored by K-type thermocouples connected to a multichannel digital readout. The reactor pressure in all cases was slightly above atmospheric.

The experiments consisted of alternating sulfidation and regeneration runs. In a sulfidation run, the sulfur-free sorbent was exposed to a feed gas containing H_2 (~20 mol %), H_2O (7–25 mol %), H_2S (0.2–1 mol %), and N_2 (balance). In a few tests with CuO–FeO_3–Al_2O_3 sorbents, the feed gas also contained CO and CO_2. The temperature was chosen in the range of 500–700 °C and was held fixed for the duration of sulfidation. Sulfided sorbents were regenerated by using nitrogen–air or nitrogen–air–steam mixtures at temperatures of 600–750 °C.

The product gas was passed through ice traps to condense any elemental sulfur formed and was analyzed for H_2S and SO_2 by a HP 5830-A gas chromatograph equiped with a flame photometric detector. The column was 6 ft × $^1/_8$ in. o.d. Teflon tubing packed with Chromosil 310 (Supelco Inc.) and was operated isothermally at 50 °C. By using an automated valve system, samples could be analyzed every 2 min during sulfidation to provide time-resolved composition. The tubing downstream of the reactor consisted of Teflon-coated stainless steel to avoid H_2S adsorption.

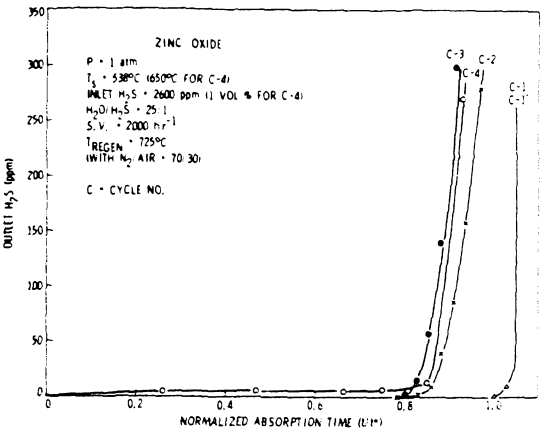

Figure 3. Breakthrough curves in successive sulfidation cycles of zinc oxide.

Results and Discussion

In this section, we present hydrogen sulfide breakthrough curves for the sulfidation of each of the sorbents listed in Tables I and II. These results are discussed in terms of solid-phase transformations observed during sulfidation.

In a typical sulfidation experiment, the concentration of hydrogen sulfide in the product gas rises very slowly at first until a certain time after which it rises rapidly to the inlet value. The time of this abrupt change in slope is called the breakthrough time, and the concentration vs. time curve is sometimes called the breakthrough curve. In the absence of transport and kinetic limitations, the breakthrough curve would be the step function $y = y^{eq}$ at $t < t^*$ and $y = y^0$ at $t > t^*$, where y^{eq} and y^0 are the equilibrium and inlet mole fractions of hydrogen sulfide, and t^* is the theoretical breakthrough time, i.e., the time required for complete sulfidation of the sorbent. Finite reaction and diffusion rates, axial dispersion, and channeling produce experimental breakthrough curves that are smoothly sloping. The fractional conversion at the actual breakthrough time provides a measure of sorbent utilization efficiency, while the level of H_2S before breakthrough is also an important measure of sorbent performance. The results below are presented in terms of the mole fraction of H_2S in the product gas vs. the normalized time t/t^*. Each figure includes several breakthrough curves corresponding to successive sulfidation cycles denoted by C-1, C-2, etc. The conditions for regeneration between sulfidations are also listed in each case.

Zinc Oxide. During sulfidation, this sorbent undergoes undesirable reduction

$$ZnO + H_2 = Zn + H_2O \quad (4)$$

in addition to sulfidation

$$ZnO + H_2S = ZnS + H_2O \quad (5)$$

Figure 3 presents successive sulfidation cycles, each followed by regeneration with an air–nitrogen mixture (30:70 molar) at 725 °C. In the first three cycles, carried out at

538 °C, the sorbent conversion at breakthrough was above 0.85 with the outlet H_2S level before breakthrough below the equilibrium value of 1.2 ppm for reaction 5. However, because at this low level the measurement error is significant, sulfidation was repeated on a fresh sorbent sample, with a feed gas containing a higher amount of steam (25 mol %). The breakthrough curve C-1′ essentially coincided with C-1 with the prebreakthrough H_2S level remaining below 1 ppm, compared to the equilibrium level of 4.2 ppm. One possible explanation for such subequilibrium concentrations is chemisorption of H_2S forming a surface sulfide layer with substantially lower free energy than the bulk sulfide. Dramatic differences in the thermodynamic properties of surface and bulk sulfides have been reported for the case of nickel (Rostrup-Nielsen, 1975).

In sulfidation C-4, the temperature was raised to 650 °C and the mole fractions of H_2O and H_2S were increased to 25% and 1%, respectively. The breakthrough sorbent conversion was still 0.8 and the prebreakthrough H_2S level was 6–8 ppm, below the equilibrium level of 16 ppm. At this temperature, zinc deposits were observed on the quartz tube wall downstream of the bed, indicating loss by reduction (reaction 4) and evaporation.

Previous work on the ZnO–H_2S reaction was carried out with commercial sorbents in pellet form. ZnO pellets of 28 m^2/g surface area and 0.3 cm^3/g pore volume were tested at 650 °C with very high space velocity (19 000 h^{-1}) but with no H_2O in the sulfidation gas (Giner, 1981). Very low sorbent conversions, 0.05–0.12, were obtained, reflecting drastic reduction in pore volume and surface area during sulfidation. Another commercial ZnO sorbent in the form of pellets of 3 m^2/g surface area and 0.26 cm^3/g pore volume was tested in sulfidation with a simulated coal-derived gas (Grindley and Steinfeld, 1981). At 538 °C, conversion at breakthrough was lower than 0.20, while the prebreakthrough H_2S level was 1–3 ppm. Sulfidation again caused drastic reduction in surface area and pore volume. The higher conversion obtained in this work is partly attributed to the small size (−20+40-mesh particles) of the sorbent. The main contribution to the observed high sorbent conversion, however, comes from the different porous structure of the material, especially its much higher pore volume. In view of the significant increase of molar volume during sulfidation, sorbents with high initial pore volume would be less susceptible to pore mouth blocking.

Zinc Ferrite. Extensive laboratory and bench-scale tests with zinc ferrite have been performed at the Morgantown Energy Technology Center (METC) of the Department of Energy with a synthetic sorbent prepared by United Catalysts, Inc. by heating powders of ZnO and Fe_2O_3 at 815 °C. A pelleted form of this sorbent, designated here as METC-ZF, with 6 m^2/g surface area and 0.29 cm^3/g pore volume yielded prebreakthrough H_2S levels of 2–10 ppm at sorbent conversion of ~0.20 with a simulated coal-gasifier feed gas (Grindley and Steinfeld, 1981).

The performance of the porous zinc ferrite ZF synthesized in this work with high surface area and large pore volume was tested in the quartz microreactor and compared to the METC-ZF sorbent at the same operating conditions. Both sorbents were used as −20+40-mesh particles mixed with low surface area alumina particles. Sulfidation at 538 °C yielded prebreakthrough conversion of 0.75 or higher for ZF and 0.35–0.40 for METC-ZF. Both sorbents were capable of removing H_2S from ~2500 ppm to less than 1 ppm level with a feed gas containing 20 mol % H_2 and 6.5 mol % H_2O. The higher conversion of ZF must be attributed to its different physical properties.

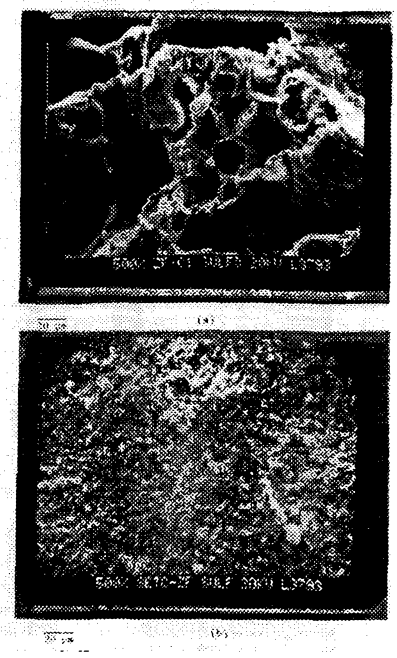

Figure 4. SEM micrographs of zinc ferrite sorbents sulfided at 538 °C: (a) porous ZF sorbent; (b) METC-ZF sorbent.

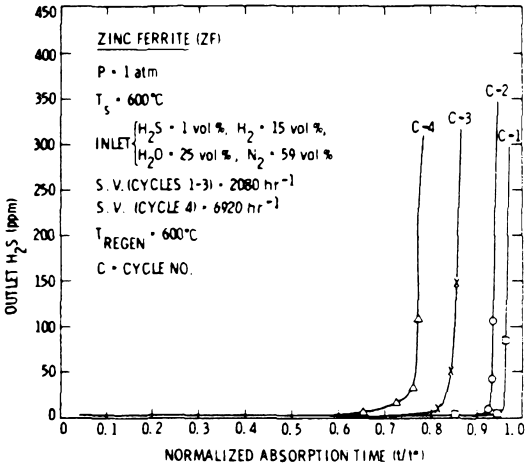

Figure 5. Breakthrough curves in successive sulfidation cycles of zinc ferrite (ZF).

Figure 4 shows SEM micrographs of the sulfided ZF and METC-ZF sorbents. The pore structure of the two is very different, with METC-ZF lacking the large pores of ZF. The gross morphological features of the latter were the same before and after sulfidation, indicating high accessibility to H_2S and limited or no pore mouth blocking.

Similarly, high conversion (>0.75) was obtained with ZF at all temperatures in the range 538–650 °C with the sulfidation gas containing 15–20% H_2, 7–25% H_2O, and 0.2–1.0% H_2S, balance N_2 by volume. Figure 5 shows H_2S breakthrough curves for the ZF sorbent at 600 °C sulfidation/regeneration. Very sharp breakthrough curves, indicative of fast reaction and diffusion rates, are observed. The breakthrough conversion gradually declined from 0.95 in C-1 to 0.7 in C-4, while the prebreakthrough H_2S level remained at 2–3 ppm. A slow decline in breakthrough

Table III. Equilibria of Sulfidation and Reduction Reactions[a]

reaction	temp, °C	K_p[b]	Y_{H_2S}, ppm Y_{H_2O} = 0.07	Y_{H_2S}, ppm Y_{H_2O} = 0.25
4	538	3.8×10^{-7}	1.1[c]	0.3[c]
	650	2.2×10^{-6}	61.4[c]	17.2[c]
5	538	5.96×10^{4}	1.2	4.2
	600	2.71×10^{4}	2.6	9.2
	650	1.55×10^{4}	4.5	16.1
6	538	2.08×10^{3}		
	600	2.97×10^{3}		
	650	3.84×10^{3}		
7	538	7.99×10^{11}	5.3	29.0
	600	2.41×10^{11}	7.9	48.3
	650	1.03×10^{11}	10.5	57.5
8	538	1.07×10^{9}	48.2	263
	600	5.05×10^{8}	55.3	302
	650	2.76×10^{8}	75.8	414
9	538	4.35×10^{3}	46.0	46.0
	650	2.18×10^{3}	91.7	91.7
10	538	3.95×10^{18}		
	650	2.24×10^{16}		
11	538	1.22×10^{9}		
	650	4.32×10^{8}		
12	538	1.64×10^{8}	5.5	19.5
	650	2.53×10^{7}	13.9	49.7
13	538	5.20×10^{15}	0.3	1.6
	650	5.28×10^{14}	0.6	3.3
16a	538	5.70×10^{7}	0.001	0.004
	650	7.04×10^{6}	0.01	0.036
16b	538	5.11×10^{9}	1.4×10^{-5}	4.9×10^{-5}
	650	6.05×10^{8}	1.2×10^{-4}	4.1×10^{-4}

[a] With 20 mol % H_2 in the feed gas. [b] Equilibrium constants were calculated from the thermodynamic data from Barrin and Knacke (1973). [c] Equilibrium Y_{Zn} in ppm.

conversion was also observed at 650 °C sulfidation temperature.

Similarly to zinc oxide, sulfidation of zinc ferrite at 600 and 650 °C produced deposits on the cooler tube walls downstream of the bed which were found by atomic absorption (AA) to contain zinc. At the conditions of Figure 5, the rate of zinc loss from the sorbent was measured by AA to be 8 and 26% per 1000 h at space velocities of 2100 and 6900 h^{-1}, respectively. The corresponding mole fraction of zinc vapor in the gas phase was approximately 1.3 ppm, close to the equilibrium for reaction 4. Therefore, at temperatures above 600 °C, ZnO reduction is at equilibrium. The decline in conversion with successive sulfidation cycles observed in Figure 5 is due to evaporative loss of zinc as well as loss of surface area. During experiments at 538 °C, the sorbent conversion dropped from 1.0 in the first cycle to 0.8 in the sixth cycle, while the surface area changed from 17 to 6 m^2/g (Table II). At this temperature, the loss of zinc by reduction and evaporation is negligible.

Since zinc ferrite has a crystalline structure distinct from zinc oxide, we must inquire about the relevance of reaction 5 in the thermodynamics and kinetics of sulfidation of the zinc ferrite sorbent. The reactions that are thermodynamically feasible during contact with the sulfiding gas (H_2–H_2O–H_2S–N_2) include

$$3ZnFe_2O_4 + H_2 = 3ZnO + 2Fe_3O_4 + H_2O \quad (6)$$

$$ZnFe_2O_4 + 3H_2S + H_2 = ZnS + 2FeS + 4H_2O \quad (7)$$

$$ZnO + H_2S = ZnS + H_2O \quad (5)$$

$$Fe_3O_4 + 3H_2S + H_2 = 3FeS + 4H_2O \quad (8)$$

with the equilibrium constants at 538 and 600 °C listed in Table III.

The observed prebreakthrough H_2S level of 2–3 ppm is below the 9 ppm equilibrium level for reaction 5, the most favorable among the three sulfidation reactions (5), (7), and (8). Hence, formation of some surface sulfide must be at work, and it cannot be decided on the basis of these data whether ferrite decomposition according to reaction 6 precedes sulfidation. The regenerated sample contains Fe_2O_3, and perhaps amorphous ZnO, in addition to $ZnFe_2O_4$; hence, the formation of zinc ferrite from the individual oxides does not proceed to completion during the limited time of regeneration.

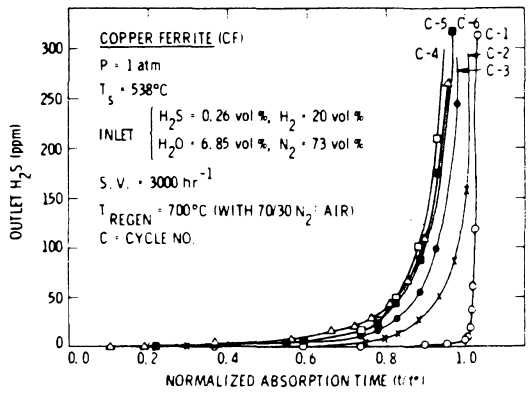

Figure 6. Breakthrough curves in successive sulfidation cycles of copper ferrite (CF).

Copper Ferrite. Copper ferrite was investigated with the hope of avoiding two difficulties that arise with zinc-based sorbents, namely the loss of metallic zinc at temperatures above 600 °C and the high temperatures required for decomposition of zinc sulfate formed during regeneration.

Cupric oxide by itself is known to reduce to the metal under the conditions of temperature and feed composition employed. Metallic copper, in turn, is sulfided according to

$$2Cu + H_2S = Cu_2S + H_2 \quad (9)$$

For a gas with 20 mol % H_2, the equilibrium H_2S level is 46.0 ppm at 538 °C and 91.7 ppm at 650 °C (Table III). Although these levels are quite high, it was thought that the equilibrium with copper ferrite could be lower because of its different crystal structure.

The copper ferrite sorbent was prepared with the technique described earlier and had the properties listed in Table I. The breakthrough curves in several sulfidation cycles at 538 °C are presented in Figure 6. In the first sulfidation, conversion was complete. In five subsequent sulfidations, the breakthrough sorbent conversion stabilized to about 0.75. In all cases, the prebreakthrough H_2S level was well below the value of 46.0 ppm calculated for the equilibrium of reaction 9. In fact, the H_2S level remained below 2 ppm until 0.5 conversion and then gradually increased to ~10 ppm when conversion reached 0.78. In two sulfidation/regeneration cycles carried out at 600 °C, subequilibrium H_2S levels were again measured until breakthrough, which occurred at ~0.80 sorbent conversion. At 650 °C sulfidation temperature, however, while a similarly high and stable sorbent conversion took place, the prebreakthrough H_2S level at 0.80 sorbent conversion was 85–90 ppm, close to the equilibrium for reaction 9. Still, the exit H_2S level remained below its equilibrium value up to 0.20 sorbent conversion.

Characterization of fresh, sulfided (in H_2S–H_2O–H_2–N_2), reduced (in H_2–H_2O–N_2), and regenerated (in O_2–N_2) samples of CF sorbents was performed by SEM and XRD analyses. SEM micrographs of the sorbent before and after

sulfidation were presented earlier in Figure 1. XRD analysis of the sorbent provided the results listed in Table II. The weight percentage figures are only qualitative and refer to the total crystalline phases. The reduced sample includes $CuFe_2O_4$; hence, reduction is not very fast at 538 °C. The sample sulfided at 538 °C contains the mixed-sulfide compound $CuFeS_2$ (chalcopyrite) along with $Fe_{1-x}S$, Fe_3O_4, unconverted $CuFe_2O_4$ and some amorphous material. In the sample sulfided at 650 °C, the phase $CuFeS_2$ is absent, while there is indication of a poorly crystalline Cu_2S phase. As in the case of zinc ferrite, copper ferrite formation from the individual oxides does not proceed to completion during regeneration.

The prebreakthrough H_2S levels and the phases observed in the XRD analyses may be discussed qualitatively in terms of the following thermodynamically feasible phase transformations

$$3CuFe_2O_4 + 2H_2 = 3CuFeO_2 + Fe_3O_4 + 2H_2O \quad (10)$$

$$3CuFeO_2 + 2H_2 = 3Cu + Fe_3O_4 + 2H_2O \quad (11)$$

$$CuFeO_2 + 2H_2S = CuFeS_2 + 2H_2O \quad (12)$$

$$2CuFeO_2 + 3H_2S + H_2 = Cu_2S + 2FeS + 4H_2O \quad (13)$$

$$2Cu + H_2S = Cu_2S + H_2 \quad (9)$$

$$Fe_3O_4 + 3H_2S + H_2 = 3FeS + 4H_2O \quad (8)$$

with equilibrium constants and corresponding H_2S concentrations listed in Table III (based on thermodynamic values given in Barrin and Knacke (1973)).

Reactions 10 and 11 represent the stepwise reduction of copper ferrite $CuFe_2O_4$ via the intermediate compound $CuFeO_2$ to the final products Cu and Fe_3O_4 which constitute the stable phases of Cu and Fe in the presence of the H_2–H_2O mixture employed. The equilibrium H_2S levels for reaction 12 were calculated by using thermodynamic values for the compound $Cu_2O{\cdot}Fe_2O_3$ (Barrin and Knacke, 1973). The absence of $CuFeO_2$ from the reduced and sulfided samples indicates that this intermediate compound is depleted relatively rapidly by reactions 11–13 to either the final reduction products Cu and Fe_3O_4 (reaction 11) or to the sulfided products $CuFeS_2$, Cu_2S, and FeS. The products of reduction, Cu and Fe_3O_4, are also sulfided to Cu_2S and FeS by reactions 9 and 8.

The prebreakthrough level of H_2S is determined by the thermodynamically most favorable among the sulfidation reactions (8), (12), (13), and (9), assuming that such reaction is sufficiently rapid. We note that the sulfidation of the intermediate compound $CuFeO_2$, containing copper at some oxidized state, is more favorable than that involving sulfidation of metallic copper, Cu^0. Reaction 12, although thermodynamically less favorable than (13), is kinetically much more favorable, for it requires no change of oxidation state and only minor rearrangement of the two cations. This hypothesis is consistent with phases found in the sample sulfided at 538 °C and with the prebreakthrough concentrations of H_2S in Figure 6. Chemisorption can be invoked once more to explain the subequilibrium H_2S levels during the first sulfidation.

At 650 °C, the compound $CuFeS_2$ was no longer present in the sulfided sorbent, possibly due to very rapid consumption of the precursor $CuFeO_2$ by reaction 11. In the absence of this intermediate product, sulfidation would proceed by reactions 8 and 9, of which (9) is more favorable and should control the prebreakthrough level of H_2S. This hypothesis is again consistent with observed H_2S concentrations of 90 ppm upon sulfidation at 650 °C—not included in Figure 6.

Copper Aluminate. In view of the superior performance of copper ferrite in comparison to its constituent pure oxides, another mixed oxide, copper aluminate, possessing the spinel structure was prepared and tested under the same conditions. The results presented in Figure 7 reveal some interesting features. In three sulfidations at 538 °C, the conversion at breakthrough was higher than 0.7, while the prebreakthrough H_2S level was lower than 10 ppm as compared to 46 ppm for the equilibrium of reaction 9. At 650 °C, on the other hand, the breakthrough curve has an odd shape. An initial near-zero level is succeeded at 0.15 sorbent conversion by a plateau at about 100 ppm, which terminates at a second breakthrough at 0.80 conversion. As shown in Table II, the fresh and regenerated sorbents contain the crystalline phases $CuAl_2O_4$ and CuO and some amorphous material, probably Al_2O_3. The sulfided sample contains unconverted copper aluminate, the nonstoichiometric phase Cu_7S_4 and some amorphous material. These results can be discussed in terms of the following reaction sequence

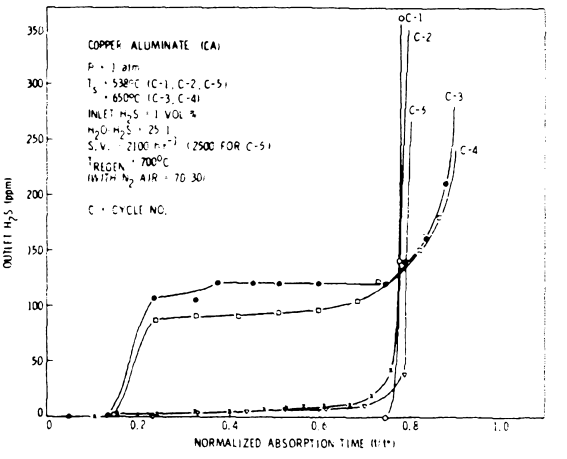

Figure 7. Breakthrough curves in successive sulfidation cycles of copper aluminate (CA).

$$xCuAl_2O_4 + (x-1)H_2 = Cu_xO{\cdot}Al_2O_3 + (x-1)Al_2O_3 + (x-1)H_2O \quad 1 \le x \le 2 \quad (14)$$

$$Cu_xO{\cdot}Al_2O_3 + H_2 = xCu + Al_2O_3 + H_2O \quad (15)$$

$$Cu_xAl_2O_3 + H_2S = Cu_xS + Al_2O_3 + H_2O \quad (16)$$

$$2Cu + H_2S = Cu_2S + H_2 \quad (9)$$

We again adopt the hypothesis that copper is reduced stepwise from the 2+ to the 1+ to the 0 oxidation state and that an intermediate copper compound is the key to low H_2S concentrations. At 538 °C, the intermediate copper compound represented as $Cu_xO{\cdot}Al_2O_3$ is maintained at sufficient concentration to control the exit level of H_2S all the way to 0.80 conversion. At 650 °C, on the other hand, reaction 15 is fast and by the time of 0.15 sorbent conversion, all copper has been completely reduced to its metallic form. From then on, the exit level of H_2S is controlled by reaction 9 up to the final breakthrough.

The intermediate copper compound has been represented as $Cu_xO{\cdot}Al_2O_3$, because its precise structure is unknown. All indications, however, point to the existence of a complex compound rather than the pure oxides Cu_2O or CuO. Firstly, XRD analysis has not identified Cu_2O. Secondly, sulfidation of pure CuO, prepared by the same technique as $CuAl_2O_4$, yielded H_2S concentrations corresponding to the equilibrium of reaction 9, indicating that CuO and Cu_2O are reduced very rapidly to Cu^0 in the

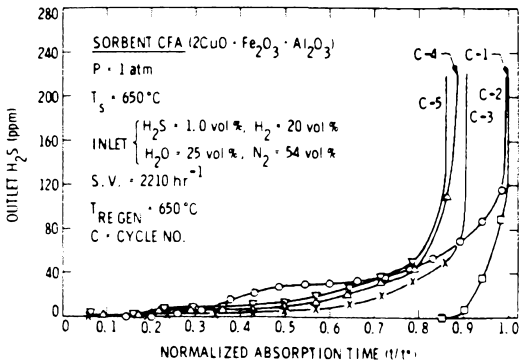

Figure 8. Breakthrough curves in successive sulfidation cycles of sorbent CFA at 650 °C.

presence of hydrogen. It is, thus, concluded that Cu^{2+} or Cu^{1+} are stabilized in the alumina matrix with respect to reduction. This stabilization also shifts the sulfidation equilibria. Thus, whereas the reactions

$$CuO + H_2S = CuS + H_2O \quad (16a)$$

$$Cu_2O + H_2S = Cu_2S + H_2O \quad (16b)$$

yield negligible equilibrium H_2S (Table III), the results in Figure 7 show small but finite prebreakthrough H_2S. Inhibition of the reduction of transition-metal oxides in close association with alumina has been amply documented in the case of nickel (e.g.: Gavalas et al., 1984).

Mixed $CuO–Fe_2O_3–Al_2O_3$ (CFA). In view of the enhanced stabilization of copper oxide in copper aluminate and copper ferrite sorbents, a mixed-copper ferrite–copper aluminate material with $CuO:Fe_2O_3:Al_2O_3$ = 2:1:1 molar ratio was prepared with 26 m^2/g surface area. Under similar operating conditions, this sorbent was superior to either copper ferrite or copper aluminate in regard to prebreakthrough H_2S levels, which were lower than the equilibrium of reaction 9 at all temperatures, 538–650 °C. An example is shown in Figure 8 for sulfidation at 650 °C with a gas containing 20 mol % H_2, 25 mol % H_2O, 1 mol % H_2S, and balance N_2. The performance was stable over five cycles of sulfidation/regeneration with prebreakthrough sorbent conversion of 0.75 and prebreakthrough H_2S levels in the range of 0–10 ppm up to 0.50 conversion and less than 35–40 ppm at breakthrough.

XRD analysis of the fresh and sulfided (after cycle 4) CFA sorbent was performed to identify crystalline phases that may be responsible for the improved performance of this sorbent. The fresh CFA consisted of $CuFe_2O_4$, CuO, and $FeAl_2O_4$, the latter in highly microcrystalline form. The remaining compounds were in an amorphous phase. The sulfided sample contained CuS, FeS, and $CuFe_2S_3$ along with an amorphous (to XRD) phase. These results indicate the stabilization of Cu^{1+} or Cu^{2+} in the sorbent matrix, resulting in improved sulfidation equilibria.

Additional testing of the CFA sorbent was conducted with a mixture containing 17% H_2, 12% CO, 10% CO_2, 24% H_2O, 0.5–1% H_2S, and balance N_2, simulating fuel gas from a Lurgi coal gasifier. The results were similar to those shown in Figure 8. A total of 14 cycles of sulfidation–regeneration were conducted at 650 °C. At the end of the 14th cycle, the surface area of the sulfided sorbent was 8 m^2/g and XRD analysis identified a nonstoichiometric mixed-sulfide $Cu_9Fe_9S_{16}$, along with $CuAl_2O_4$, $CuFe_2O_4$, and smaller amounts of Al_2O_3. In addition, there was a large amount of an amorphous phase which contained most of the sulfided compounds, in view of the overall stoichiometry and the conversion observed.

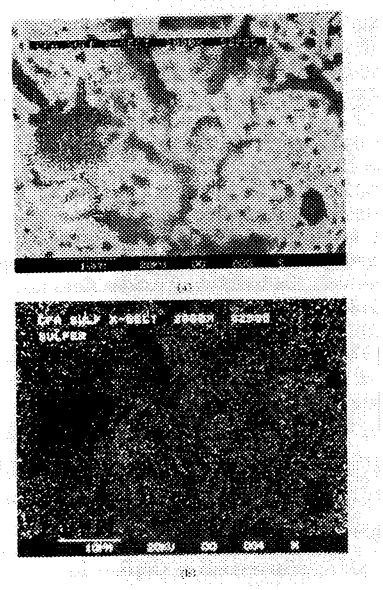

Figure 9. (a) SEM micrograph of a cross section of sulfided CFA sorbent (650 °C, 14 cycles); (b) corresponding EDS map of sulfur.

The same sulfided CFA sample was examined by SEM-EDS. The surface of the particles had a uniform distribution of Fe, and Cu, with the iron intensity stronger than that of copper and with very little sulfur or aluminum. Next, the particles were cross-sectioned and polished, and SEM-EDS maps were taken again. Figure 9 shows an SEM micrograph of the porous surface and the corresponding EDS map for sulfur, respectively. Clearly, sulfur is uniformly distributed over the entire cross-section, the only sulfur-deficient regions corresponding to large macropores. Similarly uniform distributions were obtained for copper, iron, and aluminum. These data along with the XRD analysis indicate that the most active compounds in CFA are in the underlying amorphous phase, which is comprised of alumina-bound Cu (and Fe) oxides. The iron-rich surface of the CFA particles is only partially sulfided but may assist in retaining the amorphous phase in an active and regenerable state.

Conclusions

A special technique has been employed to prepare metal oxides, such as ZnO, $ZnO–Fe_2O_3$, $CuO–Fe_2O_3$, $CuO–Al_2O_3$, and $CuO–Fe_2O_3–Al_2O_3$ as porous solids of medium surface area (10–30 m^2/g) and very high pore volume (1–2 cm^3/g). These materials have been found to exhibit improved performance for hot gas cleanup applications over conventional H_2S sorbents. This is displayed by sharp H_2S breakthrough curves, indicating rapid reaction and diffusion rates and minimal pore plugging, which all result in high absorption capacity, stability, and good regenerability of sorbents. The fresh porous sorbents yielded 100% conversion. After one or more regenerations, the conversion declined to 60–80% largely due to surface area loss. With ZnO, the prebreakthrough H_2S concentration was well below the equilibrium of bulk sulfide formation, indicating the possible effect of surface sulfide formation.

The porous zinc oxide and zinc ferrite materials were equally efficient H_2S sorbents. At and above 600 °C, however, both sorbents suffered loss of zinc by reduction and vaporization. This problem was absent in CuO-containing materials. In the sulfidation of $CuO–Fe_2O_3$, CuO–

Al_2O_3, and $CuO-Fe_2O_3-Al_2O_3$, the results suggest stepwise reduction of copper from 2+ to 1+ to 0 oxidation states. Sulfidation equilibrium is much more favorable for the oxidized than the metallic state of copper. In the temperature range 538–600 °C, the association of copper oxide with iron oxide in copper ferrite and aluminum oxide in copper aluminate stabilizes an intermediate compound of better sulfidation equilibria than Cu^0. At 650 °C, however, reduction to metallic copper is rapid, and the H_2S concentration corresponds to the sulfidation equilibrium for metallic copper. The sorbent CFA ($2CuO-Fe_2O_3-Al_2O_3$) was found to be superior to either $CuO-Fe_2O_3$ or $CuO-Al_2O_3$, yielding stable conversion and subequilibrium H_2S levels (with respect to metallic copper sulfidation) at temperatures as high as 650 °C. Several of these sorbents appear promising for high-temperature desulfurization applications, provided they can be produced as pellets of reasonable mechanical strength without compromising too much their favorable porous structure. Use of pellets would produce somewhat lower conversions than those obtained here with −20+40-mesh particles. A more detailed investigation of solid-phase transitions and reaction mechanisms will be conducted in future work to eludicate further the observed sulfidation/regeneration characteristics of these materials.

Acknowledgment

This work was carried out under a contract (DE-AI21-83MC20417) from the Department of Energy, Morgantown Energy Technology Center. The XRD and SEM/EDS analyses were performed by L. Lowry and R. Ruiz of the Jet Propulsion Laboratory. We thank Dr. G. Krishnan of SRI International for the mercury porosimetry analyses performed in his laboratory.

Registry No. ZnF, 12063-19-3; $CuFe_2O_4$, 12018-79-0; $CuFeS_2$, 12015-76-8; $CuAl_2O_4$, 12042-92-1; Fe_2O_3, 1309-37-1; Al_2O_3, 1344-28-1; ZnO, 1314-13-2; CuO, 1317-38-0; H_2S, 7783-06-4.

Literature Cited

Anderson, G. L.; Garrigan, P. C. Paper presented at the Electrochemical Society Meeting, Montreal, Quebec, Canada, May 10–12, 1982.
Barrin, I.; Knacke, O. "Thermochemical Properties of Inorganic Substances"; Springer-Verlag: New York, 1973.
Gavalas, G. R.; Phichitkul, C.; Voecks, G. E. *J. Catal.* **1984**, *88*, 54.
Giner, Inc. Final Report to Argonne National Laboratory, Contract 31-109-39-5804, Waltham, MA, 1981.
Grindley, T.; Steinfeld, G. DOE/MC/16545-1125, METC, Morgantown, WV, 1981.
Jalan, V. Final Report, DOE/MC/16021-1486, Giner, Inc., Waltham, MA, 1983.
Marcilly, C.; Courty, P.; Delmon, G. J. *Am. Ceram. Soc.* **1970**, *53* (1), 56.
MERC Hot Gas Cleanup Task Force Final Report, MERC/SP-78/2, MERC, Morgantown, WV, 1978.
Oldaker, E. C.; Poston, A. M.; Farrior, W. L. Reports MERC/TPR-75/1 and 2, MERC, Morgantown, WV, 1975.
Oldaker, E. C.; Gillmore, D. W. *Prepr., Div. Fuel Chem., Am. Chem. Soc.* **1976**, *21* (4), 79.
Rostrup-Nielsen, J. R. "Steam Reforming Catalysts"; Teknisk Forlag A/S: Copenhagen, Denmark, 1975.
Schrodt, J. T. Final Report, DOE/ET/10463-T1 (Vol. 1), University of Kentucky, Lexington, KY, 1980.
Westmoreland, P. R.; Harrison, D. P. *Environ. Sci. Technol.* **1976**, *10*, 659.
Westmoreland, P. R.; Gibson, J. B.; Harrison, D. P. *Environ. Sci. Technol.* **1977**, *11*, 488.

Received for review September 19, 1984
Revised manuscript received July 23, 1985
Accepted July 29, 1985

CHAPTER V

Tengo, vamos a ver
Tengo,
lo que tenía que tener

Nicolás Guillén

The first part of this chapter was submitted for publication to the Journal *Env. Sci. & Tech.* Interaction of H_2S in a reducing atmosphere with alumina-supported V_2O_5 is treated in detail. Following the paper, some additional results are discussed.

HYDROGEN SULFIDE REMOVAL BY SUPPORTED VANADIUM OXIDE

Miguel J. Bagajewicz, Satish S. Tamhankar[+],

Maria F. Stephanopoulos [++], George R. Gavalas*

Department of Chemical Engineering and Jet Propulsion Laboratory

California Institute of Technology

Pasadena, CA 91125

[+] *Now with The BOC Group, Technical Center, Murray Hill, NJ 07974*

[++] *Now with Dep. of Chem. Eng., MIT, Cambridge, MA 02139*

* *Author to whom correspondence should be addressed*

ABSTRACT

The retention of hydrogen sulfide by alumina-supported vanadium oxide at 650-700 ^{0}C is studied using flow reactor experiments. The effects of sorbent prereduction and gas-phase composition (H_2 and H_2O content) are discussed. It is found that hydrogen sulfide is chemisorbed reversibly on a nonstoichiometric vanadium oxide. Bulk sulfide is not formed.

Introduction

In efforts to develop a process for the removal of H_2S from coal-derived fuel gas at high temperatures (500-800°C), various transition metal oxides have been considered as potential sorbents. Comparative evaluation of various oxide sorbents have been published in Department of Energy reports (MERC [1]) and in journals (Westmoreland and Harrison [3]; Westmoreland *et al.* [4]).

In a fuel gas atmosphere most metal oxides are first reduced to lower oxides or even metals that in turn react with H_2S. Thus, in general, the reactions can be represented as

$$MO_x \xrightarrow{H_2,CO} MO_y \qquad (y < x) \tag{1}$$

$$MO_y + y\,H_2S \rightleftharpoons MS_y + y\,H_2O \tag{2}$$

The level of H_2S in the purified gas and the sulfur loading of the sorbent at H_2S breakthrough are governed by the kinetic as well as by the thermodynamic parameters of these reactions.

In the case of V_2O_5, thermodynamic data (JANAF tables [6]) predict reduction to V_2O_3, which has been considered to react according to

$$V_2O_3 + 3\,H_2S \longrightarrow V_2S_3 + 3H_2O \tag{3}$$

This reaction was regarded as thermodynamically favorable (MERC [1], Jalan *et al.* [2]) in the temperature range of interest resulting in equilibrium H_2S levels of less than 10 parts per million (ppm). In view of the presumed favorable thermodynamics of reaction (3), V_2O_5 appeared to be a very promising sorbent. However, Westmoreland *et al.* [4] found that reaction (3) was much slower compared to sulfidation reactions of other metal oxides. Jalan *et al.* [2] experimented with V_2O_5 supported on high surface area materials (alumina, zeolites) in the hope of improving the kinetics of reaction (3). But they consistently found sulfur capture capacities much lower than expected from the stoichiometry of reaction (3).

In the studies mentioned above the free energy of reaction (3) was calculated using the thermodynamic data for V_2S_3 published in a NBS report [7] and other conventional sources. However, Mills [8] found these data to be in great error. The revised values of the heat of formation and the free energy of formation for V_2S_3 estimated by Mills [8] imply that reaction (3) has unfavorable equilibrium under conditions of practical interest.

In apparent contradiction with the unfavorable equilibrium suggested by the recent data, Jalan *et al.* [2] consistently observed a finite H_2S uptake by various vanadium oxide sorbents. To explain this finding, Jalan *et al.* [9] postulated formation of a surface complex, $V(HS)_3$, which, however, was not substantiated by direct means. In the present study, simple packed-bed flow experiments were used to show that at 650-700°C, H_2S is strongly but reversibly adsorbed on a nonstoichiometric reduced form of vanadium oxide, which is being formed ahead of the sulfidation front or during a separate prereduction step. A similar study on adsorption of H_2S on $MoO_3 - TiO_2$ was reported by Matsuda *et al.* [10].

Experimental

Sorbent Preparation : A high surface area alumina ($\gamma - Al_2O_3$) support in the form of 1/8" pellets was obtained from United Catalsts Inc. (UCI). The pellets were crushed, and a -35+45 mesh size fraction was collected. The alumina was thermally stabilized by heating in air at 800°C for 2-5 hr. With this thermal treatment, the original surface area of 100 m^2/g was reduced to 85 m^2/g. After cooling, the alumina was washed a few times in concentrated NH_4OH to remove fines and then dried slowly to 200°C. After this treatment the surface area remained unchanged.

The stabilized alumina was impregnated with a solution of ammonium metavanadate in concentrated NH_4OH. The impregnated particles were quickly washed, slowly dried and then calcined at 350°C to obtain V_2O_5 supported on alumina (V_2O_5/Al_2O3). The sorbent properties are listed in Table 1.

Since the present experiments were conducted in a reducing atmosphere, resembling that of fuel gas, a preliminary study of the reducibility of the sorbent in the presence of H_2 was performed. A small sample of NV1 was heated in a thermogravimetric analyzer, and when the temperature reached 700 °C, a flow of 9% of H_2 in N_2 was introduced. A rapid weight loss occurred within the first minute, approximately equivalent to the removal of one atom of oxygen from each V_2O_5 molecule. The weight continued to decrease slowly, and after 10 min. the equivalent of an additional 0.25 atom of oxygen was removed. At this point the rate of weight loss had declined to an almost undetectable level, in the time range of the experiment. Based on these results it is assumed that a non-stoichiometric vanadium oxide of approximate composition $V_2O_{3.75}$ is acting as a substrate for H_2S chemisorption.

Apparatus and Procedure : The experiments were performed with a reactor consisting of a quartz tube, 1 cm I.D. and 41 cm length, mounted vertically inside an electric furnace and instrumented with a K-type thermocouple moving inside a quartz thermowell (0.3 cm I.D.) concentric to the reactor, as described elsewhere (Tamhankar *et al*, [5]). Different gases from cylinders passed through calibrated flowmeters into a common gas line leading to the reactor. The gas mixture could be flown through the reactor in the upward or downward direction, as desired. The lines leading to the reactor were heated and insulated. Nitrogen bubbling through water maintained at a constant temperature in a 3-neck flask assembly was used to introduce known amounts of water vapor into the feed gas stream. Temperatures at various locations in the system were monitored by K-type thermocouples connected to a multichannel digital readout. In all experiments the reactor pressure was slightly above atmospheric.

The experiments generally consisted of adsorption, desorption, and regeneration periods, carried out at the same temperature in the range 500-700°C. Typically, 3-6 g of sorbent were loaded into the reactor, which was brought to the desired temperature under flow of nitrogen. In adsorption runs the feed gas contained H_2 (0-20%), H_2S (150-2000 ppm) and N_2 (balance). Desorption was carried out by a N_2 purge, while regeneration was carried out with a N_2-air mixture (O_2: 1-5%).

The product gas was passed through ice traps to condense any elemental sulfur formed and was analyzed for H_2S and SO_2 by a gas chromatograph equipped with a flame photometric detector. The column was teflon tubing 6 ft long and 1/8" O.D. packed with Chromosil 310 (Supelco Inc.) and was operated isothermally at 50°C. By using an automated valve, system samples could be analyzed every 2-3 minutes to provide time-resolved composition. The tubing

downstream of the reactor consisted of teflon-coated stainless steel to avoid H_2S adsorption. An absorber loop containing iodine solution in the exit line from the gas-sampling valve was used to analyze total sulfur gases (H_2S, SO_2) eluted from the bed or produced during any period. The amount of sulfur gases absorbed was determined by titrating the excess iodine with a solution of sodium thiosulfate. Elemental sulfur collected in the traps was dissolved in a solution of sodium sulfite and analyzed by a standard iodometric titration method.

Results and Discussion

The first set of experiments carried out at 700^0C with sorbent NV1 included a sequence of six adsorption periods C1-C6 with N_2 purge and/or regeneration by air between succesive adsorptions. The results are presented in Figure 1 in the form of plots of outlet H_2S concentration versus time. In the first two adsorption periods C1 and C2, the breakthrough of H_2S takes place at about six minutes. Beyond the breakthrough H_2S continued to be partially retained in the bed as indicated by the slow rise in H_2S concentration. Similar sulfidation runs shown in Figure 2 were conducted using sorbent NV2.

A nitrogen purge followed cycles C1, C2 and C3 of sorbent NV1, as well as all cycles done with sorbent NV2. During those purging periods, H_2S and elemental sulfur were detected at the bed outlet. The amount of H_2S collected in the iodine absorbers, together with the sulfur captured in the trap, was equivalent, within experimental error, to the amount of H_2S retained in the bed during the sulfidation step. The amount of H_2S retained per mol of V_2O_5 originally present varies from cycle to cycle, especially because complete saturation of the bed was not achieved. Values as high as 0.42 mol H_2S/mol V_2O_5 were observed.

After each nitrogen purge, the sorbent was regenerated by a flow of a

nitrogen- air mixture, except after cycles C2 and C3 of sorbent NV2, where this step was omitted. In all cases only traces of SO_2 were detected during this period. This provides clear evidence that no bulk sulfide was being formed, and that H_2S was chemisorbed reversibly.

In the set of experiments with sorbent NV2, five consecutive cycles of adsorption- desorption were carried out. The adsorption breakthrough curves are shown in Figure 2. Two parameters, viz. pre-treatment with a nitrogen-hydrogen mixture and temperature, were changed in the adsorption cycles. The effects of these changes on the adsorption breakthrough curves were not too significant, and the total amount of H_2S retained at the end of each cycle did not vary greatly. However, some subtle differences are apparent. Thus, in the first cycle, since the reduced form of V_2O_5 was not present from the beginning, but was formed *in situ*, an early breakthrough is seen. Following adsorption periods C1,C2 and C3 the bed was not regenerated but simply purged with nitrogen. With the bed pre-reduced, the breakthrough time in C2 and C3 is somewhat larger than in C1. The amount retained in period C4 at 700°C was somewhat lower than in C2 and C3 perhaps because of less favorable equilibrium at 700°C compared to 650°C and the possible loss of surface area in repeated high-temperature operation without regeneration. On regeneration V_2O_5 is re-formed at 700°C, and consequently, the adsorption performance in cycle C5 is substantially better than in cycle C4.

To study the contribution of alumina to the sorbent adsorption capacity a separate run was performed. Two grams of UCI-Alumina were placed inside the reactor and a sulfidation run was performed at 700°C, using a 20% H_2 concentration and 5000 ppm of H_2S. The amount retained was $8. \times 10^{-8}$ mol/ m^2 compared with values of 10^{-6} mol/m^2 obtained with the vanadium containing

sorbents. The adsorbtive contribution of alumina in vanadium containing sorbents would be even smaller, in view of the blocking effect of the vanadium oxide at the values of loading employed.

During the nitrogen purge following various sulfidations, as much as 26% of the total H_2S retained in the bed desorbed as elemental sulfur and was collected at the bed outlet. Since H_2 is not present in the purging gas, decomposition of H_2S takes place and, as reported by Fukuda *et al.* [11], is catalyzed by the solid substrate. The amount of elemental sulfur collected was lower than the equilibrium amount corresponding to the measured H_2S concentration at the reactor outlet.

The above results can be described by the following reaction sequence:

$$\text{reduction}: \quad V_2O_5 + (5-y)\,H_2 \; - - > \; V_2O_y + (5-y)\,H_2O \tag{4}$$

$$\text{adsorption}: \quad V_2O_y + H_2S \; - - > \; V_2O_y.H_2S \tag{5}$$

$$\text{desorption}: \quad V_2O_y.H_2S \; - - > \; V_2O_y + (1-z)\,H_2S + z\,H_2 + \frac{z}{2}\,S_2 \tag{6}$$

$$\text{regeneration}: \quad V_2O_y + \left(\frac{5-y}{2}\right) \; - - > \; V_2O_5 \tag{7}$$

An additional reaction that is important in the absence of H_2 from the input gas is the direct reduction of V_2O_5 by H_2S:

$$V_2O_5 + \frac{(5-y)}{2}\,H_2S \; - - > \; V_2O_y + \frac{(5-y)}{2}\,SO_2 + \frac{(5-y)}{2}\,H_2 \tag{8}$$

In the presence of H_2, reaction (8) is ineffective since V_2O_5 is reduced ahead of the sulfidation front. Nevertheless, at the beginning of sulfidation of fresh or regenerated sorbents, SO_2 in amounts 1 to 5 ppm levels was observed. These small peaks of SO_2, which are not shown in the figures, fade away as sulfidation

proceeds, evidently due to the conversion of V_2O_5 to a lower oxide by reduction with H_2. When sulfidation was carried out in the absence of H_2, as in period C6 (Figure 1), H_2S consumption was much higher and SO_2 was formed in larger amounts. The constant level of SO_2 observed before breakthrough is an indication that reduction of V_2O_5 is performed by means of reaction (8).

An important aspect in relation to the desulfurization of a coal-derived fuel gas is the effect of H_2O on the interaction of H_2S with V_2O_5 or the reduced vanadium oxides present. In sulfidation period C3 in the above batch of experiments, 7 mol% H_2O was added to the reaction gas. The resulting H_2S retention was found to be much lower (Figure 1) and the breakthrough sharper, suggesting that H_2O and H_2S compete for the same adsorption sites.

The tables and figures referred to in the above paper can be found at the end of the chapter.

THE DESORPTION PROCESS

Notable results were obtained during H_2S desorption in the cycles corresponding to the sulfidation of NV2, as shown in Figure 3. In all curves, following the initial decay, a plateau region is apparent, suggesting an equilibrium behavior. Competitive chemisorption of hydrogen is believed to be responsible for the initial behavior. The effect of the flow rate of purging nitrogen on these curves is the most interesting result of this batch of experiments.

A new set of experiments referred to later as the "Sample 2" was performed to further clarify the above findings, resulting in additional details not previously observed. In Figure 4, breakthrough curves of 5 sulfidation cycles using NV2 are shown. Regeneration was conducted after each cycle, without any pretreatment. The first three cycles(c-1,c-3 and c-4) were performed at exactly the same conditions as in the batch of experiments shown in Figure 2. Note that the breakthrough times are comparable. However, a new detail not detected before is apparent : in cycle c-4 there is a relative maximum in the first few minutes of the run. Cycles c-5 and c-6 were performed using much lower H_2S inlet concentration (490 ppm), with the same H_2 concentration. In cycle c-6 the first relative maximum is again detected. Pure alumina presents the same response upon exposure to H_2S as shown in Figure 5. Competitive adsorption of two species is known to show the type of maxima [12].

Figure 5 shows the desorption pattern for the second batch of experiments with NV2 (Sample 2). Three striking results are inmediatly recognized. First, the plateau regions of of cycles c-1 and c-6, which employed different H_2S inlet concentrations, almost coincide. One would expect c-1 to have the same short plateau of $\approx$ 400 ppm as in the case of cycle c-1 of Figure 4. Second, relative

minima, ocurring before the plateau develops, are observed in the case of cycles c-1 and c-6. No explanation has been found for this behavior. Finally, in the desorption of cycle c-5 a relative maximum higher than the initial concentration is seen. This response cannot be explained on the basis of competitive chemisorption alone. Using a model with first order kinetics, Thomas [13] was able to show that this maximum can occur if the adsorption step was interrupted at some stage, as it was in our case where the process was not conducted until complete bed saturation. More detailed experiments are needed to understand this unusual phenomenon. In the appendix at the end of this chapter, a theoretical analysis of some aspects of the desorption results is done.

CONCLUSIONS

The interaction of V_2O_5 supported on alumina was studied in detail and no bulk sulfide formation was observed, contrary to earlier expectations. The V_2O_5 is first reduced to a lower oxidation state very fast, so that competitive chemisorption of H_2 and H_2S takes place on the reduced form. The outlet concentrations during desorption show the typical plateau obtained when competitive adsorption is analyzed in the case of fast kinetics for both components (equilibrium). However, the flow rate dependence of the plateau concentration that is observed experimentally is not predicted by this model. Further modeling of the problem is possible, but until more experimentation is done to clarify some basic issues, theoretical treatments lead to more questions rather than to answers. Some interesting phenomena, such as the relative maxima observed in sulfidation breakthrough curves as well as maxima and minima arising during desorption, indicate that the system warrants further experimental and theoretical study.

REFERENCES

1.- MERC Hot Gas Cleanup Task Force. *MERC/SP-78/2.* 1978.

2.- Jalan V. ; Desai M. ; Frost D.; Wu D. *Final Report to DOE. Contract No. 31-109-38-5804. Giner Inc., Waltham, Massachusetts,* 1981.

3.- Westmoreland P.R. and Harrison D.P. *Environm. Sci. Technol.*, 1976, **10**, 659.

4.- Westmoreland P.R.; Gibson J.B. and Harrison D.P. *Environm. Sci. Technol.*, 1977, **11**, 488.

5.- Tamhankar S.S.; Bagajewicz M.J. and Gavalas G.R. (California Institute of Technology) and Sharma P.K. and Flytzani-Stephanopoulos M. (JPL). *I&EC, Proc. Des. and Dev.*, 1986, **25**, 429.

6.- Stull D.R.; Prophet H. *Editors*, JANAF Thermochemical Tables. NSRDS-NBS 37, U.S Government Printing Office, Washington DC, 1971 Supplement: *J. Phys. Chem. Ref. Data*, 1974, **4**, 1.

7.- *NBS. Technical Note 270-5.* 1971.

8.- Mills K. C. *Thermodynamic Data for Inorganic Sulfides, Selenides and Tellurides. Butterworth, London,Eng.*, 1974.

9.- Jalan V.; Desai M.; Brooks C. and Waterhouse R. *Proceedings of the Third Annual DOE Contractors' Meeting on "Contaminant Control in Hot Coal Derived Gas Streams", DE64000216, DOE/METC, Morgantown*, 1983.

10.- Matsuda S.; Kamo T.; Imahashi J. and Nakajima F. *I&EC Fund.*, 1982, **21**, 18.

11.- Fukuda K.; Dokiya M.; Kameyama T. and Kotera Y. *I&EC Fund.*, 1978, **17**, 4.

12.- M. Morbidelli G. Strort, S. Carra, G. Niederjaufner, A. Pontoglio, *Chem. Engng Sci.*, 1984, **39**, 3.

13.- H.C. Thomas, *Annals of the New York Academy of Sciences*, 1948, **49**, 161.

14.- R. Aris and N.R. Amundson, *Mathem. Methods in Chem. Eng., Vol 2.*Prentice Hall. New York, 1975.

Table 1. Properties of Supported Vanadium Oxides

Property	*UCI – Alumina*	*NV1*	*NV2*
Source	UnitedCatalysts T – 2432	UCI – Alumina impregnation	UCI – Alumina impregnation
Bulk Density	40	– –	– –
Particle Size	−35 + 45 mesh	−35 + 45 mesh	−35 + 45 mesh
Surface Area (m^2/g)	85(*)	93	93
Pore Volume (cm^3/g)	0.6 – 0.7(**)	– –	– –
Vanadium $(wt\%)$	– –	2.24	1.88

(*) After stabilization process.

(**) Manufacturer data.

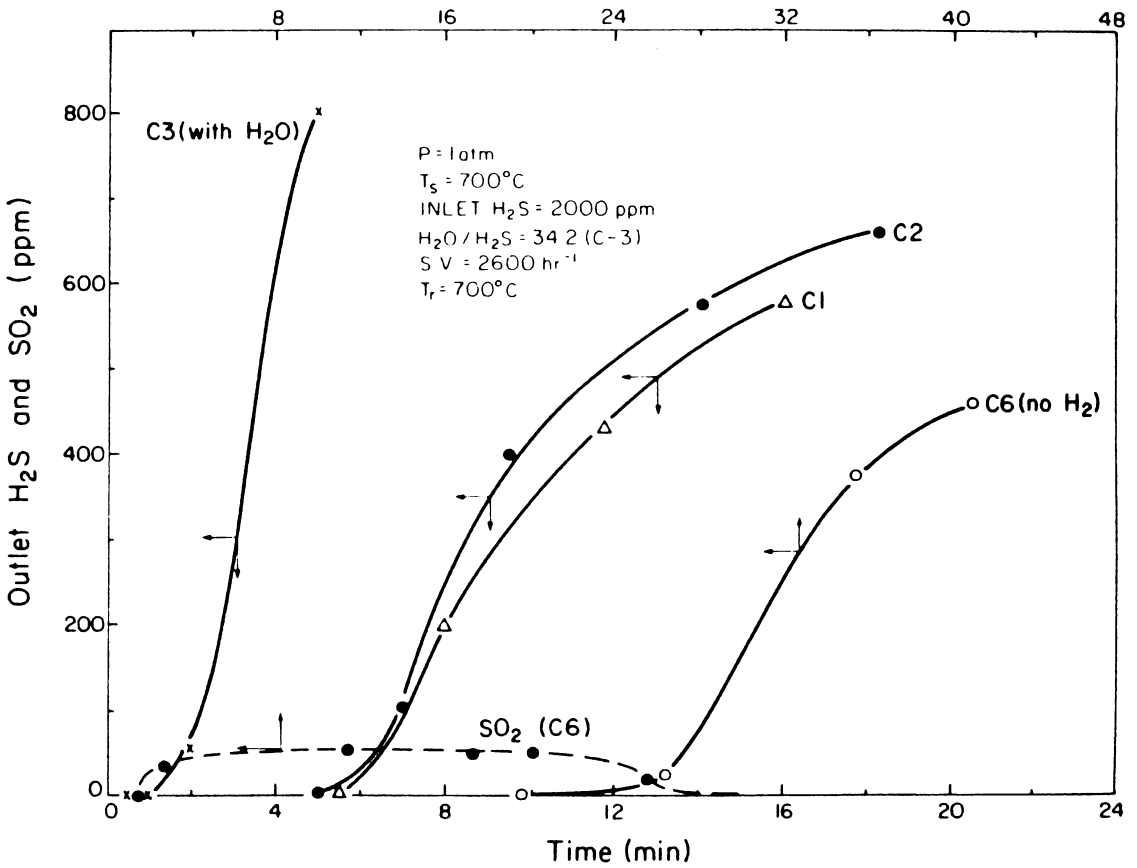

Figure 1.- Breakthrough Curves in Succesive Sulfidation Cycles of NV1 Sorbent.

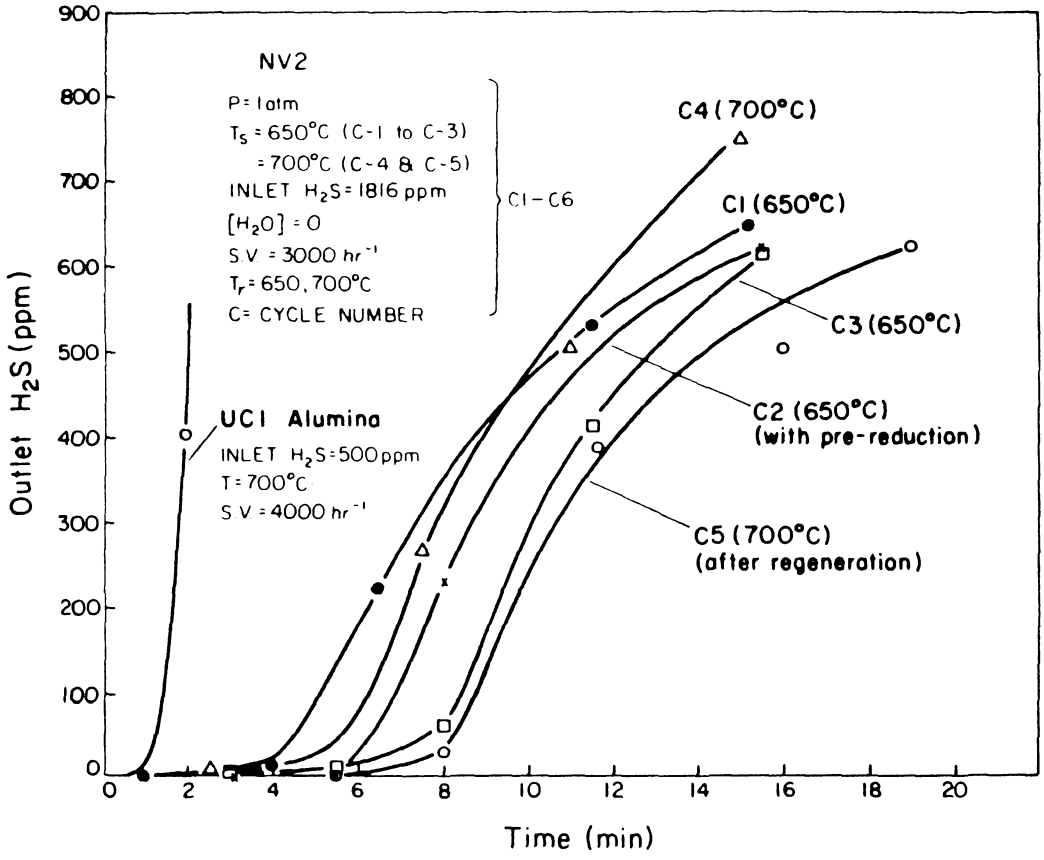

Figure 2.- Breakthrough Curves in Succesive Sulfidation Cycles of NV2 Sorbent and UCI-Alumina (Sample 1).

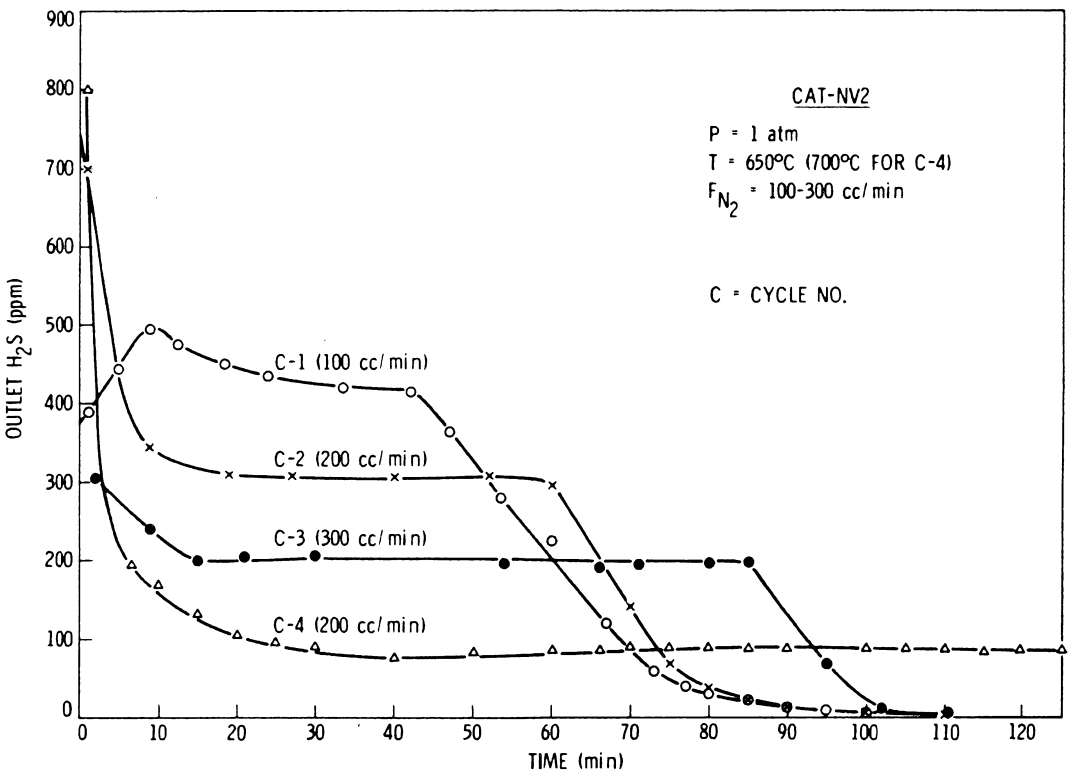

Figure 3.- H_2S Desorption from Sulfided NV2 (Sample 1).

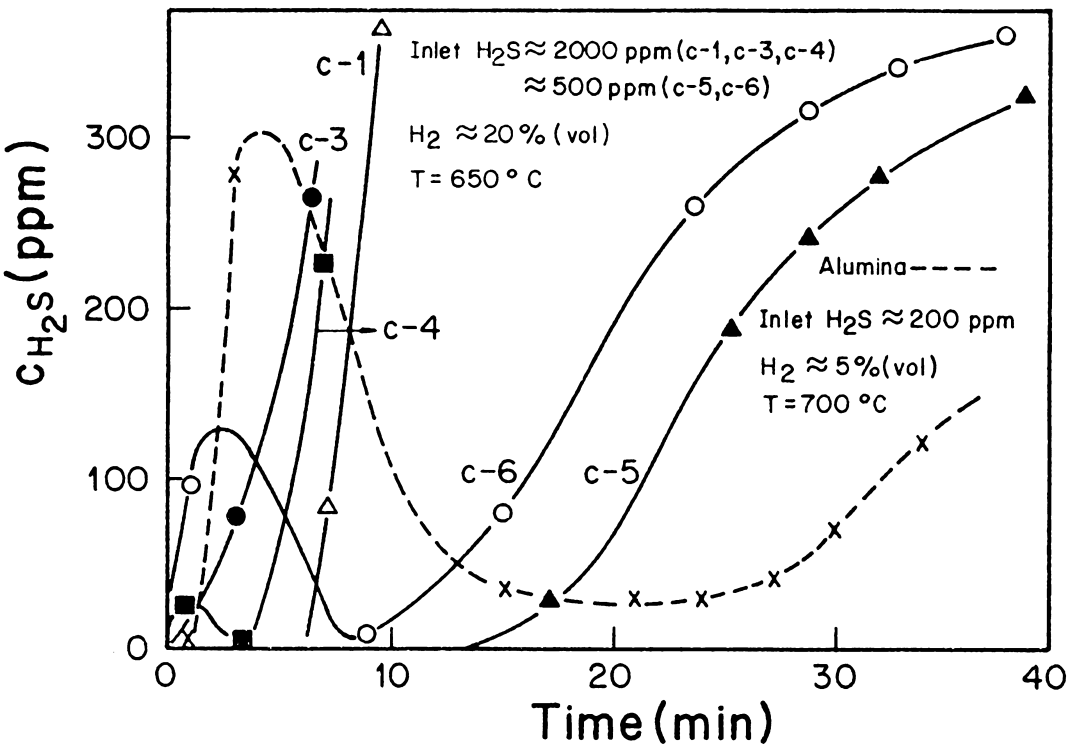

Figure 4: Breakthrough Curves in Successive Sulfidation Cycles of NV2 Sorbent and UCI-Alumina (Sample 2).

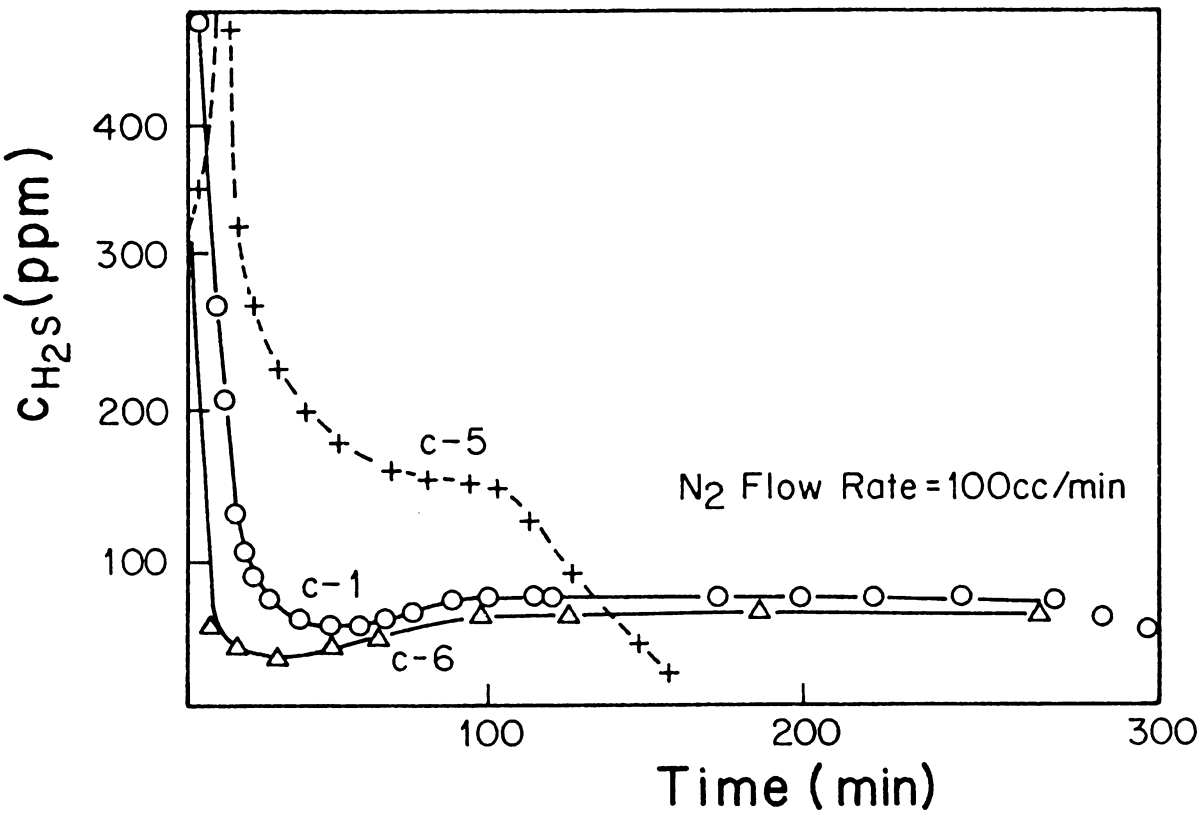

Figure 5: H_2S Desorption from Sulfided NV2 (Sample 2).

APPENDIX

In this appendix some results obtained in the desorption process are discussed using theoretical results. At the end of the sulfidation cycle, only H_2S and H_2 are chemisorbed on the sorbent. While the chemisorption of H_2 at high temperatures has been studied for many metals and oxides, no data are available for the case of vanadium oxides. Likewise, no information is available about the chemisorption of H_2S on vanadium oxides.

Constant concentration levels during desorption from a fixed bed is a well characterized phenomenon corresponding to equilibrium between chemisorbed and gaseous species. Therefore, the presence of the plateau in the desorption curve suggests that H_2S is at equilibrium. For the purpose of the following analysis, it will be assumed that H_2 was also at equilibrium, although the concentration of this gas was not measured to test this assumption.

The continuity and equilibrium equations for chemisorption are

$$\frac{\partial c_i}{\partial t} + u\,\frac{\partial c_i}{\partial z} + \frac{(1-\varepsilon)}{\varepsilon}\,\frac{\partial n_i}{\partial t} = 0 \qquad i = A, B \tag{1}$$

$$n_A = \frac{K_A c_A\,(n - n_B)}{1 + K_A c_A} \tag{2}$$

$$n_B = \frac{K_B c_B\,(n - n_A)}{1 + K_B c_B} \tag{3}$$

where: c_A and c_B are the gas phase concentrations of H_2S and H_2, respectively; n_A and n_B are the concentrations of adsorbed H_2S and H_2; n is the total concentration of chemisorbed sites ; ε is the void fraction; u is the linear gas phase velocity; K_A and K_B are equilibrium constants.

The following assumptions were made

(i) Langmuir-type equilibrium relationships for both components were assumed.

(ii) Only one type of chemisorption sites is available.

(iii) H_2 is considered to be less strongly chemisorbed than H_2S. Therefore, $K_A > K_B$.

(iv) The velocity u is considered constant.

It is believed that in spite of these simplifications the qualitative behavior of the system will be reproduced. Following Aris and Amundson [14], after nondimensionalizing the system of two equations that remains when equilibrium relationships (2) and (3) are substituted in equations (1), the hodograph transformation was applied. This yielded analytical solutions to the elution problem. A general sketch of the solution obtained is drawn below:

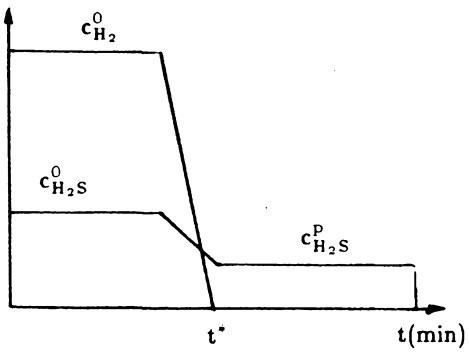

Soon after the less strongly adsorbed H_2 leaves the bed, a plateau starts to develop for the strongly adsorbed H_2S. With minor differences, this solution exhibits the same pattern as our observed desorption curves. From the mathematical description of the solution [14] we reproduce the formula for the level of the H_2S plateau concentration $c^P_{H_2S}$

$$c^P_{H_2S} = c^o_{H_2S} - \frac{\Lambda\, c^o_{H_2}}{\sigma_+} \tag{4}$$

where: $\Lambda = K_B/K_A$ and σ_+ is the positive root of the following equation

$$\sigma^2 + \left[\frac{\Lambda(1 + K_A c^o_A) - (1 + K_B c^o_B)}{K_A c_A}\right]\sigma - \Lambda^2 \frac{c^o_B}{c^o_A} = 0 \tag{5}$$

One estimate of the maximum concentration n can be obtained if a monolayer of H_2S is assumed. A material balance for H_2S provides an estimate for n^0_A. Similarly, by assuming that hydrogen evolves as shown above, an estimate for n^0_B can be obtained using the following material balance: $n^0_{H_2} = c^0_{H_2}(F/V)t^*$, where F is the flow rate of inert used at the reactor inlet, V is the total sorbent volume and t^* is the time at which the plateau starts.

The above results were used to estimate K_A and K_B by solving Equations (2) and (3), obtaining $K_A = 7.5\ m^3/mol$ and $K_B = 0.375\ m^3/mol$. Using these values to solve (5) for σ_+, and substituting in (4) a plateau concentration of about $\approx$ 360 ppm is obtained for cycle c-1 of Figure 4, in close agreement with the experimental value. The model predicts a plateau concentration that is independent of the N_2 flow rate. The different values measured at different flow rates of nitrogen (Figure 4), seem to indicate a flow rate dependency. However, comparison between cycles c-5 and c-6, which were conducted at the same flow rate (Figure 5), also shows some difference indicating that, aside from the flow rate, other parameters have influence on the system. This is analyzed next.

It may be useful to use the above analysis to calculate the following sensitivity parameters:

$$\left.\begin{aligned} \frac{\partial c^{p}_{H_2S}}{\partial c^{o}_{H_2S}} &\approx 1.8 \\ \frac{\partial c^{p}_{H_2S}}{\partial K_{H_2S}} &\approx -0.009 \\ \frac{\partial c^{p}_{H_2S}}{\partial c^{o}_{H_2}} &\approx -0.0016 \\ \frac{\partial c^{p}_{H_2S}}{\partial K_{H_2}} &\approx -0.21 \end{aligned}\right\} \qquad (6)$$

The following are the expected changes in plateau concentration for the indicated changes in the corresponding parameters:

$$\left.\begin{aligned} \Delta c^{p}_{H_2S} &\approx \pm 90 \text{ ppm} & \Delta c^{o}_{H_2S} &= \pm 5\% \\ \Delta c^{p}_{H_2S} &\approx -120 \text{ ppm} & \Delta K_{H_2S} &= 10\% \\ \Delta c^{p}_{H_2S} &\approx \pm 130 \text{ ppm} & \Delta c^{o}_{H_2} &= \pm 5\% \\ \Delta c^{p}_{H_2S} &\approx -150 \text{ ppm} & \Delta K_{H_2} &= 10\% \end{aligned}\right\} \qquad (7)$$

As was reported before, the reduction of the vanadium oxide is a slow process, and therefore continues to take place during the time span of all the succesive cycles, until regeneration of V_2O_5 is performed. Consequently, the properties of the chemisorption sites may be changing along this period, influencing directly the values of the equilibrium constants. Since the plateau concentrations keep decreasing for successive cycles corresponding to an increase of the values of K_{H_2S} and K_{H_2}, a definite direction of change is obtained, contrasting with the random variations that normally arise in experimental measurements. This has to be substantiated with more experiments.

CHAPTER VI

Y como muchacho loco
Lo pasaba de holgazán
Con razón dice el refrán
Que lo bueno dura poco.

del Martín Fierro

THE REGENERATION OF ZnS

In Chapters III and IV, results on the desulfurization properties of ZnO, were presented. High surface area bulk ZnO proved to be more efficient than alumina-supported ZnO. Since the regeneration step converts the sulfide back to the oxide, the way in which this step is conducted affects the performance of the overall process. This chapter covers some of our work on the regeneration of bulk ZnS.

The following is an outline of the different topics covered in this chapter. First, a thermodynamic analysis is presented identifying all the possible species and reactions present in the ZnS oxidation process. Then, background material on the kinetics is presented. A brief description of preparation and properties of the sorbent used in our experiments is given, followed by our experimental results

on the kinetics of oxidation. To conclude, the secondary reactions encountered in the regeneration carried out in a fixed-bed reactor are briefly analyzed, and some experimental results are presented.

BACKGROUND MATERIAL AND PRELIMINARY ANALYSIS

In this section the thermodynamics, mechanism and kinetics of ZnS oxidation are briefly reviewed. The roasting of ZnS is an old process in the pyrometallurgy of sulfide ores. Pertinent thermodynamic data are available [1-4] and can be conveniently presented in the diagram of Figure 1. In this figure, phase equilibrium is shown as a function of the partial pressure of two components in the gas phase. Each phase is stable within a predominance region, bordered by lines that represent the coexistence with other phases. The slope of each line is given by the stoichiometry of the corresponding reaction. With the use of such a diagram the identification of the stable solid phase is immediate, once the composition of the gas phase is known. The advantage of using this diagram, contrasting with reaction network analysis, is transparent.

The first thing to point out in the $Zn - O_2 - SO_2$ diagram is the presence of an intermediate oxysulfate, namely, $2ZnSO_4.ZnO$, as a stable and separate phase. At low SO_2 concentrations and in the presence of oxygen concentrations normally used in oxidation, ZnO is the stable solid species.

The mechanism of oxidation has been a matter of some speculation. The formation of oxide is generally attributed to the direct reaction

$$ZnS + \frac{3}{2}O_2 \; - - > \; ZnO + SO_2 \qquad (1)$$

The mechanism of formation of the experimentally observed $ZnSO_4$ is less cer-

tain. One possibility is formation *via* the oxide intermediate:

$$ZnO + SO_2 + \frac{1}{2} O_2 \text{ - - > } ZnSO_4 \qquad (2)$$

The other is the direct oxidation:

$$ZnS + 2\,O_2 \text{ - - > } ZnSO_4 \qquad (3)$$

Any sulfate formed would decompose when the product $P_{SO_2} P_{O_2}^{1/2}$ drops below its equilibrium value for reaction (2). The formation of the oxysulfate $2ZnSO_4.ZnO$ as an intermediate, or side product, is subject to the same uncertainities. These possible oxidation pathways are represented in a reaction network shown in Figure 2.

As was explained in Chapter II, when the sulfate (or oxysulfate) is first formed *via* reaction (3), three regions can appear in the reactor. A region of unreacted ZnS is followed by a front where reaction (3) is occurring. Thus, a second region of sulfate follows and its decomposition takes place in a second reaction front. This leaves the final product ZnO as the last region in the reactor.

If ZnO is directly formed *via* reaction (1), only one front would be observed inside the reactor. Since in this case reaction (3) does not take place, sulfate (or oxysulfate) formation can occur only *via* reaction (2). Therefore, the condition $P_{SO_2} P_{O_2}^{\frac{1}{2}} \geq \exp(-\Delta G_3^0/RT)$ will have to be met at some point, to obtain some sulfate formation. If the material balance of the fixed-bed reactor is used, the following expression is obtained:

$$P_{SO_2} \leq \frac{2}{3}\left(P_{O_2}^0 - P_{O_2}\right) \qquad (4)$$

where $P_{O_2}^0$ is the oxygen partial pressure at the reactor inlet. The equality is valid for the case where no reaction other than the direct oxidation (1) takes

place. This condition, which is independent of the reaction rate, is represented by the curve on top of stability diagrams for different temperatures (Figure 3). If side reactions that consume O_2 and SO_2 are present, the curve will fall inside the shaded region. The reaction path terminates at the line separating the ZnO and ZnS regions, where equilibrium of reaction (1) is eventually achieved. The reaction path also depends on $P^0_{O_2}$, and if this pressure is sufficiently low, sulfate formation is not possible.

Therefore, if sulfate formation is to be entirely avoided, the shaded region should lie completely inside the ZnO region of the stability diagram. For a given initial oxygen partial pressure, this happens above a given value of temperature. However, high temperatures have the possible pitfall of sorbent sintering and loss of surface area. Conversely, for a given operating temperature, lowering the oxygen concentration, or rapid removal of the SO_2 formed, also avoid sulfate formation. Low temperatures will reduce the rate of regeneration, while low-oxygen concentrations will produce low exit SO_2 concentration increasing the cost of final sulfur recovery or disposal. Some theoretical insights on this problem are explored in Chapter IX.

Even when the reaction path partially overlaps with the region of sulfate stability, the amount of sulfate formed can be small and tolerable. The rate of formation of sulfate according to reaction (2) is expected to be low, because it involves crystallographic transformation from the hexagonal form of ZnO to the rhombic sulfate, and because of slow product layer diffusion. Since ZnS is also hexagonal, reaction (3) is expected to be much slower than reaction (1). As will be proved later in this chapter, the oxidation of ZnS undergoes the direct route from sulfide to oxide, confirming the above qualitative considerations.

Proceeding now to reaction kinetics, we note that considerable uncertainty

exists about the order and rate constant of reaction (1). A recent paper by G. M. Prabhu *et al.* [5] presents a review and provides some new data on the kinetics of this reaction. They measured initial reaction rates with a thermogravimetric analyzer, using cylindrical pellets of various sizes and porosities. Their data were fitted with a first order reaction. This agrees with the earlier results reviewed in their paper. Other authors, including Cannon and Denbigh [6], reported that the reaction order was of order one-half. Ong *et al.* [7] concluded that reaction of adsorbed oxygen with the solid is the rate-limiting step, with the overall rate being represented by a Langmuir type expression

$$r = k_1 \frac{K_1 C_{O_2}}{1 + K_1 C_{O_2}} \tag{5}$$

where K_1 is the equilibrium constant for the adsorption process, k_1 is the kinetic constant and C_{O_2} is the oxygen concentration. This last expression fits all the experimental data here presented.

The value of the activation energy of this reaction is also a matter of disagreement. As reviewed elsewhere [5,8] no less than 14 values have been reported varying from 7.6 to 85 Kcal/mol. Our results fitted by the Langmuir expression above yielded an activation energy of the order of 66 Kcal/mol based on the temperature dependence of the rate constant k_1.

EXPERIMENTAL

Material Preparation

High surface area bulk ZnO preparation was described in Chapter IV, and essentially follows the procedure suggested in the literature [9]. Briefly, this method consists of a rapid dehydration at 70^0C of an aqueous solution of Zn

nitrate and a polyfunctional acid with at least one hydroxy and one carboxylic function (citric acid was used in our preparation) to obtain a highly porous foam. This foam was then calcined in air at 550 °C. Since the maximum temperature of the experiments was 700 °C, the sorbent was pretreated by heating for a few hours at 720 °C until the surface area was stabilized. This was achieved in approximately two hours, during which the surface area dropped from 6.5 m^2/g to 4.1 m^2/g, as measured by the BET method.

Next, the ZnO was placed in the fixed-bed reactor described in Chapter III, and sulfidation was performed at 550 ^{0}C using a stream of 0.17% H_2 and 4.16 % of H_2S. The ZnS thus obtained was analyzed using wet methods and was found to contain only 0.1 % of ZnO. Given the experimental errors of these techniques complete conversion can be assumed. The surface area of the sulfide measured using the BET method gave a value of 3.0 m^2/g.

Apparatus and Procedure

The sulfidation experiments were performed using a 2000 Cahn Thermogravimetric Balance. Figure 4 shows the essential parts of the setup. A quartz pan is suspended inside a concentric glass tube, which is sorrounded by the furnace. A thermocouple measures the temperature and a controller provides 1^0C of maximum deviation from the set value. A continuous nitrogen purge is passed through the balance mechanism for protection from corrosive sulfur gases. When the temperature reaches the desired value, a side stream coming from a mixing fitting is allowed into the thermobalance. The flows of air and nitrogen in the side stream are adjusted to achieve the desired oxygen concentration. Simultaneously, the weight is monitored as a function of time, using a chart recorder.

RESULTS AND DISCUSSION

Conversion was defined as follows:

$$\alpha_1 = \frac{W_i - W}{W_i - W_f^I} \tag{6}$$

where W is weight, W_i is initial weight and W_f^I is the weight at complete conversion, assuming that the initial sample consists entirely of ZnS and reacts completely to ZnO. Corrections due to flow rate effect on weight were taken into account.

When plotting the reaction rate, diagrams like the one shown in Figure 5 were obtained. The reaction rate grows with conversion, passing through a maximum value. Upon sulfidation of ZnO, a reduction of surface area takes place because of the higher molar volume of ZnS; therefore, as the oxidation reaction proceeds, the interfacial area between sulfide and oxide will grow, explaining the initial increase in the reaction rate.

With the chosen values of the flow rates and the geometry of the thermobalance, the oxygen concentration takes 0.5-1.0 min to reach the desired value around the sample, and hence the initial values of weight loss rates were not considered good measures of the reaction rate. Instead, to correlate the reaction rate with oxygen concentration, the maximum rates were used. These values are shown in Table 1.

The dependence of the rate on oxygen concentration was found to follow the expression given in Equation (5), as can be inferred by the good fit obtained in Figure 6. The values of k_1 and K_1 obtained from this fit are plotted in an Arrhenius plot, as shown in Figure 7. The following values were found valid for the range of temperatures of the experiments.

$$k_1(\text{sec}^{-1}) = 1.90 \times 10^{12} \exp(-33,200/T)$$

$$K_1(\text{lt/mol}) = 5.01 \times 10^{-9} \exp(28,700/T)$$

Note that the value for the free energy of chemisorption is approximately half of the oxygen-oxygen bond energy.

Equilibrium between gaseous and chemisorbed oxygen is rapidly achieved, the limiting step being the surface reaction that involves the formation of some surface intermediate. Therefore, the morphology of the material has to be taken into account in any comparison with other results.

Secondary Reactions and Mechanism

The above results cannot be used to deduce conclusively the mechanism of oxidation. A weight increase in the early part of the oxidation would indicate formation of sulfate, or oxysulfate formation. The converse is not true. The weight loss observed could be consistent with intermediate sulfate or oxysulfate formation, provided the decomposition of these compounds is much faster than their formation.

In the different experiments performed in fixed-bed reactors described in [10], evidence of sulfate decomposition was observed after the regeneration with air was completed. Briefly summarized, when sulfidation was performed using a freshly prepared ZnO sorbent, very little SO_2 could be seen at the bed outlet. However when a regenerated bed was used for the same sulfidation, an early peak of SO_2 was observed, indicating the presence of traces of $ZnSO_4$. The sulfate reacted with the H_2 of the inlet gas to give a mixture of ZnS and ZnO and SO_2 as discussed by Krishnan et al. [11].

To check the hypothesis that reaction (3) followed by sulfate decomposition is not the reaction mechanism, sulfate was formed by reacting SO_2 and O_2, with ZnO in a platinum pan hanging inside the thermobalance. Sulfate formation was rapid under these conditions, evidently proceeding by the SO_3 formed

by the oxidation of SO_2 catalyzed by platinum. A stream of nitrogen was then introduced and the decomposition of sulfate was monitored. The decomposition rate passed through a maximum value, because of the increase of the interfacial area between sulfate and oxide. The average maximum value of the decomposition rate among several runs was 3.1×10^{-4} sec^{-1}. The rate of weight loss per unit initial weight measured during ZnS oxidation experiments was at least one order of magnitude larger. This comparison shows that reaction (2) followed by sulfate decomposition is incompatible with the weight loss observed in the oxidation experiments. The conclusion is that regeneration occurs by reactions (1) and (2) alone.

Experiments were conducted to measure the rate of sulfate formation *via* reaction (2), using fresh ZnO and various SO_2 and O_2 concentrations. The conversion was defined as for α_1 above, but assuming $ZnSO_4$ as the final product. As expected, the reaction rate decreased with conversion. Later, the rate reached a constant value varying in the range $0.5 - 3.5 \times 10^{-7} sec^{-1}$ for different experiments. Although very low, this rate is sufficient to form small amounts of undesirable $ZnSO_4$ in a fixed-bed reactor.

Oxygen chemisorption seems to be an important step in the mechanism of the oxidation *via* reaction (1). Since SO_2 can also chemisorb, its influence was investigated, repeating some of the previous experiments adding SO_2 to the air-nitrogen mixtures. No appreciable difference was obtained in the weight *vs.* time curve. Once the oxidation was over, however, the weight started to increase slowly, because of the sulfate formation *via* reaction (2). This reaction was probably present all along the experiment, but too slow to be detected. Given the slow rates of sulfation, only the initial rates of weight increase were taken into consideration. The results were in the range 1.7-2.3 $\times 10^{-5} sec^{-1}$ for SO_2

compositions in the range 0.5-2.5 %. These values are one order of magnitude greater than those observed when using pure ZnO as starting material, indicating that reaction (1) produces ZnO *in situ* in a form that is considerably more active than the stabilized ZnO and/or has a higher specific surface area and different morphology.

CONCLUSIONS

Experimental work was focused on the regeneration of a high surface area bulk ZnO sorbent for high-temperature desulfurization of fuel gas streams. It was established that the oxidation of ZnS to ZnO follows the direct route, with no intermediate compounds. The kinetics of the oxidation of ZnS was found to follow a Langmuir-type expression, indicating that the surface reaction is the limiting step. Any sulfate or oxysulfate formed derives from a secondary reaction of SO_2 and O_2 with freshly formed ZnO. The TGA experiments yielded very low reaction rates for these secondary reactions. Finally, differences observed in the reactivity of fresh and regenerated ZnO with SO_2 suggest further studies.

REFERENCES

1.- Stull D.R., Prophet H. *Editors, JANAF Thermochemical Tables* . NSRDS-NBS 37, U.S Government Printing Office: Washington, DC, 1971.

2.- Pankratz L.B. *U.S. Bureau of Mines Bull.*, 1972, 672.

3.- DeCock C.W. *U.S. Bureau of Mines*, I.C., 1982, 8910.

4.- Barin I. and Knacke O. Termodynamic Properties of Inorganic Substances. *Springer Veralg*, New York, 1973.

5.- Prabhu G. M., Ulrichson D.L. and Pulsifer A.H. *I&EC, Fund.*, 1984, **23**, 271.

6.- Cannon K.J. and Denbigh K.G. *Chem. Engng Sci.*, 1957, **6**, 145.

7.- Ong J.N., Wadsworth M.E., Fassell W.M. *Trans. Soc. AIME*, 1956, **206**, 257.

8.- Fukunata Y., Monta T., Asaki Z. and Kondo Y. *Metallurgical Transactions B*, 1976, **7B**, 307.

9.- Marcilly C., Courty P. and Delmon B.. *J. Am. Cer. Soc.*, 1970, **53**, 1, 56.

10.- Flytzani-Stephanopoulos M., Gavalas G.R., Tamhankar S., Sharma P.K. *Final Report to DOE. DOE/MC/20417-1898. Jet Propulsion Laboratory and California Institute of Technology*, 1985.

11.- Krishnan G.N., Lamoreaux R.H., Brittain R.D. and Wood B.J. *Quarterly Progress Report 1 to DOE, Contract No. DE-AC21-83MC20092.* SRI International, Menlo Park, California, 1983.

TABLE 1

Maximum Rates Observed in ZnS Oxidation Runs

TEMPERATURE (^{0}C)	C_{O_2} (% vol)	RATE $\times 10^3$ (sec^{-1})
700	0.161	2.355
700	0.161	2.064
700	0.160	1.761
700	0.160	1.671
700	0.160	1.875
700	0.090	1.618
700	0.090	1.403
700	0.045	1.284
700	0.045	1.232
700	0.160	1.818
700	0.161	2.182
700	0.209	2.033
700	0.209	2.269
700	0.108	2.017
700	0.096	1.897
700	0.070	1.380
700	0.023	0.702
700	0.018	0.621
700	0.209	2.613
675	0.209	0.8388
675	0.209	0.7349
675	0.209	0.8348
675	0.129	0.7334
675	0.052	0.5855
675	0.094	0.7400
675	0.051	0.7107
675	0.209	1.0080
675	0.209	0.9946
675	0.209	1.0420
650	0.209	0.3873
650	0.209	0.4513
650	0.139	0.4052
650	0.111	0.4837
650	0.059	0.3070
650	0.051	0.3579

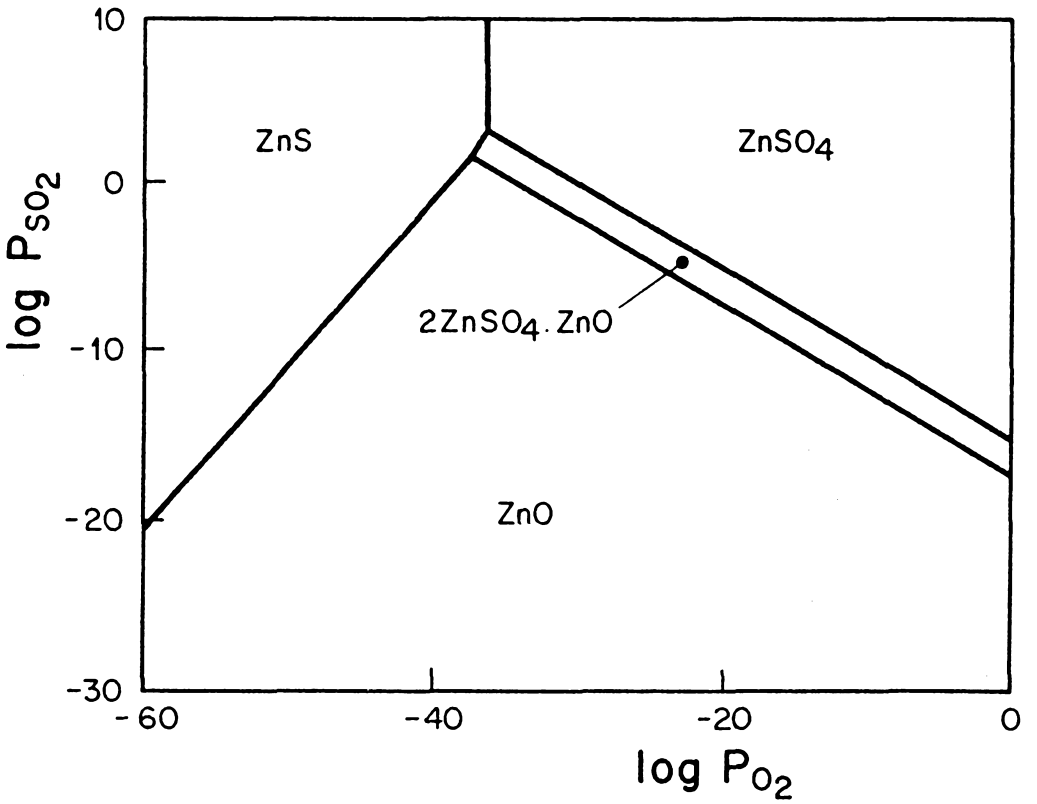

Figure 1: Thermodynamic Stability Diagram for the Zn-S-O System (800°K).

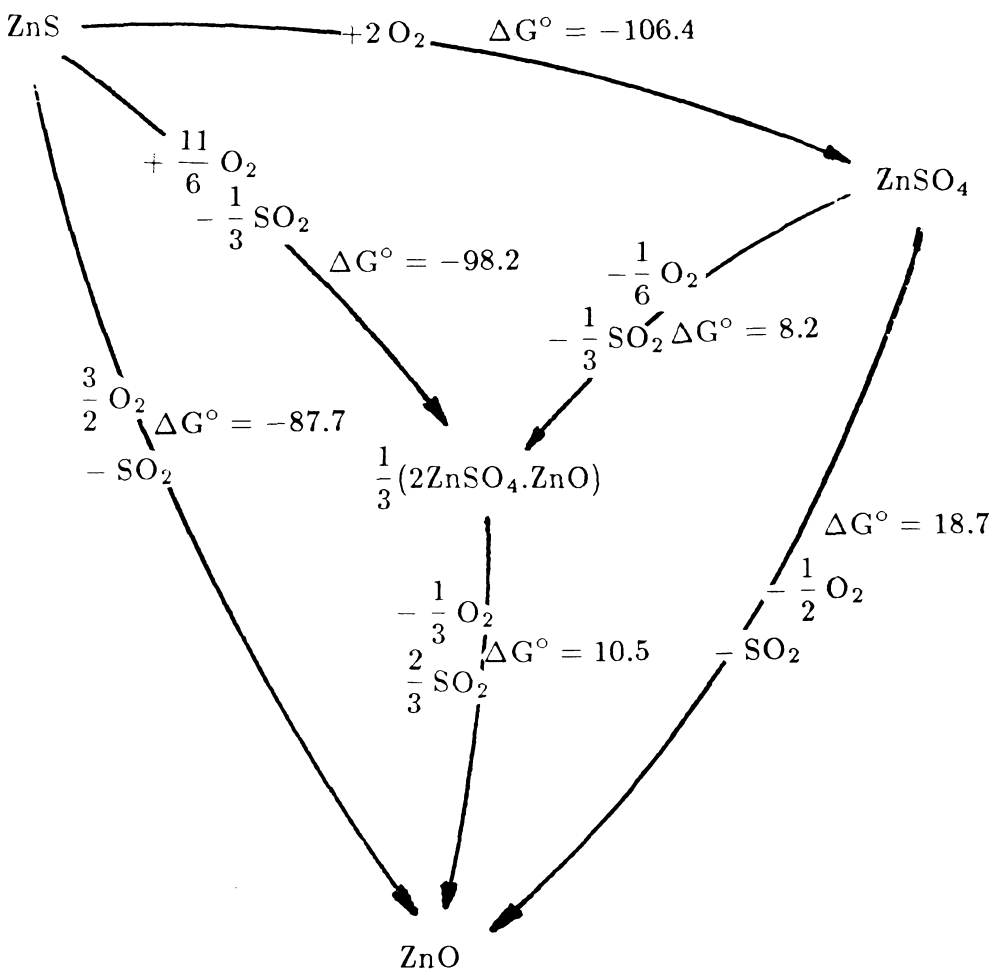

Figure 2.- Possible Routes for ZnS Oxidation.
Addition (+) and Release (-) of Gaseous Species are Indicated
Free Energy Changes (ΔG° (Kcal/mol)) are at 1000°K.

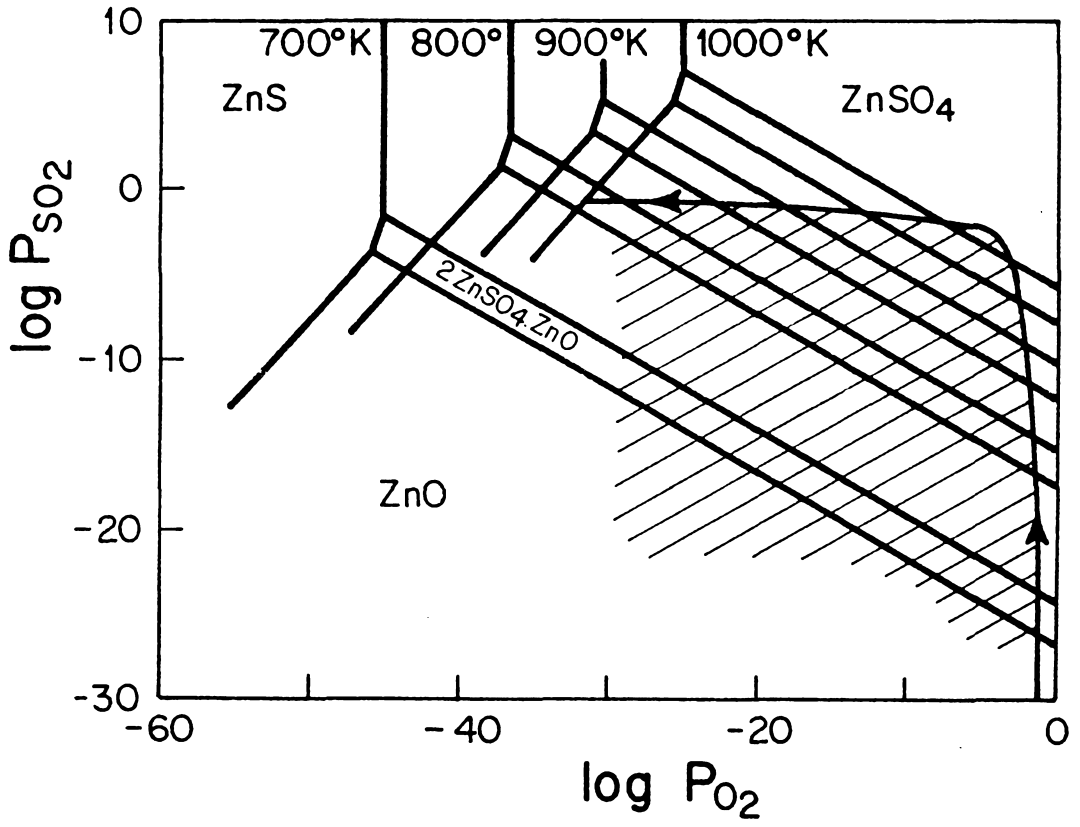

Figure 3: Material Balance Relation between P_{SO_2} and P_{O_2} inside a Fixed-Bed Reactor.

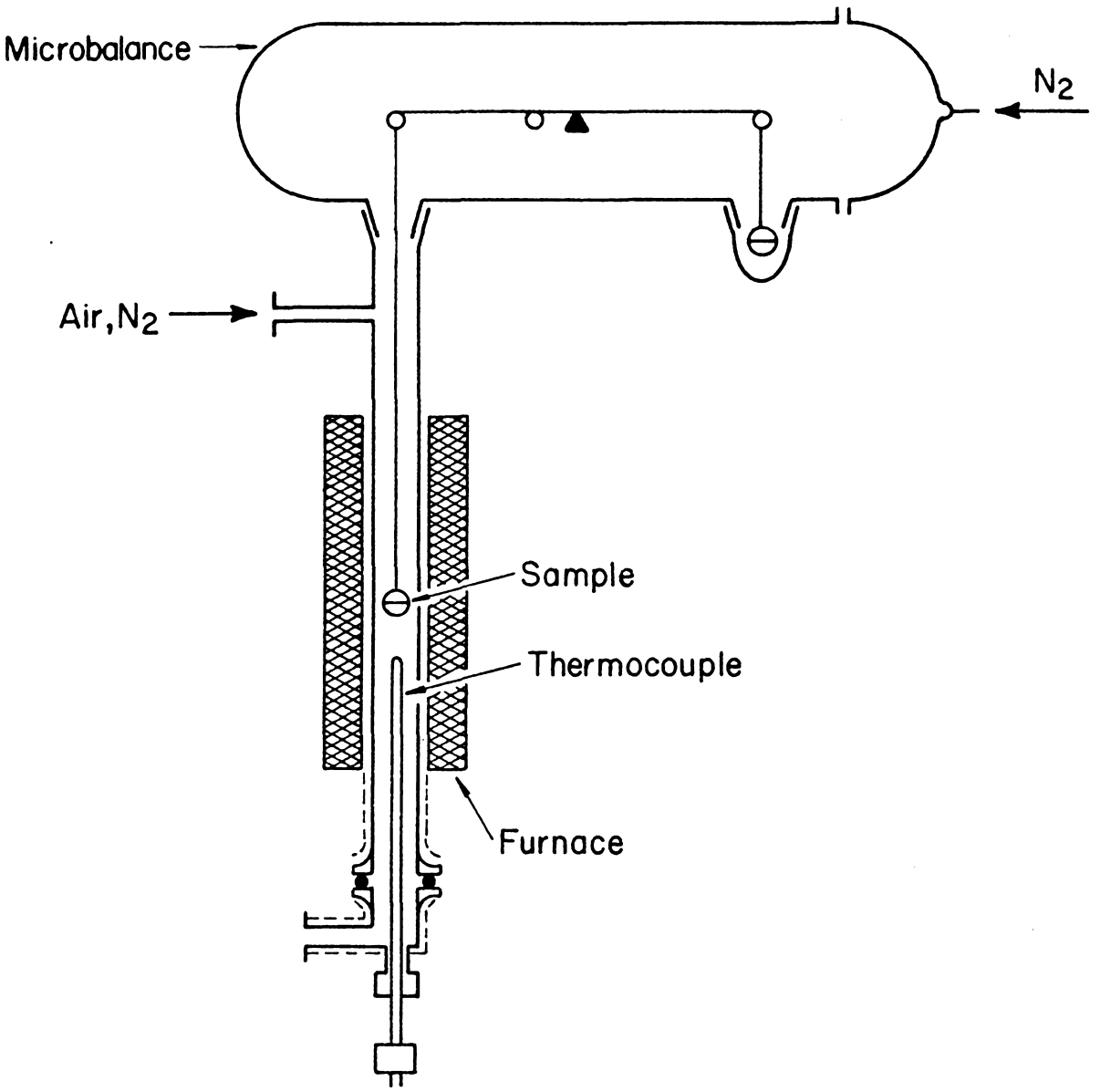

Figure 4: Schematic of the Thermogravimetric Balance.

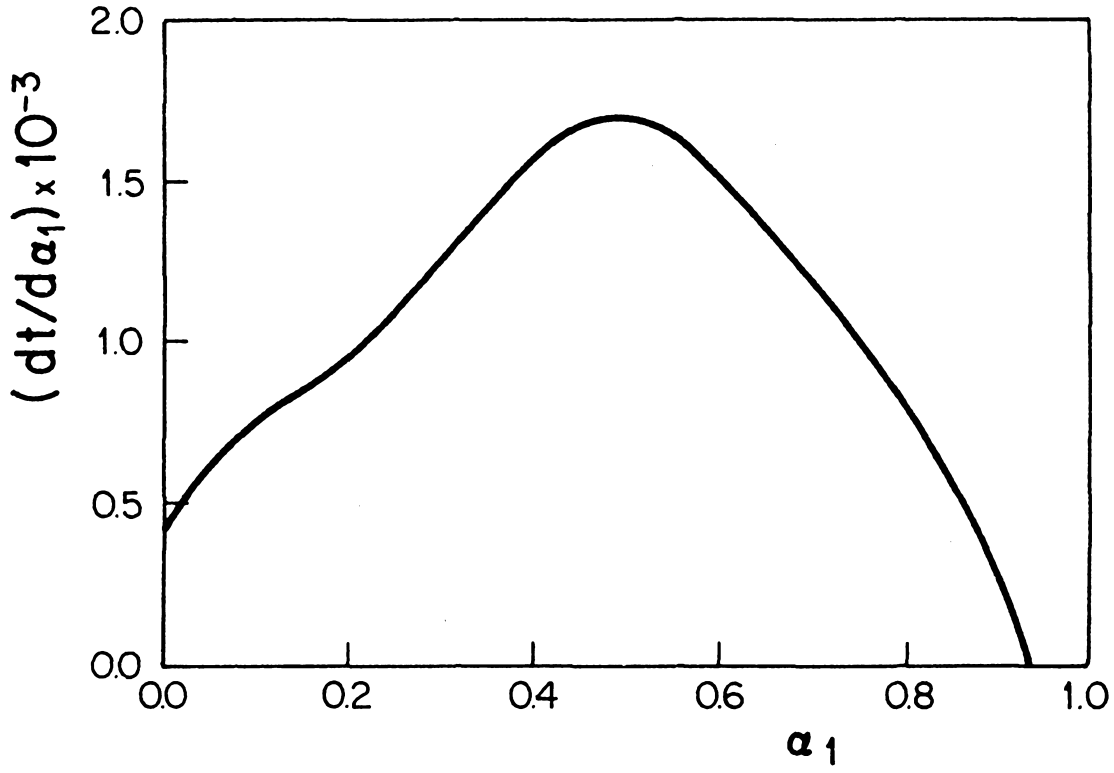

Figure 5: Typical Rate *vs.* Conversion Plot for ZnS Oxidation Experiments.

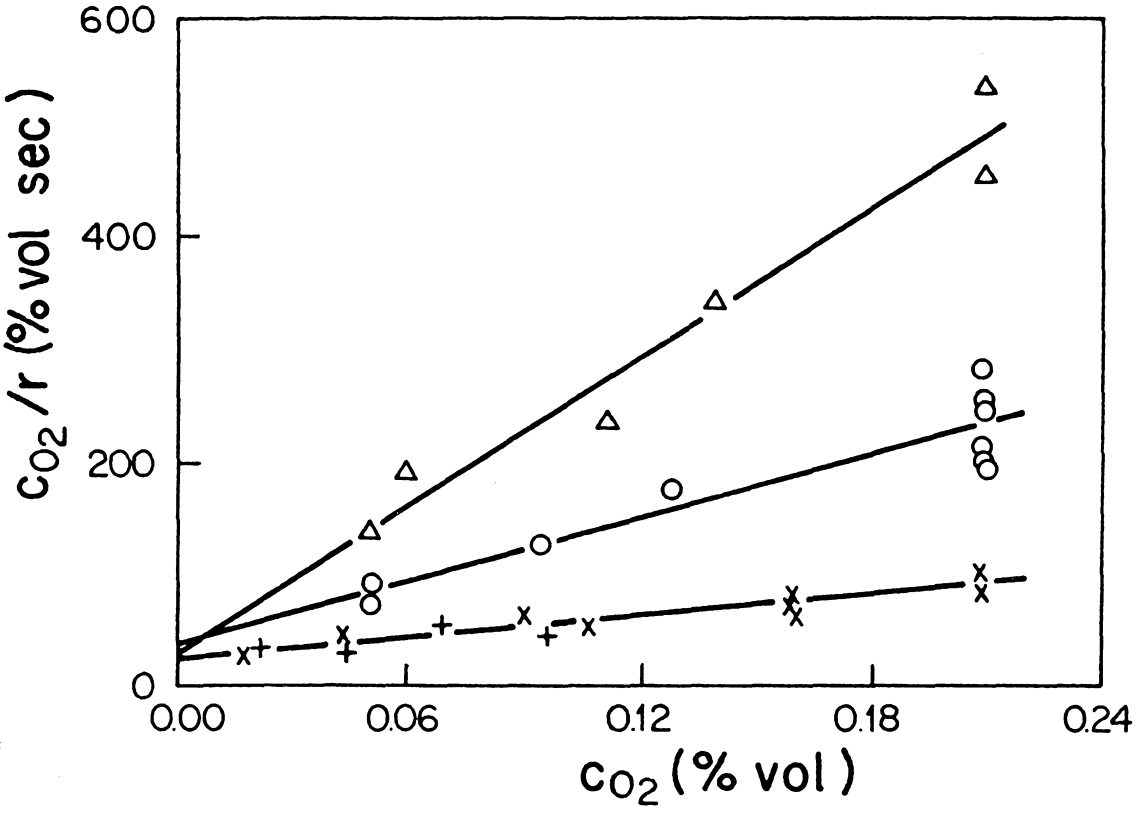

Figure 6: Maximum Rate of Oxidation *vs.* Oxygen Concentration.

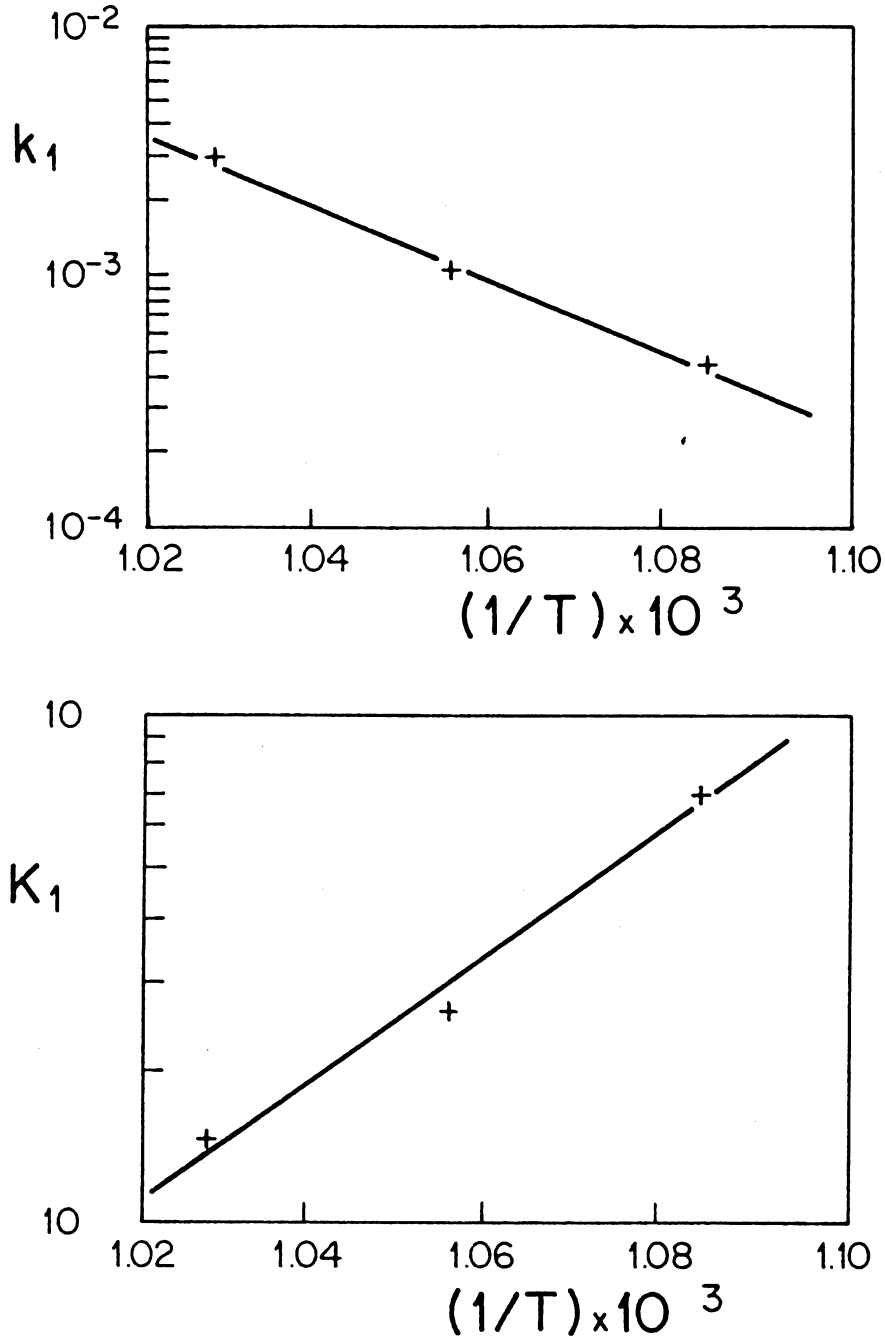

Figura 7: Arrhenius Plots for Rate Constant k_1 and the Equilibrium Constant K_1 of ZnS Oxidation.

CHAPTER VII

Aquí me pongo a cantar
Al compás de la vigüela

del Martín Fierro

MODELING OF A FIXED-BED GAS-SOLID REACTOR

The analysis that follows is restricted to a single isothermal gas-solid reaction taking place in a fixed-bed reactor. Chapter IX presents a treatment of the nonisothermal case, with special application to ZnS regeneration.

Consider the following general reaction occurring in a fixed-bed reactor

$$A_{(g)} + \nu_R R_{(s)} \longrightarrow \nu_B B_{(g)} + \nu_P P_{(s)} \qquad (1)$$

under the following assumptions:

1.- Properties in the radial direction are uniform. This allows a 1-D reactor model.

2.- Continuity equations are written for both stationary and moving phases. Normally, this assumption leads to the so-called pseudohomogeneous family of models.

3.- Reactor is isothermal: Inlet gases are fed at reactor temperature and heat of reaction is dissipated appropriately.

4.- Either the reaction is equimolar and no change of number of moles with conversion occurs, or the reactant concentration (c_A^0) is low. The latter case covers desulfurization reactions. Under these conditions the molar flux and the velocity of the gas phase (u) is constant. From the mathematical point of view, the system of equations becomes semilinear.

5.- Feed concentrations are independent of time. This permits the use of an overall material balance relating the concentration of gaseous reactant and products. For irreversible kinetics, this assumption is not needed.

6.- The reaction rate depends only on reactant and product concentration. If reaction rate depends on other physical parameters, such as porosity, a governing equation for such changes is also needed.

7.- Intraparticle diffusion is considered to be fast. If this is not the case, an additional equation for reaction and diffusion inside the particle has to be included in the model. A detailed treatment of this last case is given in [1].

Using the above assumptions, the following system of continuity and overall balance equations can be written

$$\frac{\partial c_A}{\partial t} + u\frac{\partial c_A}{\partial z} = D_{Aeff}\frac{\partial^2 c_A}{\partial z^2} - r_A\frac{(1-\epsilon_0)}{\epsilon_0} \tag{2}$$

$$\frac{\partial c_R}{\partial t} = -\frac{r_A}{\nu_S} \tag{3}$$

$$(c_R - c_R^0) + (c_P - c_P^0)\frac{\nu_R}{\nu_P} = 0 \tag{4}$$

$$(c_A - c_A^0) + (c_B - c_B^0)\frac{1}{\nu_B} = 0 \tag{5}$$

We will use the dimensionless variables

$$y_A = \frac{c_A}{c_A^0} \qquad y_R = \frac{c_R}{c_R^0} \qquad \varsigma = \frac{z}{L_c} \qquad \tau = \frac{t}{t_c} \qquad \Omega_A = \frac{r_A}{r_A^0}$$

$$Pe = \frac{L_c^2}{D_{Aeff}t_c}$$

where the following characteristic time t_c and length L_c can be chosen as

$$t_c = \frac{L}{u} \qquad L_c = L$$

where L is the reactor length. With this choice, t_c becomes the time needed for the main stream to travel along the reactor. In this case the Peclect number is essentially the ratio of convection and diffusion rates. This is the most suitable choice for slow reactions.

With the alternative definition

$$t_c = \frac{\epsilon_0 c_A^0}{(1-\epsilon_0) r_A^0}$$

the characteristic time t_c is the time needed to consume an initial concentration c_A^0 at the rate r_A^0, and the Peclect number becomes the ratio of the rates of reaction and diffusion. For fast reactions this last choice should be preferred.

The non-dimensional equations now become:

$$\frac{\partial y_A}{\partial \tau} + \xi \frac{\partial y_A}{\partial \zeta} = \frac{1}{Pe} \frac{\partial^2 y_A}{\partial \zeta^2} - \Omega_A \tag{6}$$

$$\frac{\partial y_R}{\partial \tau} = -\delta \Omega_A \tag{7}$$

where

$$\xi = \frac{u}{L_c} t_c \qquad \delta = \frac{\epsilon_0}{\nu_S (1-\epsilon_0)} \frac{c_A^0}{c_R^0}$$

The choice $\xi = 1$ allows the definition of a characteristic length $L_c = u/t_c$. Clearly, for any reaction rate expression, the characteristic length is now the width of the traveling concentration wave. Fast reactions provide a very thin "reaction front," whereas for relatively slow reactions, the front extends through a region comparable to the reactor length L. The former case is typical of the sulfidation reaction fronts, and as will be seen later in this chapter and in Chapter IX it allows the possibility of introducing traveling wave solutions.

In gas solid reactions δ is a small number, since it is the ratio of gaseous to solid densities. However, in the case of supported sorbents, the support occupies a large fraction of the solid volume, and consequently, δ is not necessarily very small. For CAT-15Z, $\delta = 0.02$. In any case, when the reaction rate is fast the product $\delta\Omega_A$ may not be small. Using the equation of Fuller *et al.* (in [2] Eq. 3-133) to estimate the diffusivity of H_2S in nitrogen, a value of 1.53 cm^2/sec is obtained. Accordingly, a typical Peclect number for the sulfidation experiments conducted at JPL is estimated as Pe= 2.6×10^{10}.

Neglecting the axial dispersion term in the above equation yields the following system of equations:

$$\frac{\partial y_A}{\partial \tau} + \frac{\partial y_A}{\partial \zeta} = -\Omega_A(y_A, y_R) \tag{8}$$

$$\frac{\partial y_R}{\partial \tau} = -\delta\Omega_A(y_A, y_R) \tag{9}$$

In the majority of cases, the reaction rate Ω_A is expressed as a product of two factors, one depending on y_A and the other on y_R. Many models have been proposed [3] to account for the factor depending on y_R (i.e., the solid conversion).

Equilibrium Case

In a reversible reaction, with the forward and reverse reactions both being very fast, equilibrium can be considered to hold everywhere in the reactor. The equilibrium relationship can be expressed as $y_R = f(y_A)$. Replacing Ω_A in Equation (8) by the expression given in Equation (9), and using the equilibrium relationship, we obtain

$$\frac{\partial y_A}{\partial \tau} + v\frac{\partial y_A}{\partial \zeta} = 0 \tag{10}$$

$$v = \frac{1}{1 - f'(y_A)/\delta} \tag{11}$$

The above is a hyperbolic PDE for which the characteristics are straight lines. The slope of these characteristic lines is determined by the initial and boundary conditions. For the majority of the cases they are $y_A(0,\varsigma) = 0$ and $y_A(\tau,0) = 1$. If $f'(0) < f'(1)$, as happens in the case of reactions with high equilibrium constants, a multivalued region is obtained, as is shown in the schematic diagram below. Conversely, when the equilibrium constant is low, $f'(0) > f'(1)$, and the solution is represented by an expansion fan.

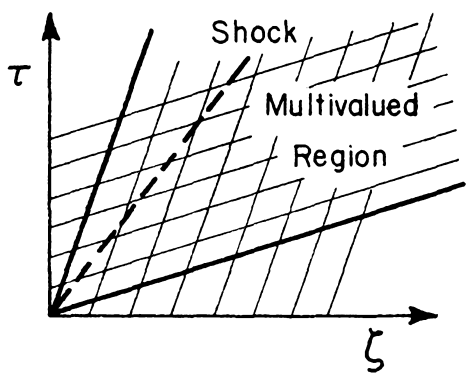

$f'(0) < f'(1)$

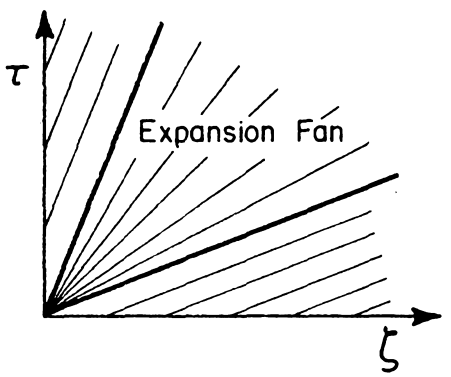

$f'(0) > f'(1)$

The multivalued region is clearly unacceptable, and a weak solution or shock layer has to be introduced. The shock travels along the reactor with velocity given by

$$v = \frac{\delta}{\delta + [f(0) - f(1)]}$$

and the concentrations are $y_A = 1$ behind and $y_A = 0$ ahead of the shock.

A Useful Transformation

With the following transformations

$$\eta = \varsigma - \tau \quad ; \quad \sigma = \varsigma$$

the system of Equations (8) and (9) reduces to

$$\frac{\partial y_A}{\partial \sigma} + \frac{1}{\delta}\frac{\partial y_R}{\partial \eta} = 0 \tag{12}$$

$$\frac{\partial y_R}{\partial \eta} = \delta\Omega(y_A, y_R) \tag{13}$$

Equation (12) suggests the introduction of a "stream function." Thus, following [4-5], we define $\Psi_\eta = y_A$ and $\Psi_\sigma = -\frac{1}{\delta}y_R$, so that Equation (12) is satisfied automatically and (13) transforms to

$$\Psi_{\sigma\eta} + \Omega_A = 0 \tag{14}$$

This transformation can be useful for nonlinear kinetics, whereas for linear kinetics integral transformations can be applied directly on Equations (12-13).

Some Exact Solutions

First-Order Reaction for the Gas Concentration and Zero-Order in the Solid Concentration

In the case

$$r_A = kc_A - k'c_B$$

one gets

$$\Omega_A = ay_A - b$$

where a and b are constants depending on k, k′, c_A^0 and c_B^0 (b=0 when k′ =0). The solution can be found *via* a Laplace transformation of Equation (8) or by the direct integration of Equation (12). The solution is:

$$y_A = \left[\frac{b}{a} + (1 - \frac{b}{a})e^{-a\sigma}\right]H(\tau - \varsigma)$$
$$y_R = 1 - \delta(a - b)e^{-a\sigma}\tau$$

The concentration at $\varsigma > \tau$ is clearly zero, since no reactant has arrived yet, hence the use of the Heaviside function H. The solution presents a discontinuity

at $\zeta = \tau$, as a consequence of neglecting the diffusive term in a region where diffusion is clearly important.

After a time given by $\tau^* = \frac{1}{\delta(a-b)}$, the solid is totally consumed at the reactor inlet (σ=0) and the above solutions are no longer valid . A new front carrying the values $y_R = 0$ and $y_A = 1$ starts to travel along the reactor. Denoting the front speed by v, we note that the equation

$$\frac{\partial y_A}{\partial \sigma} = -a y_A + b$$

is still valid ahead of the front, and can be solved using the following moving boundary condition,

$$y_A = 1 \qquad \text{when} \qquad \sigma = \sigma^* = v\tau$$

After solving for y_A and using $y_R = 1$ for $\sigma \longrightarrow \infty$ we obtain

$$y_A = \frac{b}{a} + (1 - \frac{b}{a})e^{-a(\sigma-\sigma^*)}$$

$$y_R = 1 - e^{-a(\sigma-\sigma^*)}$$

$$v = (1 - \frac{b}{a})\delta$$

First-Order Reaction in the Gas and the Solid Concentrations

In the case of the following reversible reaction rate $r_A = kc_Ac_R - k'c_Bc_P$ elimination of c_B and c_P using (4) and (5) and replacement in (14) produces

$$\Psi_{\sigma\eta} + a_1\Psi_\sigma\Psi_\eta + a_2\Psi_\sigma + a_3\Psi_\eta + a_4 = 0$$

where the constants a_i depend on $k, k', \delta, \xi, c_B^0$ and c_A^0. Now, by virtue of the following transformation

$$\Phi = e^{a_1\Psi + a_2\eta + a_3\sigma}$$

one obtains

$$\Phi_{\sigma\eta} + (a_4 a_1 - a_2 a_3)\Phi = 0$$

where $a_2 = 0$ for the irreversible case.

To determine the boundary conditions we note that for $\eta > 0$, $y_A = 0$, since no reactant has reached the corresponding portions of the bed. At the points for which $\eta = 0$ y_A is discontinuous in view of the fact that diffussion was neglected. Clearly, at $\eta = 0$ the solid concentration is $y_R = 1$. Finally, at $\zeta = 0$ the gas concentration is $y_A = 1$. Thus, the boundary conditions are

$$\Psi_\sigma = -\frac{1}{\delta} \quad \text{at } \eta = 0$$

$$\Psi_\eta = 1 \quad \text{at } \sigma = 0$$

Once the Riemman function is determined, the solution is found to be

$$\Phi(\sigma,\eta) = I_0\left(2\sqrt{\lambda\sigma\eta}\right) + \int_0^\sigma e^m\, I_0\left(\sqrt{\lambda\eta(\sigma - m)}\right)dm$$
$$-(a_1 + a_2)\int_0^\sigma e^{-(a_1+a_2)p}\, J_0\left(\sqrt{\lambda\sigma(\eta - p)}\right)dp$$

where $\lambda = a_4 a_1 - a_2 a_3$.

In the case of irreversible reaction ($k' = 0$) the above expressions give:

$$y_A = \frac{1}{1 - e^{\delta\eta}(1 - e^{\sigma})}$$

$$y_R = \frac{1}{1 - e^{-\sigma}(1 - e^{-\delta\eta})}$$

Approximate Solutions

Traveling Wave Solution

Introducing the transformation

$$\theta = \zeta - v\tau$$

$$\sigma = \zeta$$

the system of equations (8) and (9) becomes

$$(-v+1)\frac{\partial y_A}{\partial \theta} + \frac{\partial y_A}{\partial \sigma} = -\Omega_A \tag{15}$$

$$-v\frac{\partial y_R}{\partial \theta} = -\delta\Omega_A \tag{16}$$

Equations (15),(16) admit a travelling wave solution, independent of σ. Eliminating Ω_A between (15) and (16) and integrating, we obtain

$$y_A^* = M - \frac{v}{\delta(1-v)}y_R^*$$

$$\frac{dy_R^*}{d\theta} = \frac{\delta}{v}\Omega_A$$

where the superscript $*$ is used to indicate the approximate solution, and v is the velocity of the travelling wave.

The boundary conditions are

$$\left.\begin{aligned} y_A^* &= y_{A_1} \\ y_R^* &= y_{R_1} \end{aligned}\right\} \quad \text{at} \quad \theta = \theta_1$$

$$\left.\begin{aligned} y_A^* &= y_{A_2} \\ y_R^* &= y_{R_2} \end{aligned}\right\} \quad \text{at} \quad \theta = \theta_2$$

Using the boundary conditions, we find the wave velocity v and the constant M to be

$$v = \frac{(y_{A_1} - y_{A_2})\delta}{(y_{R_2} - y_{R_1}) + \delta(y_{A_1} - y_{A_2})}$$

$$M = \frac{y_{A_1}y_{R_2} - y_{A_2}y_{R_1}}{y_{R_2} - y_{R_1}}$$

The following ODE, with the proper boundary conditions remains to be solved:

$$\frac{dy_R^*}{d\theta} = \left(\frac{1}{P} + \delta\right)\Omega(M - Py_R^*, y_R^*) \tag{17}$$

where

$$P = \frac{y_{A_1} - y_{A_2}}{y_{R_2} - y_{R_1}}$$

In most cases it is reasonable to set

$$\theta_1 = -\infty \qquad y_{A_1} = 1 \qquad \Omega(1, y_{R_1}) = 0 \tag{18}$$

$$\theta_2 = \infty \qquad y_{A_2} = 1 \qquad \Omega(y_{A_2}, 1) = 0 \tag{19}$$

which will be called "equilibrium conditions at infinity." Boundary condition (18) states that equilibrium conditions apply upstream ($y_A = 1$), whereas condition (19) states that the solid sufficiently downstream of the wave is unreacted.

For the special case of the rate expression $r_A = kc_Ac_R - k'c_Bc_P$, Equation (17) takes the form

$$\frac{dy_R^*}{d\theta} = ay_R^{*2} + by_R^* + c$$

where a,b and c are combinations of $M, P, \delta, k, k', c_B^0, c_A^0$

For the irreversible case ($k'=0$), one obtains

$$y_R^* = \frac{1}{1 + e^{-(1+\delta)\theta}}$$

$$y_A^* = (1 - y_R^*) = \frac{1}{1 + e^{(1+\delta)\theta}}$$

Recall that this last irreversible case was solved analytically. Expressing the exact solution in terms of the variable pair (σ,θ), we find

$$y_R = \frac{1}{1 + e^{-(1+\delta)\theta} - e^{-\sigma}}$$

$$y_A = \frac{1}{1 + e^{(1+\delta)\theta}(1 - e^{-\sigma})}$$

Since $y_R e^{-\sigma} < 1$, one can put

$$y_R^* = \frac{y_R}{1 + y_R e^{-\sigma}} = y_R\left[1 + \sum_{n=1}^{\infty}(-y_R)^n e^{-n\sigma}\right]$$

$$y_A^* = y_A\frac{(1 - e^{-\sigma})}{1 - y_A e^{-\sigma}} = y_A(1 - e^{-\sigma})\left[1 + \sum_{n=1}^{\infty}(-y_A)^n e^{-n\sigma}\right]$$

The velocity of the traveling wave is

$$v = \frac{\delta}{1+\delta}$$

and since δ is large, the approximation is good. The error in the approximate wave solution is small for large σ , that is , far from the reactor inlet.

Cumulative Concentration . An Integral Transformation

When $\Omega_A = y_A g(y_R)$, a cumulative concentration Λ can be defined by

$$\Lambda = -\int_1^{y_R} \frac{dt}{g(t)} \tag{20}$$

as was suggested by Dudukovic [6] and Del Borghi *et al* [7] for this type of kinetics in pellets. Integrating (13), it is easy to see that :

$$\Lambda = \delta \int_\varsigma^\eta y_A(\sigma, t)\, dt \tag{21}$$

Equation (20) defines a functional relationship $y_R = Y(\Lambda)$, which in some cases may be obtained explicitly.

Integrating Equation (12), using Leibnitz' rule for differentiation under an integral and using (21), one obtains

$$\frac{\partial \Lambda}{\partial \sigma} - Y(\Lambda) = -1 \tag{22}$$

The solution of Equation (22) provides y_R as a function of σ but fails to give information about y_A.

In the case $\Omega_A = y_A y_R$ Equation (20) can be solved to give $y_R = e^{-\Lambda}$ and Equation (22) yields

$$y_R = \frac{1}{1 - C(\eta)e^{\sigma}}$$

where the function $C(\eta)$ remains undetermined.

REFERENCES

1.-: Evans J.W. and Song S., *Ind. & Eng. Chem., Proc. Des. Dev.*, 1974, **13**, 146.

2.-: Green D.W., *Editor*,Chemical Engineers Handbook, 5th Edition. *McGraw Hill*, New York, 1984.

3.-: Ramachandran P.A. and Doraiswamy L.K., *AIChE J.*, 1982, **28**, 6, 881.

4.-: Thomas H.C., *Annals of the New York Academy of Sciences*, 1948, **49**, 161.

5.-: Thomas H.C. *J. Amer. Chem. Soc.*, 1944, **66**,1664.

6.-: Dudukovic M. P. *AIChE J.*, 1976, **22**, 945.

7.-: Del Borghi M., Dunn J. C. and Bischoff K. B. *Chem. Engng Sci.*, 1976, **31**, 1065.

CHAPTER VIII

Que si un pueblo su dura cadena
no se atreve a romper con sus manos,
puede el pueblo mudar de tiranos
pero nunca ser libre podrá.

José María de Heredia

The contents of this chapter will be submitted to the *Chem. Eng. Sci.* Journal. It develops semi-analytical solutions of a class of equations describing gas-solid reaction and diffusion in isothermal pellets.

ANALYTICAL APPROXIMATE SOLUTIONS OF CERTAIN GAS-SOLID REACTION MODELS IN PELLETS

Miguel J. Bagajewicz*

California Institute of Technology

Pasadena, California 91125

* Now at INTEC, Casilla de Correo No 91, 3000, Santa Fe, Argentina

ABSTRACT

Analytical expressions that approximate the solutions of a class of gas-solid reaction problems are presented. These expressions are members of two monotone sequences of functions that are respectively pointwise upper and lower bounds of the solution of the problem. An approximate solution that lies between the bounds is proposed. The method is illustrated by application to different models of gas-solid reactions with linear and non-linear rate expressions. When the Thiele modulus is not very large, the method provides solutions with small deviation.

INTRODUCTION

Gas-solid non-catalytic reactions are important in many areas of chemical processing, such as hot gas desulfurization, metallurgy, coal combustion, catalyst regeneration, etc. The quantitative description of such reactions often involves the problem of reaction and diffusion inside pellets. Except for very simple cases, the pertinent partial differential equations do not accept closed form solutions. Although numerical methods for solving these equations are available, approximate analytical solutions of reasonable accuracy are of considerable interest. Such solutions display directly the effect of various parameters and can be used to guide experimental planning. They are also very useful in connection with reactor models, where numerical solution of the complete pellet-reactor problem would be very tedious and often impractical.

Approximate analytical solutions of gas-solid reaction problems were explored in a recent paper by Ramachandran [1]. The case of kinetics that are first order with respect to gas concentration, but general with respect to the solid conversion, was treated by introducing the device of cumulative concentration, which had been introduced independently by Dudukovic [2] and Del Borghi *et al.* [3]. As stated by Ramachandran [1], this method is applicable to a wide class of rate expressions yielding solutions valid for times less than a critical value, which depends on the particular model being used. Solid conversions corresponding to that time are usually in the range 0.5-0.7. Beyond these values the approximate solution breaks down. Except for the above limitation, the method produces very good results. However, the transformation that allows the definition of the cumulative concentration cannot be applied when the

reaction is not first order with respect to gas concentration. Therefore, the need remains for analytical methods for all the range of solid conversions and for rate expressions with non-linear dependence on the gas concentration.

In this paper a method is developed for deriving analytical expressions that approximate solid conversion and gas concentration profiles inside a pellet in the whole range of solid conversion. The approximate solutions are members of a sequence of functions that are bounds of the exact solutions. The upper and lower bounds are very close to each other for moderate values of the Thiele modulus. An approximate solution that falls between the upper and lower bound is also proposed.

PROBLEM FORMULATION

The conservation equations for the gas concentration and solid conversion inside a spherical pellet can be represented in the following dimensionless form.

$$\nabla^2 c = \frac{1}{\eta^2}\frac{\partial}{\partial \eta}\left(\eta^2 \frac{\partial c}{\partial \eta}\right) = \phi^2 G(X)F(c) \tag{1}$$

$$\frac{\partial X}{\partial \tau} = G(X)F(c) \tag{2}$$

where c represents the gas concentration, X represents the solid conversion, and ϕ is the Thiele modulus. For a wide range of gas-solid systems, the reaction rate is represented by a product of a factor dependent on the solid conversion G(X), where all the solid morphological parameters are taken into account, and a factor dependent on the gas concentration F(c). Equation (1) assumes implicitly that the diffusivity of the gas is independent of solid conversion.

The following boundary and initial conditions are standard and include external mass transfer resistance:

$$\frac{\partial c}{\partial \eta} = 0 \qquad \eta = 0 \tag{3}$$

$$\frac{\partial c}{\partial \eta} = \gamma(1 - c) \qquad \eta = 1 \tag{4}$$

$$X = 0 \qquad \tau = 0 \tag{5}$$

Boundary conditions (3) and (4) can be rewritten using a linear boundary operator B:

$$Bc = \underline{g} = \begin{pmatrix} 0 \\ 1 \end{pmatrix} \tag{6}$$

For convenience we define K(X) such that

$$K'(X) = \frac{1}{G(X)} \quad ; \quad K(0) = 0 \tag{7}$$

With this definition Equations (1) and (2) can be rewritten as follows:

$$\nabla^2 c - \phi^2 G(X) F(c) = 0 \tag{8}$$

$$\frac{\partial K(X)}{\partial \tau} = F(c) \tag{9}$$

The following development is restricted to the case $G'(X) < 0$.

SOLUTION PROCEDURE

It is physically clear that gas concentration decreases with decreasing radius within the pellet; i.e. the flux of the reactant is in the inward direction. This can be proved mathematically using the maximum principle for elliptic equations. Similarly, the solid conversion profile is monotone, decreasing towards the center of the particle. To prove this, take derivatives of Equation (9) with respect to η, integrate in time and use (7) to get:

$$\frac{\partial X}{\partial \eta} = G(X) \int_0^\tau F'(c) \frac{\partial c(\eta, \xi)}{\partial \eta} d\xi \tag{10}$$

Since $F'(c)$ is positive in practically all reported cases [4], there is no loss of generality in assuming monotonic increase of conversion with η.

The monotonic behavior of c and X permits the definition of two sequences of functions as follows.

Let $\{p_i, Z_i\}$ be defined by:

$$\left.\begin{aligned} \nabla^2 p_i - \phi^2 H_p(Z_i) F(p_i) &= 0 \\ B p_i &= \underline{0} \end{aligned}\right\} \tag{11}$$

$$K(Z_i) = \int_0^\tau P_{i-1}(\eta, \xi) d\xi \tag{12}$$

Similarly, let $\{r_i, Y_i\}$ be defined by

$$\left.\begin{aligned} \nabla^2 r_i - \phi^2 H_r(Y_i) F(r_i) &= 0 \\ B r_i &= \underline{0} \end{aligned}\right\} \tag{13}$$

$$K(Y_i) = \int_0^{\tau} R_{i-1}(\eta, \xi) d\xi \tag{14}$$

The functions $H_p(Z_i), H_r(Y_i), P_i(\eta, \xi)$ and $R_i(\eta, \xi)$ are chosen so as to obtain analytical solutions of Equations (11) and (13). As is shown later, the sequences $\{p_i, Z_i\}$ and $\{r_i, Y_i\}$ are upper and lower bounds of c and X, respectively, if $H_p(Z_i)$ and $H_r(Y_i)$ are defined in the following form: (see Figure 1):

$$H_p(Z_i) = \alpha_p(\tau) - \beta_p(\tau)\ \eta \tag{15}$$

$$H_r(Y_i) = \begin{cases} \alpha_{r,1}(\tau) & \eta \leq \eta^* \\ \alpha_{r,2}(\tau) - \beta_{r,2}(\tau)\ \eta & \eta > \eta^* \end{cases} \tag{16}$$

As can be inferred from Figure 1, $\alpha_p, \beta_p, \alpha_{r,1}, \alpha_{r,2}, \beta_{r,2}$ and η^* are given by:

$$\alpha_p = G(Z_i(0,\tau)) \tag{17}$$

$$\beta_p = G(Z_i(0,\tau)) - G(Z_i(1,\tau)) \tag{18}$$

$$\alpha_{r,1} = G(Y_i(0,\tau)) \tag{19}$$

$$\alpha_{r,2} = G(Y_i(1,\tau)) - \frac{\partial G(Y_i(1,\tau))}{\partial \eta} \tag{20}$$

$$\beta_{r,2} = -\frac{\partial G(Y_i(1,\tau))}{\partial \eta} \tag{21}$$

$$\eta^* = 1 + \frac{G(Y_i(0,\tau)) - G(Y_i(1,\tau))}{\frac{\partial G(Y_i(1,\tau))}{\partial \eta}} \tag{22}$$

Similarly, to make sure that the sequences of solutions will bound the exact solutions c and X, $P_i(\eta, \xi)$ and $R_i(\eta, \xi)$ are selected to be pointwise upper and lower bounds of $F(p_i)$ and $F(r_i)$, respectively. Piecewise linear bounds are here used, but any other integrable function can be selected. The following expressions cover some of the possible choices (see Figure 2)

$$R_i(\eta, \xi) = F[r_i(\eta, 0)] + \Delta_R \frac{\xi}{\tau} \tag{23}$$

$$P_i(\eta, \xi) = \begin{cases} F[p_i(\eta, 0)] + \Delta_P^0\ \xi & \xi \leq \tau^* \\ F[p_i(\eta, \tau)] + \Delta_P\ (\xi - \tau) & \xi > \tau^* \end{cases} \tag{24}$$

where the slopes Δ_R , Δ_P^0 and Δ_P satisfy the following inequalities:

$$0 \leq \Delta_R \leq \Delta_{R_{max}} = F[r_i(\eta,\tau)] - F[r_i(\eta,0)] \tag{25}$$

$$\Delta_P^0 \geq \Delta_{P_{min}}^0 = F'[p_i(\eta,0)]\frac{\partial p_i}{\partial \tau}(\eta,0) \tag{26}$$

$$0 \leq \Delta_P \leq \Delta_{P_{max}} = F'[p_i(\eta,\tau)]\frac{\partial p_i}{\partial \tau}(\eta,\tau) \tag{27}$$

When $\frac{\partial^2}{\partial \tau^2}F[p_i(\eta,0)] \leq 0$, $\Delta_R \neq 0$ and$\Delta_P^0 = \Delta_{P_{min}}^0$ are appropiate. The evaluation of $\frac{\partial p_i}{\partial \tau}(\eta,\tau)$ can be tedious, especially if the method is applied by hand, or when F(c) is non-linear. To avoid its calculation, Δ_P can be taken equal to zero. Non-zero values of Δ_P give only small improvements on the upper bound, especially for large values of time. More important improvements are obtained when the minimum value of Δ_P^0 is used.

The value of τ^* is given by

$$\tau^* = \frac{F[p_i(\eta,\tau)] - F[p_i(\eta,0)] - \tau\Delta}{F'[p_i(\eta,0)]\frac{\partial p_i}{\partial \tau}(\eta,0) - \Delta} \tag{28}$$

The following theorem was used to prove that both sequences defined above are indeed upper and lower bounds of the exact solutions c and X of Equations (1) and (2).

BOUNDING THEOREM:

If $s(\eta,\tau) < u(\eta,\tau)$ *and if* $V(\eta,\tau) < W(\eta,\tau)$ *are functions that satisfy boundary conditions* (2) (3) *and* (4) *and the following inequalities:*

$$\nabla^2 u - \phi^2 G(W)F(u) \leq 0 \qquad \frac{\partial K(W)}{\partial \tau} \geq F(u)$$

$$\nabla^2 s - \phi^2 G(V)F(s) \geq 0 \qquad \frac{\partial K(V)}{\partial \tau} \leq F(s)$$

then W,u *and* s,V *satisfy*

$$s \leq c \leq u$$

$$V \leq X \leq W$$

provided $G'(X) \leq 0$ and $F'(c) \geq 0$.

The proof of this theorem is given in Appendix 1.

The Bounding Theorem imposes a limitation on the dependence of the rate on solid conversion, namely, that $G'(X) < 0$. Models such as the grain model, where the reaction surface area decreases with conversion, satisfy this condition. The case when $G'(X) > 0$ in a certain interval of conversion requires major changes in the mathematical analysis and will not be considered in this paper.

The Approximate Solution

For practical purposes a single sequence of approximating functions, rather than the two sequences corresponding to upper and lower bounds, is more useful. Consider the sequence defined by the equations

$$\left.\begin{aligned} \nabla^2 \tilde{c}_i - \phi^2 H_p(\tilde{X}_i) F(\tilde{c}_i) &= 0 \\ B\tilde{c}_i &= \underline{0} \end{aligned}\right\} \tag{29}$$

$$K(\tilde{X}_i) = \left[F(r_0(\eta,0)) + F(\tilde{c}_i(\eta,\tau))\right]\frac{\tau}{2} \tag{30}$$

with $\tilde{X}_0 = 1$. Any member of this sequence can be used as an approximate solution for the problem. It is not difficult to prove that $\tilde{c}_i$ and $\tilde{X}_i$ lie between the pairs (r_i, p_i) and (Y_i, Z_i). This is shown in Appendix 2.

THE CASE OF LINEAR GAS KINETICS

For linear kinetics, $F(c)=c$, the solutions of Equations (11) and (13) are expressed in terms of Airy and Hyperbolic functions. These solutions are :

$$p_i(\eta,\tau) = \frac{a_p\, Ai(q_p(\eta,\tau)) + b_p\, Bi(q_p(\eta,\tau))}{\eta} \tag{31}$$

$$r_i(\eta,\tau) = \begin{cases} a_{r,1}\sinh(\phi\alpha_{r,1}\eta)/\eta & \eta \le \eta^* \\ \{a_{r,2}\,\mathrm{Ai}(q_r(\eta,\tau)) + b_{r,2}\,\mathrm{Bi}(q_r(\eta,\tau))\}/\eta & \eta > \eta^* \end{cases} \tag{32}$$

where Ai(z) and Bi(z) are Airy functions. The quantities a_p, b_p, a_r and b_r are determined in terms of α, β and η^*, which are defined in (17-22). Therefore, they are functions of time. Continuity of r_i and of its derivative with respect to η is required at η^*. The closed form solution for $\tilde{c}_i$ is of the same form as in (31).

Analytic inversion of K(X) is normally straightforward, but in some cases as in the grain model, it involves finding of the root of a single equation numerically.

First Members of the Sequences

We start with $Z_0 = 1$ as an upper bound and $Y_0=0$ as a lower bound. For $Z_0 = 1$ Equation (11) gives $p_0 = 1$. Using (12), one obtains $K(Z_1) = \tau$, which gives a conversion profile that depends on time only. The next term in the sequence is

$$p_1(\eta,\tau) = a_p\frac{\sinh(\phi[G(X_1)]^{1/2}\eta)}{\eta} \tag{33}$$

All the other members of the sequence of upper bounds have the form given by (31). For $Y_0 = 0$, (13) gives

$$r_0(\eta) = a_r\frac{\sinh(\phi\eta)}{\eta} \tag{34}$$

Using Equation (13), $K(Y_1) = r_0(\eta)\tau$, and the other members have the general form given by (32).

The function r_0 is independent of time and coincides with the concentration profile for τ=0, when the upper and lower bounds are identical.

As $\tau \to 0$, $\beta \to 0$ and direct substitution in (31) to evaluate $p_i(\eta,0)$ is not possible. The same difficulty appears when attempting to evaluate $\frac{\partial p_i}{\partial \eta}(\eta,0)$. In Appendix 3 a regular perturbation solution of Equation (11) is developed for small time. Values of $\frac{\partial p_i}{\partial \eta}(\eta,0)$ are obtained using the same technique.

Results

Expressions of G(X) for different models for which this technique can be applied are given in Table 1. For the case of the grain model [12,13], Figure 3 shows one pair of sequences of approximate solutions for the gas concentration, whereas Figure 4 shows the corresponding solid conversion profiles. These solutions include the effect of external mass transfer resistance. In general, no appreciable improvement is obtained after the third term of the sequence, and the calculations can be stopped at that point, or before when appropiate.

Table 2 shows results of the application of the method for selected values of the parameters. Values for $\tilde{c}_i$ and $\tilde{X}_i$ are compared to $\bar{c}_i$ and $\overline{X}_i$, which are in turn obtained in the following way.

$$\bar{c}_i(\eta,\tau) = \frac{1}{2}[r_i(\eta,\tau) + p_i(\eta,\tau)] \tag{35}$$

$$\overline{X}_i(\eta,\tau) = \frac{1}{2}[Y_i(\eta,\tau) + Z_i(\eta,\tau)] \tag{36}$$

Reults are shown only at the particle center ($\eta = 0$), where the difference between upper and lower bound is maximum. The deviation listed for $\bar{c}$ and $\overline{X}$ correspond to the difference of the averages from the corresponding bounds. For moderate values of the Thiele modulus, upper and lower bounds are very close, and there is no practical need for improvements. Note, for example, that the second members of the sequences already provide sufficiently accurate approximations. However, for larger values of the Thiele modulus, more terms may be needed, as shown in the last example of Table 2. Also, to improve results in this last case, Δ_R and Δ_P^0 are set equal to their limiting maximum and minimum values, respectively.

In general, it can be concluded that the error in the approximate solution increases with increasing Thiele modulus. If needed, these results can be improved using more linear segments to approximate $G(Z_i)$ and $G(Y_i)$. However, for large Thiele modulus, other models such as the Shrinking Core or the Zone models can provide good approximations more conveniently.

THE CASE OF NONLINEAR GAS KINETICS

When the reaction rate is not first order with respect to the gas concentration, the following Equations can be used to obtain upper and lower bounds of

Equations (11) and (13), respectively, as was suggested by Varma and Strieder [5].

$$\nabla^2 p_i - \phi^2 H_p(Z_i) F_h(p_i) = 0 \tag{37}$$

$$\nabla^2 r_i - \phi^2 H_r(Y_i) F_g(r_i) = 0 \tag{38}$$

Without loss of generality, assume that $F(c)$ is concave ($F''(c) \geq 0$). For this case, $F_g(c)$ and $F_h(c)$ are given by (see Figure 5):

$$F_g(c) = F(c_\alpha) + \frac{1 - F(c_\alpha)}{1 - c_\alpha}(c - c_\alpha) \tag{39}$$

$$F_h(c) = \begin{cases} F(c_\beta) + F'(c_\beta)(c - c_\beta) & c \leq \tilde{c} \\ 1 + F'(1)(c - 1) & c > \tilde{c} \end{cases} \tag{40}$$

Varma and Strieder [5] proposed the above equations to obtain bounds of the solution of non-linear elliptic problems of the type given in Equation (11) in which H_p is considered as a function of η, only. Based on an earlier result published by Amann [6] and Sattinger [8], proof is given in [5] that the solutions of (37) and (38) yield upper and lower bounds for the solutions of Equations (11) and (13), respectively. The reader is referred to these earlier results for more details and mathematical justification.

Consider the case of Equation (13) and (38). To guarantee that the solution of Equation (38) will be a lower bound of the solution of (13), c_α has to be an absolute lower bound of r_i. A first obvious selection is $c_\alpha = 0$. Call this solution $r_{i0}(\eta, \tau)$. If now c_α is chosen as $r_{i0}(0, \tau)$, a higher lower bound of $r_i(\eta, \tau)$ will be obtained. The repetition of this procedure will produce a monotone non-decreasing sequence of lower bounds $r_{ij}(\eta, \tau)$. This convergent process can be continued until the difference in successive terms becomes smaller than a predetermined quantity. Evaluation of this entire sequence of terms to obtain the final value of c_α is equivalent to solving the following trascendental equation:

$$c_\alpha = v(0, \tau) + \phi^2 \frac{(F(c_\alpha) - c_\alpha)}{(1 - c_\alpha)} \int_0^1 L_v(\rho, \eta, \tau) H_r[Y_i(\rho, \tau)] d\rho \tag{41}$$

where $v(\eta, \tau)$ and $L_v(\eta, \rho, \tau)$ are, respectively, the solution and the Green function of the following problem

$$\left.\begin{aligned} \nabla^2 v - \phi^2 H_r(Y_i) \frac{[1 - F(c_\alpha)]}{(1 - c_\alpha)} v = 0 \\ Bv = \underline{g} \end{aligned}\right\} \tag{42}$$

The reader is again referred to [5][6] and [8] for further details.

To avoid solving Equation (41) for every member of the sequence r_i, c_α is obtained only once, for r_0. The same c_α is then used for the rest of the procedure. If better bounds are needed, Equation (41) can be solved for each member of the sequence.

In the case of Equations (11) and (37), any value of c_β used in (40) will produce an upper bound of the solution of Equation (11). For simplicity, $c_\beta = c_\alpha$ was used in the calculations. Finally, the evaluation of an upper bound for $p_i(\eta,0)$ and $\frac{\partial p_i}{\partial \tau}(\eta,0)$ can be done using a regular perturbation solution, as shown in Appendix 3.

In the case of convex functions ($F''(c) < 0$) the above sequence of calculations can be used in much the same way. The only major difference is the definition of the functions F_h and F_g, which are simply interchanged. (see [5]).

Selected results for the case $F(c)=c^2$ are given in Table 3. The same comments as those made for the linear case are applicable here. Additionally, nonlinearities increase the distance between bounds. Still, for moderate values of the Thiele modulus, the method produces good results. If improvements are desired, dividing $F_g(c)$ into two linear pieces is recommended before $H_p(Z_i)$ or $H_r(Y_i)$ are modified. The error then is expected to be comparable to that obtained for the linear case.

CONCLUSIONS

A method has been developed to obtain useful bounding sequences of solutions for a wide class of gas-solid reaction rate expressions. As shown in the applications of the method, convergence to upper and lower bounds are obtained in only a few iterations. For moderate values of the Thiele modulus, the difference between these bounds is small. An approximate solution that lies between the two bounds was also derived. Various extensions of the method to obtain improved accuracy were suggested.

ACKNOWLEDGMENTS

The author wishes to thank the Argentine National Research Council (CONICET) and Universidad Nacional del Litoral (UNL), Santa Fe, Argentina, for their financial support. Also, the valuable comments and suggestions made by Dr. G. R. Gavalas at Caltech are gratefully acknowledged.

REFERENCES

1. Ramachandran P.A., *Chem. Engng Sci.*, 1983, **38**, 1385.
2. Dudukovic M.P., *A.I.Ch.E. Journal.*, 1976, **22**, 945. 22, 945.
3. Del Borghi M., Dunn J.C. and Bischoff K.B., *Chem. Engng Sci.*, 1976, **31**, 1065.
4. Ramachandran P.A. and Doraiswamy L.K., *A.I.Ch.E. Journal*, 1982, **28**, 6, 881.
5. Varma A. and Strieder W. , *IMA. J. of Appl. Math.*, 1985, **34**, 165.
6. Amann H. , *Indiana Univ. Math. J.*, 1971, **21**, 2, 125.
7. Cohen D.S., *SIAM J. Appl. Math.*, 1971, **20**, 1, 1.
8. Sattinger D.H. *Indiana Univ. Math. J.*, 1972, **21**, 11, 979.
9. Dudukovic M.P. and Lamba P.S., *Chem. Engng Sci.*, 1976, **31**, 1065.
10. Avrami M., *J. Chem. Phys.*, 1941, **9**, 177.
11. Bhatia S.K. and Perlmutter D.D., *A.I.Ch.E. Journal*, 1981, **27**, 2.
12. Calvelo A. and Smith J.M. *CHEMECA '70, Proc. 3rd Conf.*, 1970, **1**.
13. Ramachandran P.A. and Smith J.M. *Chem. Engng Sci.*, 1977, **14**, 137.

TABLE 1

Rate Forms for G(X) for Various Gas-Solid Reaction Models

Reaction Model	G(X)
Power Law Model [9]	$(1 - X)^n$
Nucleation Model [10]	$\frac{n(1-X)}{\ln(\frac{1}{1-X})^{1/n-1}}$
Random Pore Model [11]	$\frac{(1-X)\left\{1-\psi \ln(1-X)\right\}^{1/2}}{1 + (\beta' Z_v/\psi)\left\{1-\psi \ln(1-X)\right\}^{1/2}}$
Grain Model [12] [13]	$\frac{(1-X)^{2/3}}{1 + \frac{(1-X)^{1/3}}{Bi}\left[1 - \frac{(1-X)^{1/3}}{\{Z_v + (1-Z_v)(1-X)\}^{1/3}}\right]}$

TABLE 2

Gas Concentration and Solid Conversion (at $\eta = 0$)
for Selected Values of Time, Thiele Modulus, and different Models.
Linear Gas kinetics (F(c)=c).

Random Pore Model: $\psi = 2 \quad \beta' Z_v = 1.8 \quad \gamma = \infty$
$(\Delta_R = 0. \quad \Delta_P = 0. \quad \Delta_P^0 = \infty)$

ϕ	τ	$\tilde{c}_2(0,\tau)$	$\bar{c}_2(0,\tau)$	$\tilde{X}_2(0,\tau)$	$\overline{X}_2(0,\tau)$
1.	0.5	0.900	0.900± .001	0.359	0.359± .008
1.	1.0	0.937	0.936± .002	0.601	0.601± .018
1.	3.0	0.976	0.976± .001	0.850	0.849± .020
2.	0.5	0.656	0.649± .012	0.268	0.264± .021
2.	1.0	0.753	0.745± .022	0.495	0.487± .057

Grain Model: $Bi = 1 \quad Z_v = 1 \quad \gamma = \infty$
$(\Delta_R = 0. \quad \Delta_P = 0. \quad \Delta_P^0 = \infty)$

ϕ	τ	$\tilde{c}_2(0,\tau)$	$\bar{c}_2(0,\tau)$	$\tilde{X}_2(0,\tau)$	$\overline{X}_2(0,\tau)$
1.	0.5	0.899	0.899± .001	0.358	0.358± .008
1.	1.0	0.932	0.931± .002	0.608	0.608± .018
1.	2.0	0.973	0.972± .002	0.889	0.888± .023

$(\Delta_R = \Delta_{r_{max}} \quad \Delta_P = 0. \quad \Delta_P^0 = \Delta_{P_{min}}^0)$

ϕ	τ	$\tilde{c}_2(0,\tau)$	$\bar{c}_2(0,\tau)$	$\tilde{X}_3(0,\tau)$	$\overline{X}_3(0,\tau)$
2.	1.0	0.739	0.729± .011	0.484	0.486± .008
2.	2.0	0.870	0.863± .015	0.797	0.807± .017

TABLE 3

Gas Concentration and Solid Conversion (at $\eta = 0$)
for Selected Values of Time, Thiele Modulus, and different Models.
Second Order Gas kinetics ($F(c) = c^2$).

Grain Model: Bi = 1 $Z_v = 1$ $\gamma = \infty$
($\Delta_R = 0.$ $\Delta_P = 0.$ $\Delta_P^0 = \infty$)

ϕ	τ	$\tilde{c}_2(0,\tau)$	$\bar{c}_2(0,\tau)$	$\tilde{X}_2(0,\tau)$	$\overline{X}_2(0,\tau)$
1.	0.5	0.899	0.897± .002	0.336	0.336± .012
1.	1.0	0.929	0.927± .004	0.596	0.595± .033
1.	2.0	0.974	0.973± .005	0.901	0.896± .041
0.9	0.5	0.926	0.925± .002	0.326	0.326± .012
0.9	1.0	0.949	0.948± .002	0.552	0.552± .026
0.9	2.0	0.975	0.975± .002	0.826	0.824± .036
0.9	3.0	0.990	0.990± .002	0.956	0.951± .026

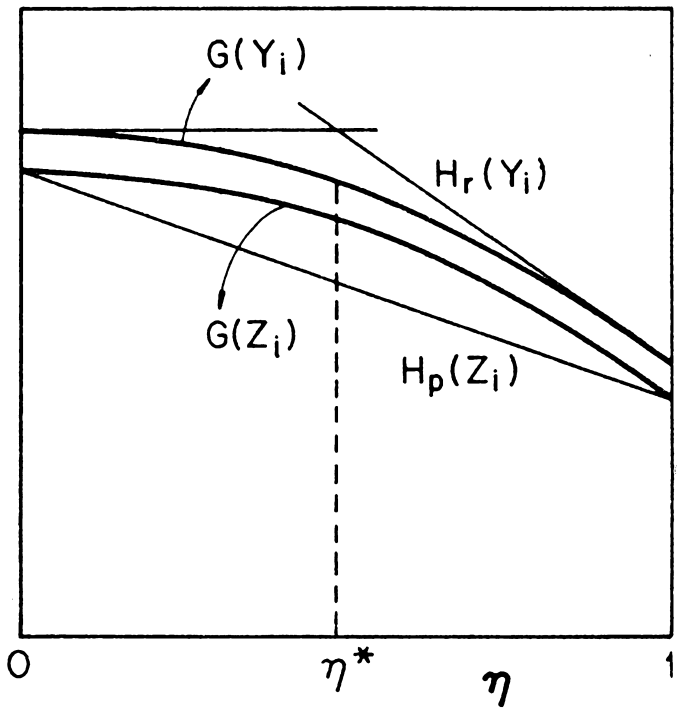

Figure 1: Plot of $G[X(\eta,\tau)]$ and the Proposed Approximating Functions H_p and H_r.

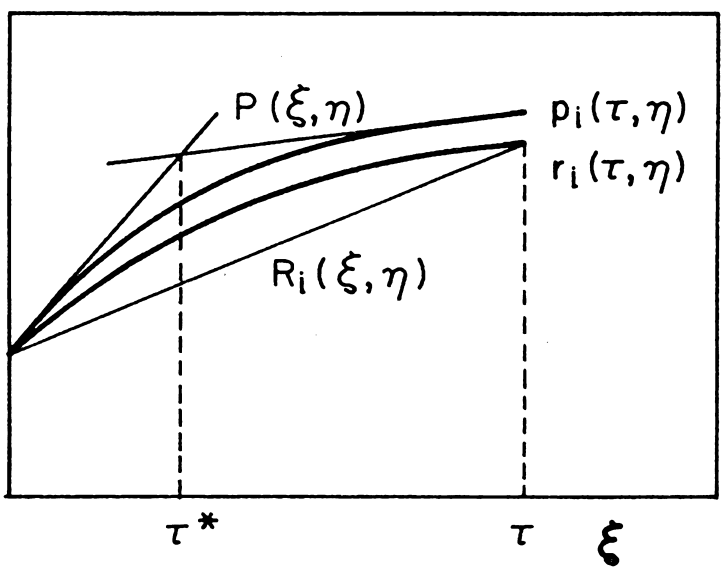

Figure 2: Plot of $p(\eta,\tau)$ and $r(\eta,\tau)$ and the Proposed Approximating Functions $P(\eta,\xi)$ and $R(\eta,\xi)$.

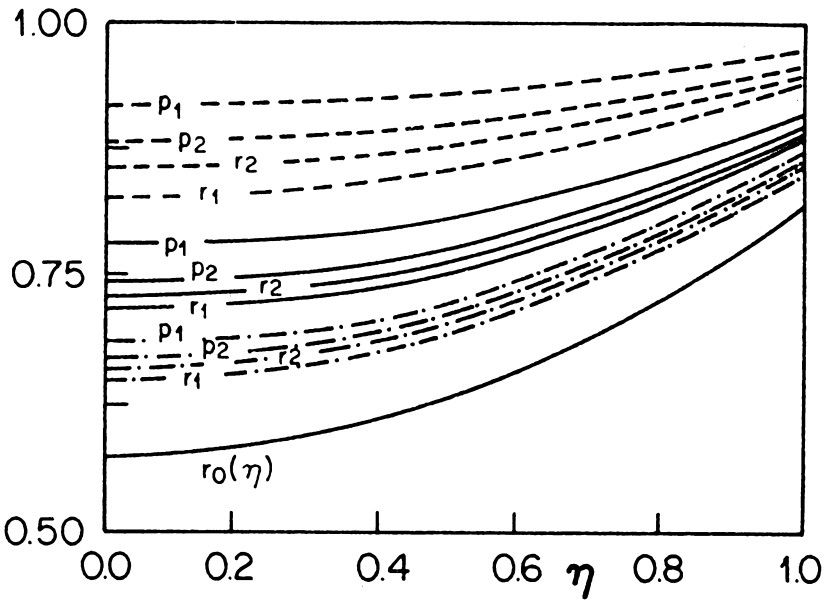

Figure 3: Sequences of Upper and Lower Bounds of the Gas Concentration Profiles. Grain Model.

(ϕ = 1.5; Bi = 2.; γ = 3.0; ·····- τ = 0.5; ——— τ = 1.0; ----- τ = 2.0).

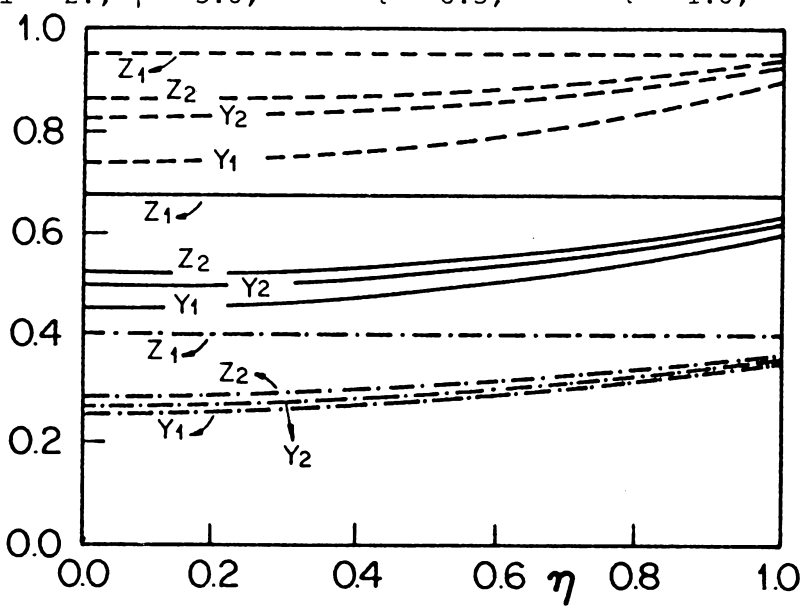

Figure 4: Sequences of Upper and Lower Bounds of the Solid Conversion Profiles. Grain Model.

(ϕ = 1.5, Bi = 2., γ = 3.0; ·····- τ = 0.5, ——— τ = 1.0, ----- τ = 2.0)

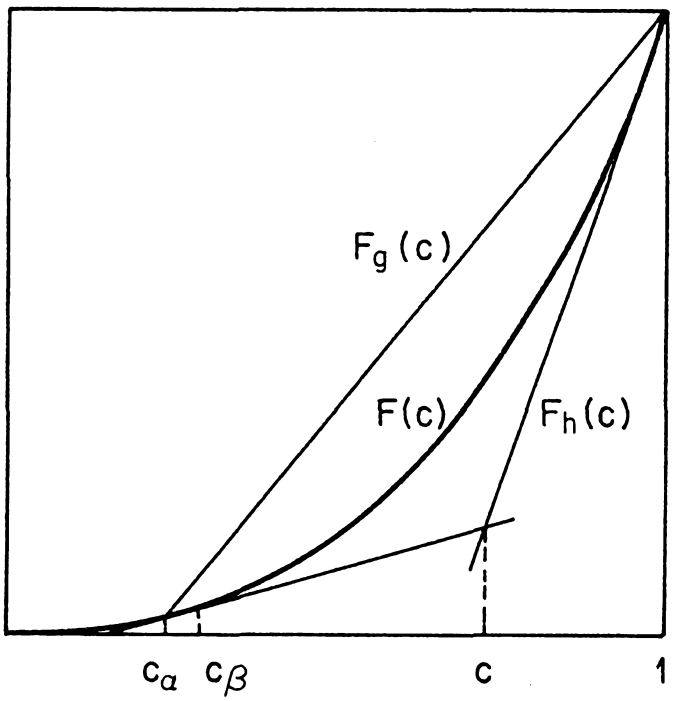

Figure 5: Approximating Functions $F_g(c)$ and $F_h(c)$.

Appendix 1

In this appendix the proof of the Bounding Theorem is given. First, a lemma presented by D.S Cohen is reproduced. Subsequently, two Lemmas needed in the proof of the Bounding Theorem, are presented. Finally, the proof itself is given.

* *Positivity Lemma* (D. S. Cohen [7])

For $\epsilon > 0$, *if*

$$(\nabla^2 - \epsilon)p \geq 0$$

with homogenous linear boundary conditions $Bp = \underline{0}$, *then*

$$p \leq 0$$

Proof: Construct the Green function and note that it is negative. Q.E.D.

To help in the proof of the next lemmas, define the transformation:

$$T\begin{bmatrix} c \\ X \end{bmatrix} = \begin{bmatrix} \hat{c} \\ \hat{X} \end{bmatrix}$$

by means of the following coupled differential equations:

$$(\nabla^2 - \phi^2\Omega)\hat{c} = F(c)\phi^2[G(X) - \Omega]$$

$$\frac{\partial K(\hat{X})}{\partial \tau} = F(c)$$

with boundary conditions as in (3)(4) and (5), and $\Omega = \max G(X)$.

The following lemma provides the basis for the proof of the Bounding Theorem:

* *Lemma 1*

Given $G'(X) \leq 0$ *and* $F'(c) \geq 0$

$$\begin{cases} c_1 \geq c_2 \\ X_1 \geq X_2 \end{cases} \Longrightarrow \begin{cases} \hat{c}_1 \geq \hat{c}_2 \\ \hat{X}_1 \geq \hat{X}_2 \end{cases}$$

Proof:

$$(\nabla^2 - \Omega\phi^2)(\hat{c}_1 - \hat{c}_2) = \left\{F(c_1)G(X_1) - F(c_2)G(X_2) - \Omega\ [F(c_1) - F(c_2)]\right\}\phi^2 =$$

$$= \left\{G(X_1)\left[F(c_1) - \frac{G(X_2)}{G(X_1)}F(c_2)\right] - \Omega\ [F(c_1) - F(c_2)]\right\}\phi^2 \leq$$

$$\leq [G(X_1) - \Omega]\ [F(c_1) - F(c_2)]\phi^2 \leq 0$$

Therefore, by Positivity Lemma we have : $\hat{c}_1 - \hat{c}_2 \geq 0$. *Also:*

$$\frac{\partial}{\partial\tau}[K(\hat{X}_1) - K(\hat{X}_2)] = F(c_1) - F(c_2) \geq 0$$

Integrating and taking into account that $K(0) = 0$, *we have* $K(\hat{X}_1) - K(\hat{X}_2) > 0$. *By definition* $K'(X) = 1/G(X) \geq 0$. *Therefore,* $\hat{X}_1 \geq \hat{X}_2$ *Q.E.D.*

Having proved Lemma 1, in Lemma 2 it will be proved that a sequence of functions constructed using the transformation defined above will be monotone nonincreasing or monotone nondecreasing if certain inequalities are satisfied by the first members of the sequence.

* *Lemma 2*

The sequence $\{c_i, X_i\}$ *defined by*

$$T\begin{bmatrix} c_{i-1} \\ X_{i-1} \end{bmatrix} = \begin{bmatrix} c_i \\ X_i \end{bmatrix}$$

is monotone nonincreasing if:

$$\begin{cases} \nabla^2 c_0 - \phi^2 G(X_0)F(c_0) \leq 0 \\ \dfrac{\partial K(X_0)}{\partial\tau} \geq F(c_0) \end{cases}$$

Proof: The proof will use induction

$$(\nabla^2 - \Omega\phi^2)c_1 = \phi^2 F(c_0)[G(X_0) - \Omega]$$

$$\Longrightarrow (\nabla^2 - \Omega\phi^2)(c_1 - c_0) = \phi^2[F(c_0)G(X_0) - \nabla^2 c_0] \geq 0$$

Therefore, by Positivity Lemma: $c_1 \leq c_0$. *Also:*

$$\frac{\partial K(X_1)}{\partial\tau} = F(c_0) \Longrightarrow \frac{\partial K(X_1)}{\partial\tau} - \frac{\partial K(X_0)}{\partial\tau} = F(c_0) - \frac{\partial K(X_0)}{\partial\tau} \leq 0$$

Using $K(0)=0$ *and* $K'(X) \geq 0$, *we get* $X_1 \leq X_0$

Once established the above inequalities use Lemma 1 to write

$$\left.\begin{aligned} c_{i-1} &\le c_{i-2} \\ X_{i-1} &\le X_{i-2} \end{aligned}\right\} \Longrightarrow \left\{\begin{aligned} c_i &\le c_{i-1} \\ X_i &\le X_{i-1} \end{aligned}\right.$$

Q.E.D.

Corollary: Invert the inequalities to prove that similar monotone nondecreasing sequence exist.

The above lemmas can now be used to prove the Bounding Theorem.

* *Proof of the Bounding Theorem*

Consider the pairs (s_0, V_0) *and* (u_0, W_0) *to be the first elements of two sequences obtained by successive application of the transformation T.*

If $s_0 \le u_0$ *and* $V_0 \le W_0$, *lemmas 1 and 2 allow to write:*

$$\left.\begin{aligned} u_i &\ge s_j \\ W_i &\ge V_j \end{aligned}\right\} \forall i\ ,\ \forall j$$

The fact that the above inequalities hold together with the monotone nonincreasing and nondecreasing property of the sequences prove that those sequences converge to the pairs (s_∞, V_∞) *and* (u_∞, W_∞), *which will satisfy:*

$$\nabla^2 u_\infty - \phi^2 G(W_\infty) F(u_\infty) = 0 \qquad \nabla^2 s_\infty - \phi^2 G(V_\infty) F(s_\infty) = 0$$

$$\frac{\partial K(W_\infty)}{\partial \tau} = F(u_\infty) \qquad \frac{\partial K(V_\infty)}{\partial \tau} = F(s_\infty)$$

which are clearly solutions of Equations (7) and (8). In the case that the system of Equations (7) and (8) has a unique solution, then:

$$u_\infty = s_\infty = c$$

$$W_\infty = V_\infty = X$$

otherwise, sequences converge to two different solutions. Q.E.D.

Appendix 2

In this appendix it is proved that the proposed sequence of approximate solutions $\{\tilde{c}_i, \tilde{X}_i\}$ lies in between the sequence of upper and lower bounds given by (11) through (14).

The proof will be based on the following lemma:

* *Comparison Lemma*

Given

$$\nabla^2 c_1 - f_1(\eta)F(c_1) = 0$$

$$\nabla^2 c_2 - f_2(\eta)F(c_2) = 0$$

with linear boundary conditions $Bc_1 = Bc_2 = \underline{g}$.

If $f_2(\eta) \geq f_1(\eta)$, *then* $c_1 \geq c_2$

Proof: Substract the equations and use $f_2(\eta) \geq f_1(\eta)$ *to write:*

$$\nabla^2(c_1 - c_2) - f_1(\eta)[F(c_1) - F(c_2)] \leq 0$$

$$B(c_1 - c_2) = 0$$

Also,

$$F(c) = F(c_1) + \lambda(c - c_1)$$

where λ *is the slope of the secant passing through both points. For* $F'(c) > 0$ *it is easy to see that* $\lambda > 0$. *Therefore, taking* $\Lambda = \max \lambda$ *and* $\Omega = \max \{f_1(\text{eta})\}$:

$$\nabla^2(c_1 - c_2) - \Omega\Lambda(c_1 - c_2) \leq 0$$

with homogeneous boundary condition $B(c_1 - c_2) = \underline{0}$.

Use Positivity Lemma to conclude that $c_1 \geq c_2$. *Q.E.D.*

Induction will now be used to show that $r_i(\eta, \tau) \leq \tilde{c}_i(\eta, \tau) \leq p_i(\eta, \tau)$.

In general, if $r_{i-1}(\eta, \tau) \leq \tilde{c}_{i-1}(\eta, \tau) \leq p_{i-1}(\eta, \tau)$, then $K(Y_i) \leq K(\tilde{X}_i) \leq K(Z_i)$. Since $K'(X) > 0$,

$$H_r(Y_i) \geq H_p(\tilde{X}_i) \geq H_p(Z_i)$$

Now use Comparison Lemma to conclude that $\tilde{c}_i(\eta, \tau)$ lies in between the upper and the lower bounds.

To complete the induction proof note that $\tilde{X}_0 = Z_0$. This in turn will give $\tilde{c}_0 = p_0$. Continuing the sequence one obtains $K(Y_1) \leq K(\tilde{X}_1) \leq K(Z_0)$ and, as before, using the Comparison Lemma one obtains $r_1(\eta, \tau) \leq \tilde{c}_1(\text{eta}, \tau) \leq p_1(\eta, \tau)$. *Q.E.D.*

Appendix 3

In this appendix a regular perturbation expansion is proposed to obtain expressions for $p_i(\eta, 0)$ and $\frac{\partial p_i}{\partial \tau}(\eta, 0)$. As $\tau \to 0$, $\alpha_p \to 1$ and $\beta_p \to 0$. This suggests the following expansion:

$$p_i(\eta, \tau) = p_{i,0}(\eta, \tau) + p_{i,1}(\eta, \tau)\beta_p + p_{i,2}(\eta, \tau)\beta_p^2 + \dots$$

Also,

$$F(p_i) = F(p_{i,0}) + O(\beta_p)$$

Substitute in Equation (10) for the case F(c)=c and solve the zero order approximation to get:

$$p_{i,0}(\eta, 0) = r_0(\eta) = a_r \frac{\sinh(\phi\eta)}{\eta}$$

In order to get $\frac{\partial p_i}{\partial \tau}(\eta, 0)$ let

$$\frac{\partial p_i}{\partial \tau}(\eta, \tau) = z_0(\eta, \tau) + z_1(\eta, \tau)\beta_p + z_2(\eta, \tau)\beta_p^2 + \dots$$

By differentiating (11) with respect to time, one gets:

$$\nabla^2 \frac{\partial p_i}{\partial \tau} - \phi^2(\alpha_p - \beta_p\eta)F'(p_i)\frac{\partial p_i}{\partial \tau} = \phi^2\left(\frac{\partial \alpha_p}{\partial \tau} - \frac{\partial \beta_p}{\partial \tau}\eta\right)F(p_i)$$

For F(c)=c, substituting the regular expansions proposed and solving the zero-order equation, one obtains

$$\frac{\partial p_i}{\partial \tau}(\eta, 0) = z_0(\eta, 0)$$

For the case of non-linear gas kinetics, upper-bounds for both $p_i(\eta, 0)$ and $\frac{\partial p_i}{\partial \tau}(\eta, 0)$ can be easily obtained using the approach suggested by Varma and Strieder [5].

An upper bound $\hat{p}_i(\eta, 0)$ can be found solving:

$$\nabla^2 \hat{p}_i - \phi^2 F_{li}(\hat{p}_i) = 0$$

$$B\hat{p}_i = \underline{0}$$

Finally, since in general

$$F_{li}(c) = a_1 + a_2 c$$

the value of $\frac{\partial \hat{p}_i}{\partial \tau}$ is obtained solving

$$\nabla^2 \frac{\partial \hat{p}_i}{\partial \tau} - \phi^2 (\alpha_p - \beta_p\eta)a_2 \frac{\partial \hat{p}_i}{\partial \tau} = \phi^2 \left(\frac{\partial \alpha_p a_1}{\partial \tau} - \frac{\partial \beta_p a_1}{\partial \tau}\right) + \left(\frac{\partial \alpha_p a_2}{\partial \tau} - \frac{\partial \beta_p a_2}{\partial \tau}\right)\hat{p}_i$$

$$B\left[\frac{\partial \hat{p}_i}{\partial \tau}\right] = \underline{0}$$

As in the linear case, propose a perturbation expansion in terms of β_p, substitute in the above equation, and solve. The zero order solution will be the value of $\frac{\partial p_i}{\partial \tau}(\eta, 0)$. *Q.E.D.*

CHAPTER IX

Libertad es el derecho que todo hombre tiene a ser honrado, y a pensar y a hablar sin hipocresía... Un hombre que oculta lo que piensa, o no se atreve a decir lo que piensa, no es un hombre honrado. Un hombre que obedece a un mal gobierno, sin trabajar para que el gobierno sea bueno, no es un hombre honrado. Un hombre que se conforma con obedecer leyes injustas y permite que pisen el país en que nació los hombres que lo maltratan, no es un hombre honrado.

José Martí.

This chapter will be submitted to the Journal *Chemical Engineering Journal.* Analytical approximate solutions are proposed to determine the temperature and concentration profiles for a single gas-solid reaction inside a fixed-bed reactor. The method is used to analize favorable conditions for the occurrance of sulfate formation during ZnS oxidation in a fixed-bed reactor.

PROPAGATION OF REACTION FRONTS IN EXOTHERMIC GAS-SOLID FIXED BED REACTORS

Miguel J. Bagajewicz* and George R. Gavalas

California Institute of Technology
Pasadena, CA 91125

* Now at INTEC, CC No 98, 3000 Santa Fe, Argentina

ABSTRACT

Traveling wave solutions are used to analyze the reaction front that develops in a gas-solid reaction carried out in a fixed-bed reactor. Simple functions are proposed to approximate the temperature and concentration profiles. For adiabatic operation and/or fast kinetics, analytical solutions are obtained in terms of a transformed dependent variable. The method is illustrated analyzing the oxidation of ZnS in a fixed-bed reactor.

INTRODUCTION

Many industrial processes employ fixed or moving bed reactors, where a gas-solid reaction having significant heat effects takes place. Processes such as mineral roasting, coal gasification, iron oxide reduction, etc, are pertinent examples. Prediction of temperature and concentration profiles developing inside reactors is often necessary to avoid undesired situations like solid overheating or runaway, secondary reactions and/or changes in selectivity.

Various numerical approaches have been used to solve the governing energy and species conservation equations [1-10]. One approach was to describe the bed as a one- or two-dimensional array of completely mixed elements [1-4]. Another approach was to reduce the governing partial differential equations to a set of ordinary differential equations, either by the method of characteristics [5], or by orthogonal collocation [6], with further numerical integration. Other formulations that include detailed intraparticle description have been solved numerically [8-9]. A general numerical algorithm accounting for intraparticle reaction and diffusion was published by Sampath *et al.*[10].

Notwithstanding the generality of the numerical approach, analytical solutions of the reactor equations, even under restrictive assumptions, would be desirable to investigate, in a direct and simple fashion, the effect of various parameters on system behaviour. Van Deemter [11-12] presented a simplified model in which a zero-order reaction was considered together with the usual assumptions that allow a one-dimensional treatment of the problem. First-order reaction with respect to both the solid and the reactant gas is considered by Johnson *et al.* [13]. By assuming that the rate constant is independent of temperature and neglecting the influence of the concentration profiles developed near the reactor inlet at the early stages of the operation, a first-order linear PDE was obtained for the temperature and was integrated analytically using the method of characteristics. When the temperature dependence of the reac-

tion rate is included, analytical solutions cannot anymore be obtained using the same approach. However, Ozawa [14] neglected the accumulation terms for the gas concentration and the temperature and derived analytical solutions in terms of the exponential integral for the case of a reaction rate that is first order with respect to both the gas concentration and the solid conversion.

In a recent paper, Gatica *et al.* [15] studied the propagation of exothermic reaction fronts in catalytic fixed-bed reactors in the context of the creeping phenomena. Some important characteristics, such as the maximum front temperature and the conversion at the hot spot were obtained approximately by means of a similarity transformation or traveling wave solutions. The solution procedure relied on numerical integration in order to find the shape of the reaction front.

In this paper, the general non-adiabatic problem is analyzed and analytical approximate solutions for the temperature and concentration profiles are derived, assuming a traveling wave solution. Special cases, such as the adiabatic reactor or the limit of fast kinetic are also considered. For these cases, simple closed form relations between temperature and gas concentration are obtained using a special transformation of variables. The method is illustrated with the analysis of the oxidation of ZnS in a fixed-bed reactor, where the conditions favoring a secondary reaction forming zinc sulfate are of practical interest. This analysis is of importance, when ZnO is used as a sorbent for hot-gas desulfurization where regeneration is carried out by oxidation of the spent ZnS.

MODEL FORMULATION

Consider the following irreversible gas-solid reaction taking place in a fixed-bed reactor.

$$a\,A_{(g)} + B_{(s)} \longrightarrow c\,C_{(g)} + d\,D_{(s)} \tag{1}$$

The continuity equations for the reactant gas concentration and solid conversion are described in the standard form.

$$\frac{\partial \hat{c}}{\partial t} + u\frac{\partial \hat{c}}{\partial z} = a\rho_s \frac{(1-\epsilon_0)}{\epsilon_0} k(T)\ \hat{F}(\hat{c},T)\ \hat{G}(\hat{X},T) \tag{2}$$

$$\frac{\partial X}{\partial t} = k(T)\ \hat{F}(\hat{c},T)\ \hat{G}(X,T) \tag{3}$$

The rate term is generally expresed as a product of three factors, namely, the rate constant k(T), which contains the principal temperature dependence and has the well-known Arrhenius form, the factor $\hat{F}(\hat{c}, T)$, which depends on temperature and reactant gas concentration, and the solid conversion factor $\hat{G}(X, T)$. Intraparticle diffusion resistances are here neglected.

The energy equation can be written with minor simplifications as follows:

$$[(1-\epsilon_0)\rho_s C_{p_s} + \epsilon_0 \rho_g C_{p_g}]\frac{\partial T}{\partial t} + \epsilon_0 \rho_g C_{p_g} u \frac{\partial T}{\partial z} = a\rho_s(1-\epsilon_0)(-\Delta H)k(T)\,\hat{F}(\hat{c}, T)\,\hat{G}(\hat{X}, T) + Q \qquad (4)$$

where Q represents the heat transferred through the wall of the reactor. In this paper only two cases are analyzed. Either the reactor is adiabatic (Q=0) or the wall temperature is constant. In this last case Q is given by

$$Q = \frac{4U\epsilon_0}{D}(T_w - T) \qquad (5)$$

This one-dimensional pseudohomogeneous model has been –and still is– used for simple reactor simulations.

A few words about the energy equation are appropiate before proceeding into the analytical developement. Note first that the heat transfer resistance between the gas and the solid is neglected. Axial heat and mass dispersion is also neglected, and the gas phase velocity is considered constant. The latter assumption holds well, either when the reaction is equimolar with respect to gas phase reactant and products, or when the mole fraction of reactants and products is small. The gas density and the heat capacities of gas and solid are considered constant and independent on temperature. In the presence of large temperature gradients, the latter assumption and the assumption of neglegible axial heat dispersion will introduce significant error. Finally, for convenience, ΔH is treated as a constant. Its temperature dependence can be incorporated with minor changes in the solution procedure.

The simplifying assumptions seem to constitute a fair tradeoff between accuracy and ability to obtain analytical results.

The following boundary and initial conditions will be used:

$$\hat{c}(0,t) = c_0 \tag{6}$$

$$X(z,0) = 0 \tag{7}$$

Equations (2-4) are made dimensionless by using the following characteristic quantities: The characteristic time is

$$t^* = \frac{1}{c_0 k(T^*)} \tag{8}$$

in which T^* is the characteristic temperature chosen to be the reactor wall temperature (T_w) in the non-adiabatic case and the reactor feed gas temperature T_0 in the adiabatic case. The characteristic length is

$$z^* = \frac{u}{(1+A)} t^* \tag{9}$$

where A is given by

$$A = a \frac{\rho_s}{c_0} \frac{(1-\epsilon_0)}{\epsilon_0} \tag{10}$$

The dimensionless time and position are now defined by

$$x = \frac{z}{z^*} \qquad \tau = \frac{t}{t^*} \tag{11}$$

For the dependent variables the following dimensionless concentration and temperature c and Y are used:

$$c = \frac{\hat{c}}{c_0} \qquad Y = \frac{T - T^*}{T^*} \tag{12}$$

Using the above definitions, the equations for the concentration and temperature assume the dimensionless form

$$\frac{\partial c}{\partial \tau} + (1+A) \frac{\partial c}{\partial x} = A \frac{\partial X}{\partial \tau} \tag{13}$$

$$\frac{\partial X}{\partial \tau} = e^{\gamma \frac{Y}{(1+Y)}} F(c,Y)\, G(X,Y) \tag{14}$$

$$\frac{\partial Y}{\partial \tau} + (1+A)\delta \frac{\partial Y}{\partial x} = B \frac{\partial X}{\partial \tau} - M\, Y \tag{15}$$

where B is the dimensionless heat of reaction

$$B = a\frac{(-\Delta H)}{C_{p_s} T^*} \tag{16}$$

M is the dimensionless heat transfer coefficient

$$M = \frac{4U\epsilon_0}{D\rho_s C_{p_s}(1-\epsilon_0)} \tag{17}$$

and γ is the dimensionless activation energy given by

$$\gamma = \frac{E}{RT^*} \tag{18}$$

Note that $(1-\epsilon_0)\rho_s C_{p_s}$ is much larger than $\epsilon_0 \rho_g C_{p_g}$, so that the latter has been neglected in Equation (15).

SOLUTION PROCEDURE

The above set of equations admits a traveling wave solution for the gas concentration and temperature. Making the change of variables

$$\theta = x - \tau \tag{19}$$

$$\sigma = x \tag{20}$$

the assumption of traveling waves implies that c, X and Y are independent of the variable σ; therefore,

$$\frac{\partial c}{\partial \theta} = \frac{\partial X}{\partial \theta} \tag{21}$$

$$\frac{\partial X}{\partial \theta} = -e^{\gamma \frac{Y}{(1+Y)}} F(c, Y)\, G(X, Y) \tag{22}$$

$$\frac{\partial Y}{\partial \theta} = -s\frac{\partial X}{\partial \theta} - m\, Y \tag{23}$$

Integration of (21) gives at once

$$c(\theta) = X(\theta) \tag{24}$$

The traveling wave solution is strictly valid only for an infinitely long reactor. For a finite reactor it yields a useful approximation only if the thickness of the reaction front is much smaller than the length of the reactor,

$$z^* << L \tag{25}$$

Substitution of (24) in (22) produces two ordinary differential equations in X and Y. Integration of Equations (22) and (23) is complicated by the non-linearity of the rate terms and the infinite extent of the domain of integration. In the next section we present an approximate solution procedure for the non-adiabatic as well as for the adiabatic case. An exact solution for the adiabatic case is presented in a later section.

Note that Equations (21-23) describe the operation of a moving-bed reactor ,at steady-state, provided θ is interpreted as the position. The boundary conditions would be, however, different.

Approximate Solutions

Equations (22) and (23) are integrated formally to get

$$X(\theta) = \int_{\theta}^{\infty} Z(X(\xi), Y(\xi))\, d\xi \tag{26}$$

$$Y(\theta) = se^{-m\theta} \int_{-\infty}^{\theta} e^{m\xi}\, Z(X(\xi), Y(\xi))\, d\xi \tag{27}$$

where the kernel Z(X,Y) is given by

$$Z(X, Y) = e^{\gamma \frac{Y}{(1+Y)}} F(X, Y)\, G(X, Y) \tag{28}$$

One way to obtain approximate solutions is to approximate the kernel Z(X,Y) using some appropiate function. This can be done by exploiting the form of X, which is known to be that of an inverted S-shaped curve typical of these reaction fronts. The kernel Z(X,Y) is precisely the derivative of this S-shaped curve, therefore, it has the form of an asymmetric bell-shaped curve.

Based on this fact, it is here proposed that an approximate solution $\{\tilde{X}, \tilde{Y}\}$ of the system of integral Equations (26-27) is obtained as a limit of the following iterative procedure:

$$\tilde{X}_{i+1}(\theta) = \int_{\theta}^{\infty} R_i(\xi)\, d\xi \tag{29}$$

$$\tilde{Y}_{i+1}(\theta) = se^{-m\theta} \int_{-\infty}^{\theta} e^{m\xi}\, R_i(\xi)\, d\xi \tag{30}$$

where $R_i(\theta)$ is a function that approximates the curve given by $Z(\tilde{X}_i(\theta), \tilde{Y}_i(\theta))$ as defined below. Even when the iterative process converges, however, the distance between R_∞ and $Z(\tilde{X}_\infty, \tilde{Y}_\infty)$ cannot be made arbitrarily small, because R_i has been constrained to a specific functional form.

The approximating function used in our calculations is defined by: (see Figure 1)

$$R_i(\xi) = \begin{cases} a_{1_i}\, e^{\nu_1 \xi} & \xi < \theta_1 \\ Z_{0_i}\, e^{-B_{1_i}(\xi-\theta_{0_i})^2} & \theta_1 \le \xi < \theta_{0_i} \\ Z_{0_i}\, e^{-B_{2_i}(\xi-\theta_{0_i})^2} & \theta_{0_i} \le \xi < \theta_2 \\ a_{2_i}\, e^{-\nu_2 \xi} & \xi \ge \theta_2 \end{cases} \tag{31}$$

where the various parameters are defined by the following conditions:

i.- Continuity at θ_1 and θ_2. This automatically permits writing a_{1_i} and a_{2_i} in terms of the other parameters.

ii.- According to (31), the maximum of R_i is attained at θ_{0_i}. This point is chosen to coincide with the position of the maximum of $Z(\tilde{X}_i(\theta), \tilde{Y}_i(\theta))$.

iii.- The parameter Z_{0_i} is equal to $Z(\tilde{X}_i(\theta_{0_i}), \tilde{Y}_i(\theta_{0_i}))$.

iv.- The condition $\tilde{X}_{i+1}(0) = 0.5$ is introduced to define the "center" of the wave. This condition is used to calculate B_{2_i}.

v.- To meet the boundary conditions, B_{1_i} is selected to satisfy $\tilde{X}_{i+1}(-\infty) = 1$.

vi.- The asymptotic behavior of the solutions for large positive and negative values of θ are used as a guideline to obtain values of ν_1 and ν_2. The functions X and Y approach zero at ∞. Therefore, F(X,Y) and G(X,Y) approach unity. Thus:

$$Z(X, Y) \longrightarrow 1 \qquad \text{as } \theta \longrightarrow \infty \tag{32}$$

Similarly, for large negative θ, X approaches unity and Y approaches zero; therefore, F(X,Y) approaches unity. The asymptotic behaviour of G(X,Y) depends on the particular model used. For example, if the random pore model [16] is used,

$$G(X, Y) = \frac{(1-X)\{1-\psi \ln(1-X)\}^{1/2}}{1+\omega e^{-\gamma \frac{1}{1+Y}}\{1-\psi \ln(1-X)\}^{1/2}} \longrightarrow \frac{(1-X)}{\omega} \tag{33}$$

as $X \longrightarrow 0$. Therefore, in all cases a good choice for ν_2 is $\nu_2 = 1$. On the other hand ν_1 can be selected for each particular case to make $R_i(\xi)$ have

the same asymptotic behavior as Z(X,Y) for $X \longrightarrow 1$. It may be added that for some rate expressions X will not approach unity exponentially for large negative values of θ, as it was assumed. In some other cases it is not possible to deduce the asymptotic behavior for $X \longrightarrow 1$. In such cases ν_1 has to be selected in some other way, if (31) is to be used.

Once the values of ν_1 and ν_2 are chosen, the values of B_{1_i} and B_{2_i} are affected only by the iterated values of Z_{0_i} and θ_{0_i}. This may affect the distance between R_∞ and $Z(\tilde{X}_\infty, \tilde{Y}_\infty)$. If this distance is found to be too large, the parameters ν_1 and ν_2 can be changed to obtain better results.

With the above choice of parameters, $\tilde{X}_{i+1}(\theta)$ is obtained in terms of the error function:

$$\tilde{X}_{i+1}(\theta) = \begin{cases} \tilde{X}_{i+1}(\theta_1) + \frac{a_{1_i}}{\nu_1}(e^{\nu_1\theta_1} - e^{\nu_1\theta}) & \theta < \theta_1 \\ \tilde{X}_{i+1}(\theta_{0_i}) + N(B_1, \theta) & \theta_1 \le \theta < \theta_{0_i} \\ \tilde{X}_{i+1}(\theta_2) + N(B_2, \theta_2) - N(B_2, \theta) & \theta_{0_i} \le \theta < \theta_2 \\ \frac{a_{2_i}}{\nu_2} e^{-\nu_2\theta} & \theta \ge \theta_2 \end{cases} \tag{34}$$

where

$$N(B, \theta) = \frac{Z_{0_i}}{2}\sqrt{\frac{\pi}{B}}\,\mathrm{erf}\left(\sqrt{B}(\theta_{0_i} - \theta)\right) \tag{35}$$

Similarly $\tilde{Y}_{i+1}(\theta)$ is given by:

$$\tilde{Y}_{i+1}(\theta) = s\, e^{-m\theta} I(\theta) \tag{36}$$

where

$$I(\theta) = \begin{cases} \frac{a_{1_i}}{m+\nu_1} e^{(m+\nu_1)\theta} & \theta \le \theta_1 \\ I(\theta_1) + J_1(B_{1_i}, \theta) & \theta_1 < \theta \le \theta_{0_i} \\ I(\theta_{0_i}) + \left[J_1(B_{1_i}, \theta_{0_i}) + J_2(B_{2_i}, \theta)\right] & \theta_{0_i} < \theta \le \theta_2 \\ I(\theta_2) + \frac{a_{2_i}}{(m-\nu_2)}\{e^{(m-\nu_2)\theta} - e^{(m-\nu_2)\theta_2}\} & \theta > \theta_2 \end{cases} \tag{37}$$

$$J_1(B, \theta) = e^{m\theta_{0_i} + \frac{m^2}{4B}} \frac{Z_{0_i}}{2}\sqrt{\frac{\pi}{B}}\left\{\mathrm{erf}\left(\sqrt{B}(\theta_{0_i} - \theta_1) + \frac{m}{2\sqrt{B}}\right) - \right.$$
$$\left. - \mathrm{erf}\left(\sqrt{B}(\theta_{0_i} - \theta) + \frac{m}{2\sqrt{B}}\right)\right\} \tag{38}$$

$$J_2(B, \theta) = e^{m\theta_{0_i} + \frac{m^2}{4B}}\sqrt{\frac{\pi}{B}} \begin{cases} \mathrm{erf}\left(\frac{m}{2\sqrt{B}}\right) - & \\ -\mathrm{erf}\left(\frac{m}{2\sqrt{B}} - \sqrt{B}(\theta - \theta_{0_i})\right) & \theta - \theta_0 < \frac{m}{2\sqrt{B}} \\ \mathrm{erf}\left(\frac{m}{2\sqrt{B}}\right) + & \\ +\mathrm{erf}\left(\sqrt{B}(\theta - \theta_{0_i}) - \frac{m}{2\sqrt{B}}\right) & \theta - \theta_0 \ge \frac{m}{2\sqrt{B}} \end{cases} \tag{39}$$

To illustrate the application of the method the factor F(c,Y) was chosen to have the Langmuir kinetics and the factor G(X,Y) was selected according to the random pore model. The results are shown in Figure 2.

Large values of γ produce steep reaction fronts, even for low values of the dimensionless heat of reaction. Figure 3 shows the effect of γ. As γ increases, Z(X,Y) becomes steeper and narrower. This causes numerical problems in the determination of the values of B_{1_i} and B_{2_i}. Therefore, the case of large γ is handled by a different approach, as shown in the next section. The present analysis also fails in the case of very large s, when large temperature gradients develop, undermining the assumption of neglegible axial heat conduction.

Exact Solutions for the Adiabatic and/or Fast Kinetic Cases

When analyzing the adiabatic case note first that integration of (23) gives

$$Y(\theta) = s[1 - X(\theta)] \tag{40}$$

Substitution of (40) and (24) into (22) provides a single ordinary differential equation:

$$\frac{\partial X}{\partial \theta} = -Z(X, s[1 - X]) \tag{41}$$

Equation (41) is usually not integrable in closed form. For moderate values of γ, the approximate solutions of the previous section can be used to solve (41) in terms of θ. In the general case, some results can be obtained introducing a new variable λ such that:

$$\frac{d\lambda}{d\theta} = \begin{cases} e^{\gamma \frac{Y}{1+Y}} F(X,Y)\, G(X,Y)/(1-X) & \theta < 0 \\ e^{\gamma \frac{Y}{1+Y}} F(X,Y)\, G(X,Y)/X & \theta \geq 0 \end{cases} \tag{42}$$

with $\lambda(0) = 0$. Equations (22) and (23) become:

$$\frac{\partial X}{\partial \lambda} = \begin{cases} -(1-X) & \theta < 0 \\ -X & \theta > 0 \end{cases} \tag{43}$$

$$\frac{\partial Y}{\partial \lambda} + m\frac{d\theta}{d\lambda}Y = -s\frac{\partial X}{\partial \lambda} \tag{44}$$

When γ is large, a steep front will develop and the change of variables from θ to λ constitutes a coordinate stretching. In that case, all mass transfer, chemical reactions and heat generation take place in a very thin region of the reactor with the center at $\theta = 0$. Heat transfer to the wall is limited inside this region, and therefore the reaction region is effectively adiabatic. As shown schematically in Figure 4, the temperature gradually declines outside the reaction region, because of heat transfer to the reactor wall. The value of $\frac{d\theta}{d\lambda}$ is small inside the reaction region and Equation (44) can be simplified by neglecting the heat transfer to the wall. Integration of the simplified equation gives (40).

Outside the reaction region, $X(\theta) \approx 0$, and the problem is one of pure heat transfer, yielding

$$Y(\theta) = \begin{cases} 0 & \theta < 0 \\ s\, e^{-m\theta} & \theta \geq 0 \end{cases} \tag{45}$$

while integration of (43) gives

$$X(\lambda) = \begin{cases} 1 - \frac{1}{2}e^{\lambda} & \theta < 0 \\ \frac{1}{2}e^{-\lambda} & \theta \geq 0 \end{cases} \tag{46}$$

Equations (43),(44) do not generally admit an analytical solution for X and Y as functions of λ. However, useful information can still be obtained when comparing values of X and Y at the same position λ. An example of this type of analysis is given in the next section.

In using a traveling wave approach to describe the temperature profile, the effect of the initial conditions has been neglected. To see how this affects the analysis, consider a finite adiabatic reactor. In Figure 5, a schematic representation of the expected concentration and thermal profile is shown for the adiabatic case. For short times, the heat generated at the reaction front is not sufficcient to heat up the rest of the solid downstream the front. As time increases, the front advances and the temperature downstream of the front approaches asymptotically the traveling wave limit. Numerical solutions obtained by Liaw *et al.* [9] are a good example of this asymptotic behaviour.

For the traveling wave to be a good approximation of the solution, the heat generated near the reactor inlet at the begining of the operation must be sufficient to heat up the bed of solids downstream of the reaction front to a

temperature close to the asymptotic limit. Assuming that all the heat generated by the reaction, after the thermal wave has traveled a distance L_T, is used to heat up the bed to its final temperature, we have by a simple heat balance

$$\frac{L_T}{L} = \frac{C_{p_s} T_0}{a(-\Delta H)} s \tag{47}$$

Now, the traveling wave will be a good approximation if $L_T/L \ll 1$. Substituting for s, one obtains the following criterion for the adiabatic case and the case of relatively slow kinetics.

$$\frac{L_T}{L} = \frac{1}{(1+A)\delta - 1} << 1 \tag{48}$$

In the case of large values of γ, the steep reaction front that develops is effectively adiabatic, and the above criterion is not needed, since the solution outside the front is given by (45).

Application to ZnS Oxidation in a Fixed-Bed

Zinc oxide and zinc ferrite are being studied [17-21] as sorbents for high-temperature removal of H_2S from coal-generated fuel gas. This desulfurization operation is conducted in fixed-bed reactors and, when the sorbent is completely sulfided, it is regenerated by oxidation with diluted air. The ZnS oxidation reaction is

$$ZnS + \frac{3}{2}O_2 \longrightarrow ZnO + SO_2 \tag{49}$$

Regeneration of a high-surface area sorbent at temperatures ranging from 900 to 1000°K was reported in [21]. The oxidation rate was found to follow a Langmuir type expression:

$$\hat{F}(\hat{c}, T) = k(T)\frac{\hat{c}}{1 + k'(T)\hat{c}} \tag{50}$$

For the temperature range of these studies γ is approximately 5.

For the dimensions of the experimental reactor described in [21], and for the properties of the ZnO prepared as described in [20], we obtain $L_T/L \leq 0.11$ and $z^* = 3. \times 10^{-4}$cm, satisfying the conditions of validity of the traveling wave solution. During the regeneration process it is essential that the structural

properties of the sorbent are preserved. Therefore, predictions of the maximum temperature obtained inside the bed are important to prevent the sorbent from sintering.

Besides the sintering problem, another potential pitfall is a secondary reaction forming zinc sulfate:

$$ZnO + \frac{1}{2}O_2 + SO_2 \longrightarrow ZnSO_4 \tag{51}$$

Zinc sulfate cannot be easily eliminated because it decomposes very slowly at desulfurization temperatures. Any $ZnSO_4$ surviving the regeneration will be rapidly reduced by the fuel gas during sulfidation, producing undesirable SO_2 in the product gas.

Since the oxidation reaction rate is high, a steep front develops and equations (40) and (46) give the concentration and temperature profile inside this region. These, in turn, can be used to determine the thermodynamic threshold for sulfate formation. This reaction is thermodynamically unfavorable when

$$P_{O_2}^{\frac{1}{2}} P_{SO_2} < K(T) \tag{52}$$

where K(T) is the equilibrium constant for reaction (51). Outside of the reaction front, this condition is satisfied. Using the general analytical form for an adiabatic steep reaction front in terms of λ, it is possible to check if (52) can be satisfied inside the region. In Figure 6, selected values of the parameters are used to compare values of $p_{SO_2} p_{O_2}^{1/2}$ and K(T). For low-oxygen concentration there is no favorable thermodynamic condition for sulfate formation. As oxygen concentration increases, a value is reached beyond which inequality (52) is violated. For each value of concentration the temperature at which inequality (52) changes sign was calculated and plotted in Figure 7, together with the corresponding maximum temperature. The shaded area represents a region where the sulfate formation is thermodynamically favorable. From a practical point of view, the concentration of SO_2 in the regeneration off-gas must be as high as possible to afford economic final sulfur recovery. Hence, the oxygen concentration in the oxidizing gas should be the highest possible. However, as oxygen concentration in the feed is increased, the maximum temperature also increases, suggesting that a compromise should be met.

CONCLUSIONS

A method to obtain approximate solutions for a fixed-bed reactor with exothermic gas-solid reactions has been presented. By using a traveling wave representation the partial differential equations are converted to a system of integral equations, the kernel of which is approximated. The approximating function selected is analytically integrable. In the case of fast kinetics and/or adiabatic reactor, closed form solutions in terms of a streched variable are obtained. In the case of fast kinetics, these solutions correspond to a thin reaction region around the center of the traveling wave. This method was applied to investigate the conditions for the occurrence of a secondary sulfate formation reaction during ZnS oxidation.

ACKNOWLEDGMENTS

Miguel J. Bagajewicz gratefully acknowledges support from the Argentine National Research Council (CONICET) and from Universidad Nacional del Litoral (UNL) in Santa Fe, Argentina.

NOMENCLATURE

a : Stoichioemtric coefficient of the reactant gas

A : dimensionless number $A=a\frac{\rho_s}{c_0}\frac{(1-\epsilon_0)}{\epsilon_0}$

B : dimensionless Heat of Reaction $B=a\frac{(-\Delta H)}{C_{p_s}T^*}$

$\hat{c}$: Reactant Gas concentration (mol cc^{-1})

c : dimensionless gas concentration $c=\frac{\hat{c}}{c_0}$

c_0 : Reactant concentration at reactors feed (mol cc^{-1})

C_{p_s} : Solid Heat Capacity (Kcal mol^{-1} $°K^{-1}$)

C_{p_g} : Gas Heat Capacity (Kcal mol^{-1} $°K^{-1}$)

D : reactor diameter (cm)

E : Activation Energy (Kcal mol^{-1})

$\hat{F}(\hat{c},T)$: Gas factor in the reaction rate (cc mol^{-1})

$F(c,Y)$: dimensionless gas factor in the reaction rate
$F(c,Y)=\hat{F}(c_0c,T^*(1+Y))/c_0$

$\hat{G}(X,T)$: Solid factor in the reaction rate

$G(X,Y)$: Dimensionless solid factor in the reaction rate
$G(X,Y)=\hat{G}(X,T^*(1+Y))$

ΔH : Heat of Reaction (Kcal mol^{-1})

$k(T)$: Reaction Rate Arrhenius term (cc mol^{-1} sec^{-1})

$K(T)$: Equilibrium constant.

L : Reactor length (cm)

m : $=\frac{M}{(1+A)\delta-1}$

M : dimensionless Heat Transfer Coefficient $M=\frac{4U\epsilon_0}{D\rho_s C_{p_s}(1-\epsilon_0)}$

Q : Heat transferred through reactor wall (Kcal sec^{-1} cm^{-2})

s : =Nondimensional number, $s=\frac{B}{(1+A)\delta-1}$

t : time (sec)

t^* : Characteristic time $t^*=\frac{1}{c_0k(T^*)}$ (sec)

T^* : Characteristic temperature (°K)

T_w : Wall temperature (°K)

T_0 : Feed gas temperature (°K)

u : Linear gas phase velocity based on reactor cross sectional area. (cm sec^{-1})

U : Heat transfer coefficient (Kcal cm^{-2} sec^{-1})

X : Solid conversion

Y : Dimensionless Temperature. $Y = (T - T^*)/T^*$

z : Distance (cm)

z^* : Characteristic Length $z^* = \frac{t^* u}{(1+A)}$ (cm)

Greek Letters

δ : Quotient of Heat Capacitances $\delta = \frac{\rho_g C_{pg}}{\rho_s C_{ps}} \frac{\epsilon_0}{(1-\epsilon_0)}$

ϵ_0 : Bed porosity

γ : dimensionless Activation Energy $\gamma = E/RT^*$

ρ_s : Solid density (mol cc^{-1})

ρ_g : Gas density (mol cc^{-1})

τ : dimensionless time $\tau = t/t^*$

REFERENCES

1. Aris R. and Amundson N.R. *A.I.Ch.E. Journal*, 1957, **3**, 280.
2. Deans H.A. and Lapidus L. *A.I.Ch.E. Journal*, 1960, **6**, 656.
3. Deans D.A. and Lapidus L. *A.I.Ch.E. Journal*, 1960, **6**, 663.
4. Olbrich W.E., Agnew J.B. and Potter O.E., *Trans. Instn. Chem. Engrs.*, 1966, **44**, T207.
5. J.Szekely and J.H. Chen. *Proc. DECHEMA, Frankfurt, Germany* 1973.
6. Carey G.F. and Finlayson B.A. *Chem. Engng Sci.*, 1975, **30**, 587.
7. Eigenburger G. and Butt J.B. , *Chem. Engng Sci.*, 1976, **31**, 681.
8. Olson K.E., Luss D. and Amundson N.R. *Ind. & Eng. Chem., Proc. Des. & Dev.*, 1968, **7**, 1, 96.
9. Liaw W.K., Villadsen J. and Jackson R. *Amer. Chem. Soc. Simp. Series.*, 1982, 196.
10. Sampath B.S., Ramachandran P.A. and Hughes R. *Chem. Engng Sci.*, 1975, **30**, 135.
11. Van Deemter J.J., *Ind. Engng Chem.*, 1953, **45**, 1227.
12. Van Deemter J.J, *Industr. Engng Chem.*, 1954, **46**, 2300.
13. Johnson B.M., Froment G.F., and Watson C.C., *Chem. Engng Sci.*, 1962, **17**, 835.
14. Ozawa Y. *Ind. & Eng. Chem., Proc. Des. & Dev.*, 1969, **8**, 3, 378.
15. Gatica J.E., Puszynski P.A., Hlavacek V. *A.I.Ch.E. Journal* , 1987, **33**, 5.
16. Bhatia S.K. and Perlmutter D.D., *A.I.Ch.E. Journal*, 1981, **27**, 2.
17. MERC Hot Gas Cleanup Task Force Final Report, *MERC/SP-78/2* MERC, Morgantown WV, 1978.
18. GINER Inc. Final Report to Argonne National Laboratory, *Contract 31-109-39-5804*, Waltham MA, 1981.
19. Grindley T.; Steinfeld G. *DOE/MC/16545-1125,METC*, Morgantown WV, 1981.
20. Tamhankar S.S., Bagajewicz M.J., and Gavalas G.R.; Sharma P.K. and Flytzani-Stephanopoulos M. *Ind. & Engng Chem., Proc. Des. & Dev.*, 1985, **25**, 429.
21. Bagajewicz M.J. *PhD Thesis.* California Institute of Technology, 1987.

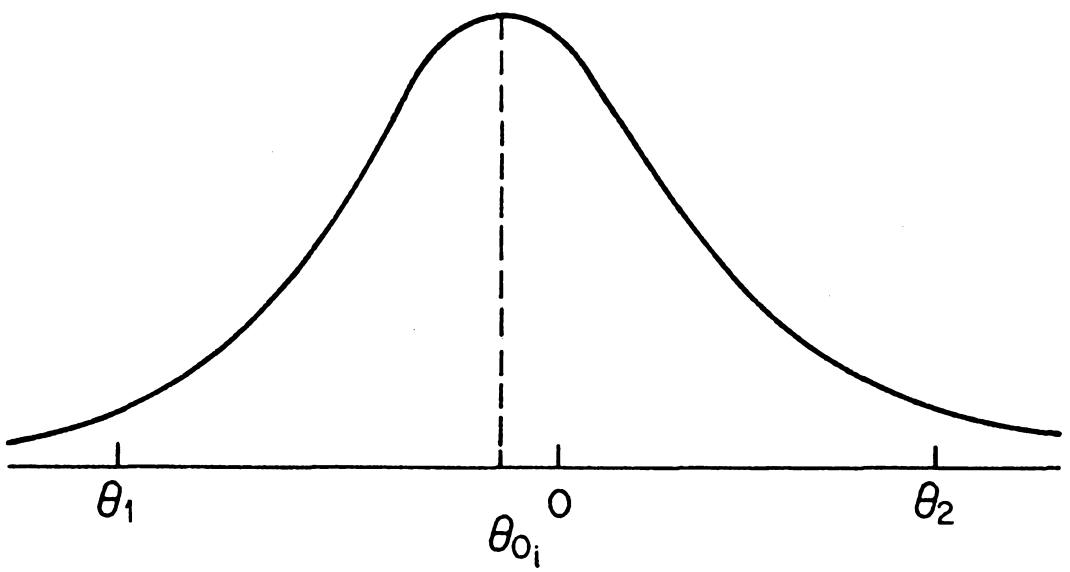

Figure 1: Schematic of the Approximating Function $R(\theta)$

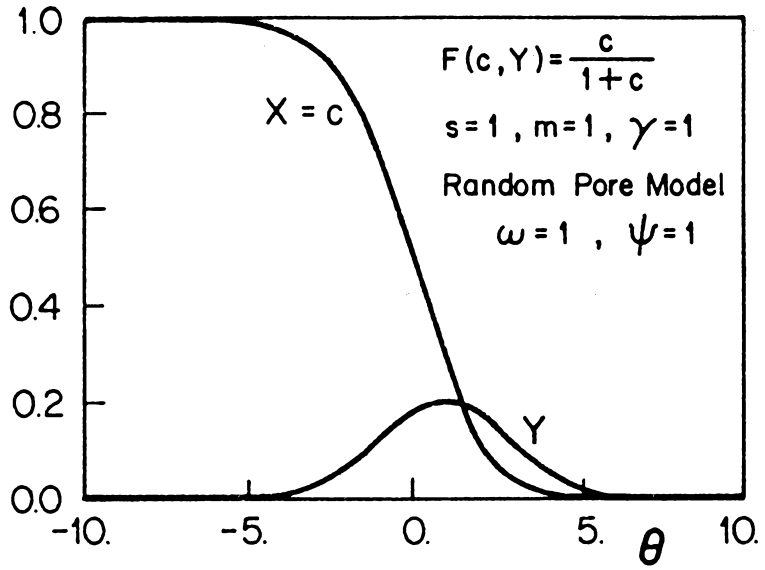

Figure 2a: Solid Conversion Profile and Reduced Temperature Profile obtained using the Approximate Method.

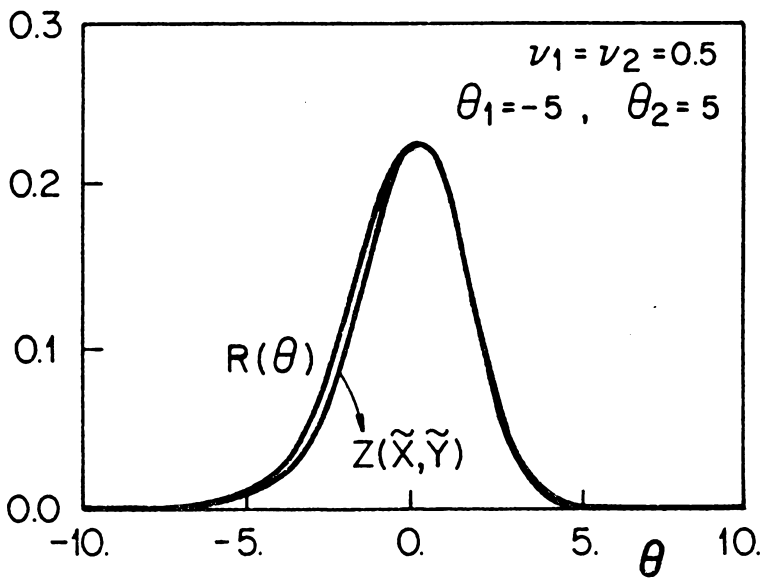

Figure 2b: Comparison of Approximating Kernel R(θ) and Z(X(θ), Y(θ)) at convergence.

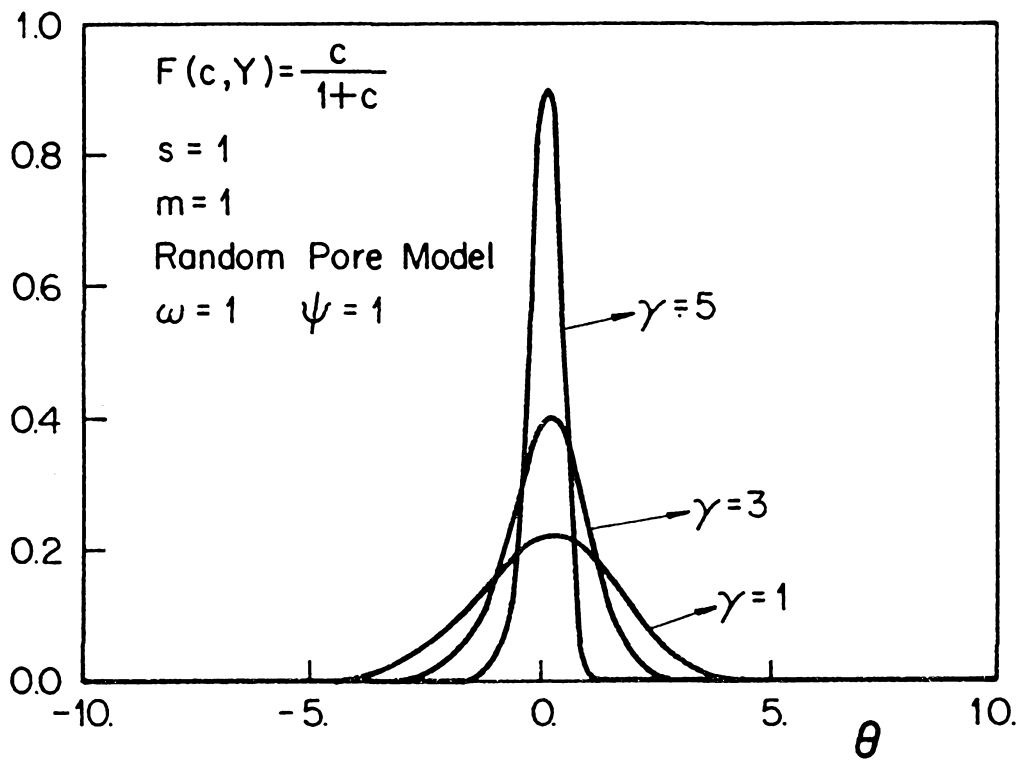

Figure 3: Comparison of Converged Kernels R_∞ for different Values of γ .

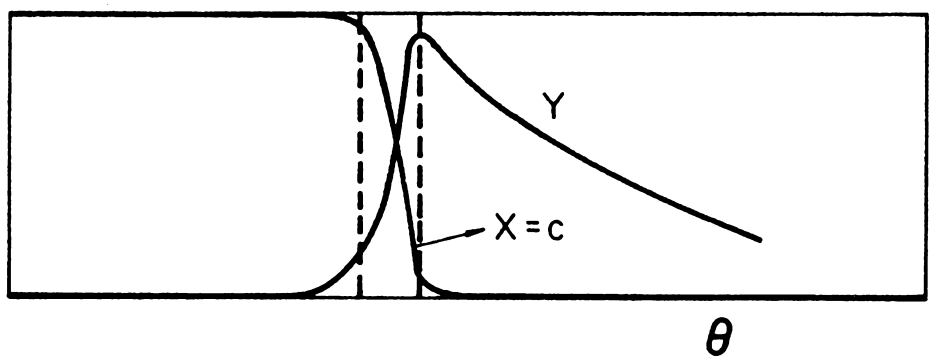

Figure 4: Schematic of the Conversion and Temperature Profile for a Steep Front developed for High γ .

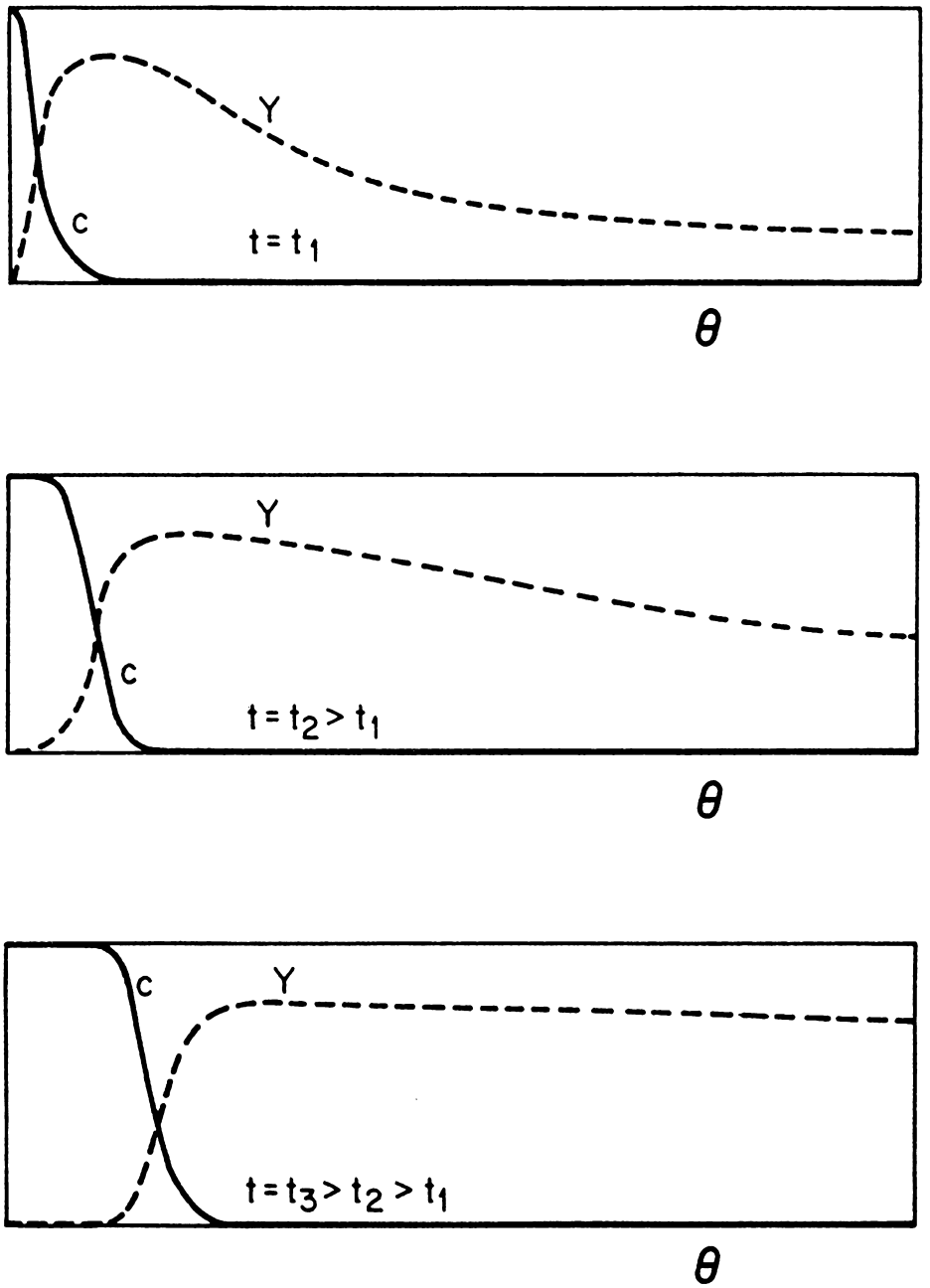

Figure 5: Schematic of the Conversion and Temperature Profile in a Finite Adiabatic Reactor at different Times.

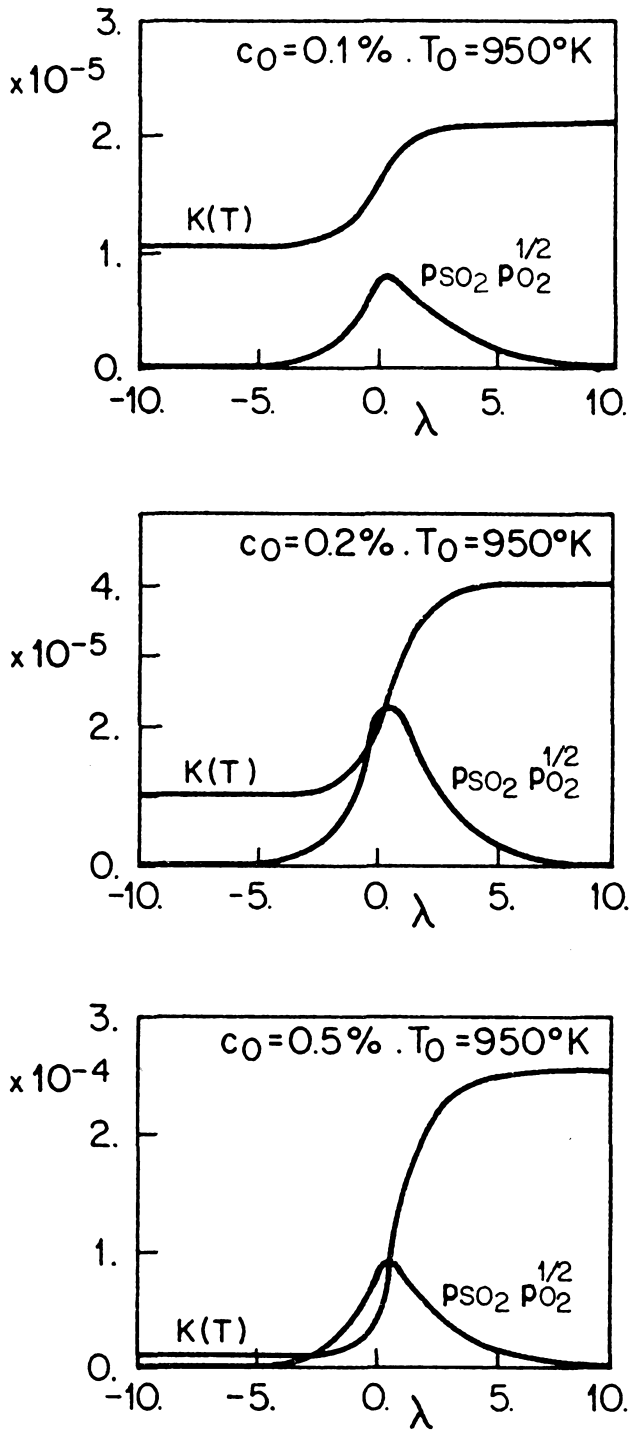

Figure 6: Comparison of the Values of the Product $p_{SO_2}\, p_{O_2}^{1/2}$ and K(T) for the Oxidation of ZnS , as a Function of a Streched Variable λ .

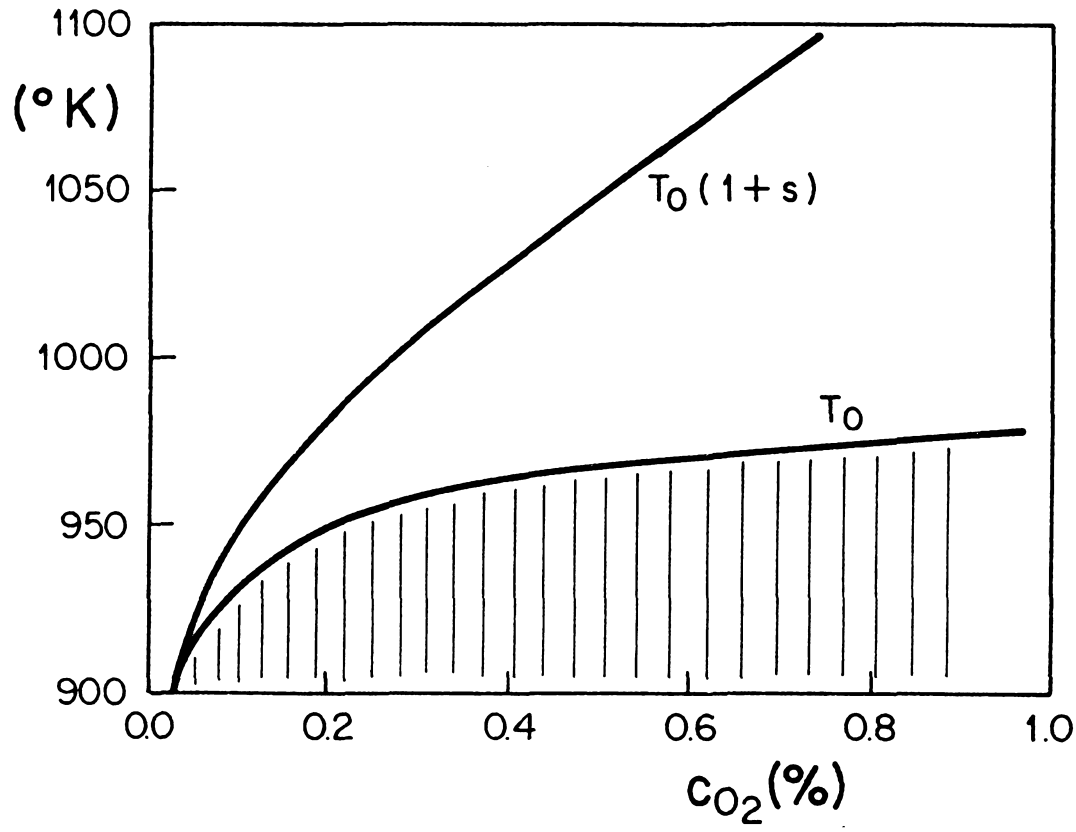

Figure 7: Critical Operating Temperature and Corresponding Maximum Temperature as a Function of Oxygen Concentration in the Feed.